Space Sci Rev (2008) 139: 3–62
DOI 10.1007/s11214-008-9403-7

Energy Deposition in Planetary Atmospheres by Charged Particles and Solar Photons

Jane L. Fox · Marina I. Galand · Robert E. Johnson

Received: 8 April 2008 / Accepted: 9 June 2008 / Published online: 13 August 2008

Abstract We discuss here the energy deposition of solar FUV, EUV and X-ray photons, energetic auroral particles, and pickup ions. Photons and the photoelectrons that they produce may interact with thermospheric neutral species producing dissociation, ionization, excitation, and heating. The interaction of X-rays or keV electrons with atmospheric neutrals may produce core-ionized species, which may decay by the production of characteristic X-rays or Auger electrons. Energetic particles may precipitate into the atmosphere, and their collisions with atmospheric particles also produce ionization, excitation, and heating, and auroral emissions. Auroral energetic particles, like photoelectrons, interact with the atmospheric species through discrete collisions that produce ionization, excitation, and heating of the ambient electron population. Auroral particles are, however, not restricted to the sunlit regions. They originate outside the atmosphere and are more energetic than photoelectrons, especially at magnetized planets. The spectroscopic analysis of auroral emissions is discussed here, along with its relevance to precipitating particle diagnostics. Atmospheres can also be modified by the energy deposited by the incident pickup ions with energies of eV's to MeV's; these particles may be of solar wind origin, or from a magnetospheric plasma. When the modeling of the energy deposition of the plasma is calculated, the subsequent modeling of the atmospheric processes, such as chemistry, emission, and the fate of hot recoil particles produced is roughly independent of the exciting radiation. However, calculating the spatial distribution of the energy deposition versus depth into the atmosphere produced by an incident plasma is much more complex than is the calculation of the solar excitation profile. Here, the nature of the energy deposition processes by the incident plasma are described as is the fate of the hot recoil particles produced by exothermic chemistry and by knock-on collisions by the incident ions.

J.L. Fox (✉)
Wright State University, Dayton, USA
e-mail: jane.fox@wright.edu

M.I. Galand
Imperial College, London, England

R.E. Johnson
University of Virginia, Charlottesville, USA

Keywords Energy deposition · Photon absorption · Chapman functions · Heating efficiencies · Auger electrons · Characteristic X-rays · X-ray absorption · Doubly charged ions · Core-excited ions · Auroral electrons · Auroral emissions · Color ratios · Auroral particles · Heavy ions · Electron transport · Pickup ions · Range of energetic particles · Knock-on · Recoil particles · Energy loss per ion pair

1 Introduction

The source for nearly all atmospheric processes is ultimately the interaction of solar photons and energetic particles of solar or magnetospheric origin with the atmosphere. We discuss first the energy deposition of solar FUV, EUV and X-ray photons. These photons and the photoelectrons that they produce may interact with thermospheric neutral species producing dissociation, ionization, excitation, and heating. The interaction of X-rays or keV electrons with atmospheric neutrals may produce ejection of inner shell electrons. The resulting core-ionized species may decay by the production of characteristic X-rays or Auger electrons.

Energetic particles may precipitate into the atmosphere, producing auroral emissions. Auroral energetic particles, like photoelectrons, interact with the atmospheric species through collisions that produce ionization, excitation, and heating of the ambient electron population. Auroral particles are, however, not restricted to the sunlit regions. They originate outside the atmosphere and are more energetic than photoelectrons, especially at the magnetized planets. Their spectral shape is very different from those of photoelectrons. The focus here is on the spectroscopic analysis of auroral emissions, their relevance to precipitating particle diagnostics, and the similarities and differences of such an approach applied to different planetary atmospheres.

Neutral atmospheres and ionospheres can be affected by coupling to an external plasma, such as the solar wind or a magnetospheric plasma. Therefore, in addition to being modified by the solar photon flux they can be modified by the energy deposited by the incident plasma ions and electrons. This flux might be associated with the solar wind plasma or, for satellites orbiting in a planet's magnetosphere, a trapped, magnetospheric plasma. The energy range of the incident ions and electrons can be large, extending from eV's to many MeV's. When the energy deposition by the plasma can be calculated, then the subsequent modeling of the atmospheric processes, which is discussed in a number of associated reviews in this issue, is roughly independent of the exciting radiation. This is the case both for the quasi-thermal chemistry and the emission processes, but is also the case for the fate of the hot recoil particles produced by the incident ions or by exothermic chemistry. However, calculating the spatial distribution of the energy deposition versus depth into the atmosphere produced by an incident plasma is much more complex than is the calculation of the solar excitation profile, as discussed briefly below, but in detail by Ledvina et al. (2008). The complexity is due not only to the feedback processes that control the interaction of an ionized upper atmosphere with the ambient fields, but also because of the flux of locally produced pick-up ions. In this paper, the nature of the energy deposition processes by the incident plasma are described as is the fate of the hot recoils produced by exothermic chemistry and by knock-on collisions by the incident ions. This involves not only describing the molecular physics initiated by the incident radiations but also the transport process that occurs in the energized regions of the atmosphere.

2 Solar Photon and Photoelectron Energy Deposition

Most of the solar energy flux is in the visible and infrared regions of the spectrum, which are characterized by photons with wavelengths in the range $\sim 4000-50{,}000$ Å. The photons in the visible (4000−8000 Å) and near ultraviolet (NUV) ($\sim 2000-4000$ Å) region of the solar spectrum arise from the photosphere, which is characterized approximately by a blackbody spectrum with a temperature of ~ 6000 K. Solar photons with wavelengths in the far ultraviolet (FUV) ($\sim 1000-2000$ Å) and the extreme ultraviolet (EUV) ($\sim 100-1000$ Å), originate in the chromosphere and the transition region to the corona, where the temperatures are in the range 10^4-10^6 K. Soft X-rays ($\sim 10-100$ Å) arise from the solar corona. Some authors refer to an XUV region, which comprises the wavelength range of about from about 10 to 250 Å (e.g., Solomon et al. 2001). Harder X-rays ($1 < \lambda < 10$ Å), which arise from solar active regions, are absorbed in the mesosphere and the mesosphere/thermosphere boundary. Only about 2% of the solar energy flux is carried by photons in the ultraviolet and X-ray regions of the spectrum. The regions of the solar spectrum that are absorbed in the thermospheres and upper mesospheres of the planets are generally characterized by wavelengths less than 2000 Å.

2.1 Photoabsorption and Scattering of Visible Photons

In the visible portion of the spectrum, the photoabsorption cross sections for the major atmospheric species at high altitudes in solar system bodies are negligible. Exceptions to this generalization include some trace species, such as ozone, which absorbs weakly in the Chappuis bands from $\sim 4500-8500$ Å in the terrestrial and Martian atmospheres. Some hydrocarbon radicals, which may be found in small abundances in the middle atmospheres of the outer planets, theoretically may undergo photodissociation in the visible region to produce an energetic H atom, such as $C_2H_5 + h\nu \rightarrow C_2H_4 + H$, for which the threshold dissociation energy (DE) is 1.65 eV (7535 Å) (e.g., Gilbert et al. 1999) and the 2-propyl radical $C_3H_7 + h\nu \rightarrow C_3H_6 + H$ for which the DE is 1.536 eV (8071.9 Å) (e.g., Noller and Fischer 2007). Visible photons therefore either penetrate to the surfaces or are scattered by cloud and haze particles on all the planets and satellites that have significant atmospheres.

The surface of the Earth is only partially obscured by water and water-ice clouds, which cover about 40% of the planet. On Mars, visible photons are partly attenuated by highly temporally and spatially variable airborne dust (e.g., Kahn et al. 1992) and water-ice hazes, such as the those that surround the poles during winter, and those that form during the afternoon over the Tharsis and Elysium uplands (e.g., Jakosky and Haberle 1992; Zurek et al. 1992).

On Venus, Titan and Triton, layers of clouds and hazes scatter visible photons and prevent them from penetrating to the surface. On Venus, the multi-layered cloud deck, which is composed of mostly sulfuric acid particles, water ices, and chlorine-containing species, extends from about 45 to 65 km. In the lower cloud layer there is evidence for a phosphorus-containing species such as phosphoric acid (H_3PO_4). Haze layers form above and below the main cloud layers (e.g., Esposito et al. 1983; Prinn 1985; Chamberlain and Hunten 1987; Esposito et al. 1997; de Pater and Lissauer 2001).

The ubiquitous hazes on Titan are probably composed of C_2 and higher hydrocarbons and large nitriles. Nitriles are organic species containing a triple CN bond, such as HCN (hydrogen cyanide), HC_3N (cyanoacetylene), CH_3CN (methyl cyanide) or C_2N_2 (cyanogen). These species are formed by ionizing and dissociating interactions of ultraviolet photons or energetic electrons with the major constituents CH_4 and N_2, followed by a rich and complicated photochemistry. The Titan surface is completely obscured by yellow-orange haze particles that are probably composed of tholins, which are

nitrogen-rich organic compounds or polymers. The haze particles are believed to contain a solid organic core (e.g., Baines et al. 1995; Israel et al. 2005; Tomasko et al. 2005; Lavvas et al. 2008). The cold surface of Triton, the temperature of which is of the order of 40 K, is also obscured partly by hazes that are probably composed of condensed hydrocarbons, and partly by patchy clouds of condensed N_2 (e.g., Gurrola et al. 1992; Stevens et al. 1992; Yelle et al. 1995).

The middle atmospheres of Jupiter and Saturn are characterized by various aerosols, hazes and multiple cloud layers that scatter visible radiation and limit its penetration to the lower atmospheres (e.g., Atreya et al. 1999; Moses 2000; West et al. 2004; Kim et al. 2006). Although NH_3 is an important minor component of the lower atmospheres of these planets (e.g., (Taylor et al. 2004); de Pater and Massie 1985; de Pater and Lissauer 2001), ammonia and NH_4SH condense to form cloud layers in the tropospheres of Jupiter and on Saturn. At higher altitudes, in the stratospheres of these planets, hydrocarbon haze layers are also present (e.g., Moses 2000; Kim et al. 2006). In the colder atmospheres of Uranus and Neptune, photochemical hydrocarbon hazes and ices may form in the stratospheres (e.g., Moses et al. 1992), and methane ices probably form tropospheric clouds (e.g., Baines et al. 1995).

2.2 Absorption of Ultraviolet Photons

The major thermospheric species of the terrestrial planets with oxidizing atmospheres (Venus, Earth and Mars) include O_2, N_2, CO_2, and Ar, with small admixtures of He, H_2, and the photolysis products, O, N, NO, CO and H. CO_2 is the major species in the lower thermospheres of Mars and Venus, but is a minor species in the terrestrial thermosphere. Although CO_2 condenses onto the surface of Mars none of the major or minor species condenses in the thermospheres of the planets, which are heated by EUV and FUV radiation (e.g., Roble et al. 1987; Fox and Dalgarno 1979, 1981; Fox 1988; Fox et al. 1995).

In the reducing thermospheres of the outer planets (Jupiter, Saturn, Neptune and Uranus), H_2, He, H, CH_4 and its photolysis products, CH_3, CH_2, and CH, along with photochemically produced higher hydrocarbons, are the dominant constituents (Gladstone et al. 1996; Yelle and Miller 2002).

The atmospheres of Titan and Triton are composed mostly N_2 and are of intermediate oxidation state; the thermospheres also contain small amounts of CH_4, H_2, and small radical species formed by chemistry initiated by photon or energetic electron impact, such as N, C and H. The abundances of C_2H_2, C_2H_6, C_2H_4, higher hydrocarbons, and nitriles such as HCN and HC_3N, and CH_3CN are significant in the lower thermospheres and the middle atmospheres (e.g., Krasnopolsky et al. 1993; Krasnopolsky and Cruikshank 1995; Keller et al. 1992; Marten et al. 2002; Yelle et al. 2006).

The photoabsorption cross sections for the small molecules and atoms that make up planetary thermospheres maximize in the extreme ultraviolet (EUV), with values of $\sim 10^{-17}-10^{-15}\,\mathrm{cm}^2$, and optical depth unity is reached for column densities in the range $(1-100)\times 10^{15}\,\mathrm{cm}^{-2}$. Therefore, any solar system body with a substantial atmosphere has a thermosphere and an ionosphere.

We here limit our discussion to the effects of absorption of FUV, EUV and soft X-ray photons. We specifically ignore the effects of the absorption of solar near infrared photons, which, however, play an important role in heating the lower thermospheres of the planets (e.g., Bougher et al. 1990; López-Valverde et al. 1998; Roldán et al. 2000; Bougher et al. 2008).

The absorption of photons in the far UV, EUV, and soft X-ray regions of the spectrum may lead to dissociation, ionization, or, in some cases, fluorescence of thermospheric species. The rate of absorption of photons that are characterized by wavelength λ at altitude z, $q_\lambda^a(z)$, is given by

$$q_\lambda^a(z) = F_\lambda(z)\sigma_\lambda^a n(z) \tag{1}$$

where σ_λ^a is the absorption cross section, $n(z)$ is the local number density, $F_\lambda(z) = F_\lambda^\infty \exp(-\tau_\lambda(z))$ is the local solar photon flux, and F_λ^∞ is the photon flux at the top of the atmosphere. The optical depth in a plane parallel atmosphere at altitude z is $\tau_\lambda(z, \chi) = \int_z^\infty \sigma_\lambda^a n(z')\sec(\chi)dz'$, where χ is the solar zenith angle. It can be easily shown that the maximum absorption rate in such an atmosphere for solar zenith angle χ is found at the altitude at which $\tau_\lambda(\chi)$ is unity. In order to compute the total photoabsorption rate, (1) must of course be integrated over all wavelengths. In any realistic multi-constituent atmosphere, the rate of photoabsorption must also be summed over all major species.

The column density above an altitude z is defined as $N(z) = \int_z^\infty n(z')dz'$. Note that here we have denoted the local number density $n(z)$, and we have reserved $N(z)$ to indicate the column density. For an atmosphere in hydrostatic equilibrium, the variation of pressure P with altitude is given by

$$\frac{dP(z)}{dz} = -\rho(z)g(z) \tag{2}$$

where the $\rho(z)$ is the mass density and $g(z)$ is the acceleration of gravity.

In the following equations, most of the variables are altitude dependent, but for the purpose of compactness, we have suppressed the variable z. The pressure P at a given altitude is just the force (or weight) per unit area of the atmosphere above that altitude, which is simply given by $P = Nm_a g$. The pressure can also be expressed by the ideal gas law:

$$P = nkT = Nm_a g \tag{3}$$

where k is Boltzmann's constant. Combining the ideal gas law with the definition of $\rho = nm_a$, where m_a is the average mass of the atmospheric constituents, we can derive an expression for the mass density, $\rho = (Pm_a/kT)$. Substituting this expression into (2) and rearranging, we obtain

$$dP/P = \frac{-m_a g}{kT}dz = -1/H_p, \tag{4}$$

where the pressure scale height H_p is defined as kT/mg. Equation (4) can be integrated to give the barometric formula

$$P = P_0 \exp\left(-\int_{z_0}^{z} 1/H_p\right). \tag{5}$$

In this equation, the subscript 0 indicates an arbitrary reference level.

Equations (3) can be rearranged to give a simple expression for the vertical column density

$$N = n\frac{kT}{m_a g} = nH_p. \tag{6}$$

This rather general expression is valid if we assume that the acceleration of gravity and m_a are constant; these assumptions are valid over altitude ranges of the order of a scale height in

the mixed region of the atmosphere, that is, below the homopause. For $\chi \neq 0$, the altitude of unit optical depth occurs where the column density along the line of sight to the sun $N(\chi) = N(0)\sec(\chi)$ is the inverse of the absorption cross section, i.e., $N(\chi) = {\sigma_a}^{-1}$. The photon fluxes F_λ^∞ at the top of the atmosphere depend on the distance of the planet from the Sun at a given place in its orbit, solar activity (usually as measured by a suitable proxy), and the solar flux model that is used.

2.3 Solar Flux Models

Among the early versions of the solar spectra used in modeling are those of Hinteregger et al. (e.g., 1981), which were based on measurements of the EUVS experiment on the Atmosphere Explorer satellites. The measurements were normalized and extended outside the wavelength range of the satellite measurements, 142–1850 Å using data from rocket experiments (e.g., Heroux and Hinteregger 1978). Often the solar flux models are denoted by the last two digits of the year and the 3 digit ordinal day of year that they apply to, such as 74113, 76200 (which is also known as SC#21REFW, the successor to the F76REF), and 79050. The first two spectra pertain to low solar activities and the latter to high solar activity of solar cycle 21. In "Hinteregger-style" spectra, the solar fluxes are given at 1 Å resolution in the continua, and as delta functions at the central wavelength of the strong solar lines, for a total of more than 1800 wavelengths from 18 to 2000 Å. Sometimes larger spectral ranges are used, for a total of 37 intervals from 50 to 1050 Å (e.g., Torr et al. 1979). The Hinteregger spectra are also known as the SERF1 solar flux models (e.g., Tobiska 1991).

More recently, the solar fluxes that have been used in thermosphere/ionosphere modeling have been derived from the SOLAR 2000 (S2K) models of Tobiska (e.g., Tobiska 2004; Tobiska and Bouwer 2006). The S2K v2.2x spectra are normalized to the measurements from the Solar EUV Experiment (SEE) on the Thermosphere Ionosphere Mesosphere Energetics and Dynamics (TIMED) spacecraft. The SEE instrument has measured solar irradiances in the range 1 to 1940 Å in 10 Å intervals from 2002 to the present. (e.g., Woods et al. 2005; see also the instrument website at lasp.colorado.edu/see). Other commonly used models include the S2K v1.24 spectra, which are normalized to the data from the Student Nitric Oxide Explorer (SNOE) spacecraft (e.g., Bailey et al. 2000). The latter spectra yield larger peak electron densities that are in better agreement with the measured electron density profiles for Mars and Venus. In Fig. 1a, we present the photon fluxes of the S2K 2.22 model for day 76200 (low solar activity) from 18 to 2000 Å; in Fig. 1b, we show the ratio of the S2K 2.22 photon fluxes to those of the S2K v1.24 spectrum over the range 18 to 1100 Å.

2.4 Chapman Layer Theory

The interaction of photons with atmospheres was first described in a simple but insightful way by Chapman (1931a). The details of Chapman layer theory have been described in many textbooks (e.g., Rishbeth and Garriott 1969; Bauer 1973; Banks and Kockarts 1973; Schunk and Nagy 2000; Bauer and Lammer 2004), and will not be repeated here. Although a Chapman layer need not be an ion/electron layer, we will confine ourselves to a brief presentation of the salient features and most important equations for ionospheric ion and electron density profiles.

In Chapman layer theory for ions, the thermosphere is assumed to be composed of one molecular constituent, XY, which is ionized by the absorption of monochromatic solar photons

$$\mathrm{XY} + h\nu \rightarrow \mathrm{XY}^+ + \mathrm{e}. \tag{7}$$

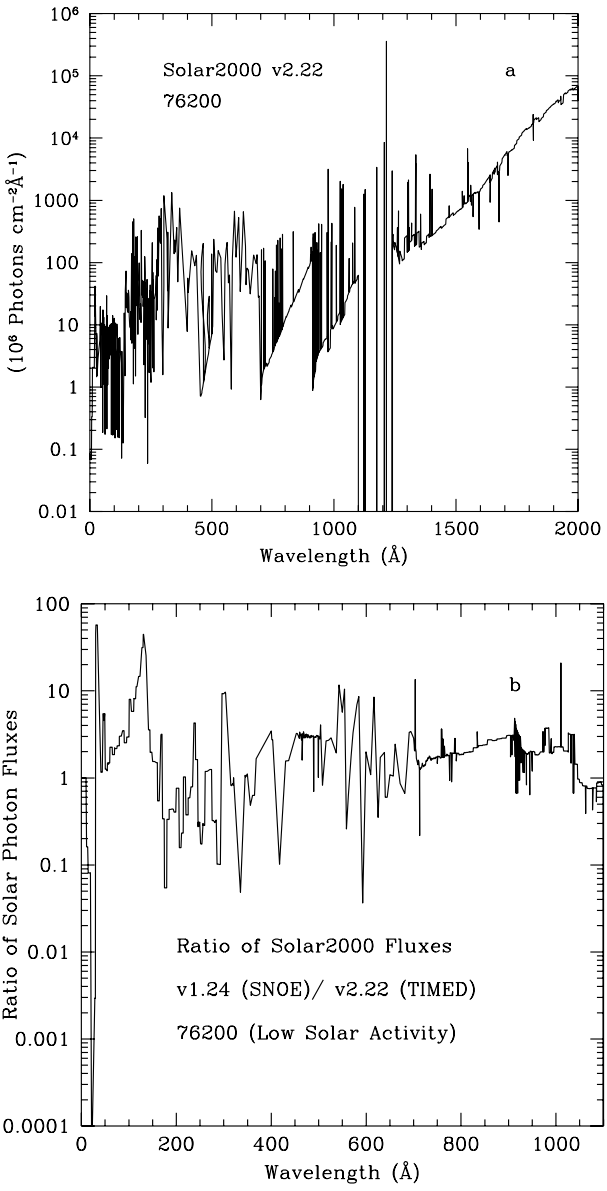

Fig. 1 (**a**) Photon fluxes from 18 to 2000 Å for the 76200 S2K v2.22 solar flux model of Tobiska (2004). (**b**) Ratio of S2K 2.22 v1.24 photon fluxes to the S2K 2.22 photon fluxes from 18 to 1100 Å

The ion XY^+ is destroyed locally by dissociative recombination with a rate coefficient α_{dr}:

$$XY^+ + e \rightarrow X + Y. \tag{8}$$

The production rate of XY^+ by photoionization is given by a general equation similar to that for photoabsorption above (see (1)):

$$q^i = F\sigma^i n_{XY}, \tag{9}$$

where n_{XY} is again the number density of the neutral molecule XY, and σ^i is the ionization cross section. The loss rate for dissociative recombination is given by $L = \alpha_{DR} n_i n_e$, where n_i is the ion density, which, because of charge neutrality, is equal to n_e, the electron density. In Chapman theory photochemical equilibrium (PCE) is assumed, which means that at steady-state, the photochemical production and loss rates are equal. The electron and ion densities are given by

$$n_e = n_i = \left[\frac{F\sigma^i n_{XY}}{\alpha_{dr}}\right]^{1/2}. \tag{10}$$

In Chapman theory the temperature T and mass of XY are assumed to be constant; furthermore, if the altitude dependence of the acceleration of gravity g is ignored, $H_p = kT/mg$ is a constant and the barometric formula (5) can be expressed in terms of the number density $n_{XY}(z) = n^0_{XY} \exp(-z/H)$, where n^0_{XY} is the number density at an arbitrary reference altitude, which may be defined as $z = 0$. Under these conditions the pressure and number density scale heights are equal. If the production rate of ions in a Chapman layer for solar zenith angle (χ) is given by (9), and the maximum ionization rate occurs at $z = 0$ where $\tau = 1$:

$$q^i_{\max,\chi} = \frac{F^\infty}{e}\frac{\sigma^i}{\sigma^a H \sec\chi} = \frac{q^i_{\max,0}}{\sec\chi}, \tag{11}$$

The ionization rate q^i_χ at altitude z can be expressed in terms of the maximum ionization rate for overhead sun as

$$q^i_\chi(z) = q^i_{\max,0} \exp\left[1 - \frac{z}{H} - \sec\chi\, e^{-z/H}\right]. \tag{12}$$

Combining (10) and (12), the ion density profile in Chapman theory for a plane parallel atmosphere is given by

$$n_{\rm i}(z) = \left[\frac{q^i(z)}{\alpha_{\rm dr}}\right]^{1/2} = \left[\frac{q^i_{\max,0}}{\alpha_{\rm dr}}\right]^{1/2} \exp\left[\frac{1}{2} - \frac{z}{2H} - \frac{1}{2}\sec\chi\, e^{-z/H}\right], \tag{13}$$

and the maximum ion or electron density as a function of solar zenith angle is then

$$n^i_{\max,\chi} = n^i_{\max,0}(\cos\chi)^{0.5}. \tag{14}$$

The mathematically elegant theory described above is confined to the plane parallel approximation, which becomes increasingly invalid as the terminator is approached. For near terminator region, the sphericity of the atmosphere must be taken into account. In these cases, $\sec\chi$ is often replaced by the Chapman Function, $Ch(x, \chi)$, where $x = R/H_n$, R is the distance from the center of the planet, and H_n is the (constant) neutral scale height. The Chapman Function, which is the ratio of the number density along the line of sight to the Sun in spherical geometry to the vertical column density, has been approximated by various combinations of analytical functions (e.g., Chapman 1931b; Rishbeth and Garriott 1969; Smith and Smith 1972; Bauer 1973). Huestis (2001) has reviewed the various approximations, and described a new analytical evaluation of the Chapman function that is accurate for a large range of χ and for small values of x. Since the advent of fast computers, however, the use of the Chapman function has become unnecessary.

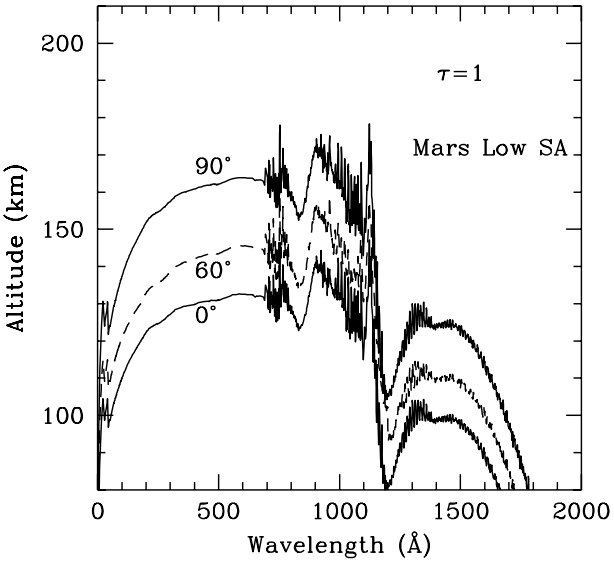

Fig. 2 Altitude of optical depth unity for a low solar activity model of Mars for 0, 60 and 90° SZA

It is fairly easy to compute the optical depth $\tau(\lambda, z, \chi)$ along the line of sight to the Sun in spherical geometry numerically, as described, for example by Rees (1989). For solar zenith angles χ less than 90°,

$$\tau(\lambda, z, \chi) = \sum_j \int_z^\infty n_j(z')\sigma_j^a(\lambda)\left[1 - \left(\frac{R+z}{R+z'}\right)^2 \sin^2\chi\right]^{-0.5} dz', \tag{15}$$

where R is the planetary radius, and the sum over species j is shown explicitly. For χ greater than 90°, the optical depth can be computed as

$$\tau(\lambda, z, \chi) = \sum_j \left\{ 2\int_{z_s}^\infty n_j(z')\sigma_j^a(\lambda)\left[1 - \left(\frac{R+z_s}{R+z'}\right)^2 \sin^2 90^\circ\right]^{-0.5} dz' \right.$$
$$\left. - \int_z^\infty n_j(z')\sigma_j^a(\lambda)\left[1 - \left(\frac{R+z}{R+z'}\right)^2 \sin^2\chi\right]^{-0.5} dz' \right\} \tag{16}$$

where z_s is the tangent altitude. It is of course unnecessary to include the $\sin^2 90^o = 1$ factor explicitly in the first term on the right of (16), but we include it here in order to clarify the origin of the formula for the optical depth as twice the total horizontal optical depth along the line of sight to the sun minus that beyond the solar zenith angle χ.

Figure 2 shows optical depth unity as a function of wavelength from the soft X-ray region to the mid FUV region for a low solar activity model of Mars for solar zenith angles 0, 60 and 90°. There is a small increase in the penetration depth as the solar zenith angle increases from 0 to 60°, but a somewhat larger increase occurs from 60 to 90° SZA.

Because of the simplifying assumptions built into the Chapman layer theory, there is no reason to believe that real ionospheric profiles are even quasi-Chapman. Although thermospheric temperatures approach a constant value, T_∞, at high altitudes in stationary atmospheres, thermospheric temperatures increase rapidly near and above the ion peak, where much of the solar energy is deposited.

Table 1 Ionization potentials (I_P) of Some Species of relevance to Planetary Atmospheres[a]. Units are eV

High I_P		Medium I_P		Ionized by Ly α	
Species	I_P	Species	I_P	Species	I_P
He	24.59	H_2O	12.61	C_4H_2	10.18
Ne	21.56	CH_4	12.51	NH_3	10.16
Ar	15.76	SO_2	12.32	CH_3	9.84
N_2	15.58	CH_3CN	12.194	C_3H_6	9.73
H_2	15.43	O_2	12.07	NO	9.264
N	14.53	HC_3N	11.64	C_6H_6	9.246
CO	14.01	C_2H_6	11.52	Si	8.152
CO_2	13.77	C_2H_2	11.40	C_2H_5	8.13
O	13.618	C	11.26	HCO	8.10
H	13.598	C_3H_8	10.95	C_3H_7	8.09
HCN	13.60	CH	10.64	Fe	7.87
OH	13.00	C_2H_4	10.51	Mg	7.65
		H_2S	10.45	trans-HCNH	7.0[b]
		CH_2	10.4	cis-HCNH	6.8[b]
		S	10.35	Ca	6.11
				Na	5.139

[a]Computed with data from Lias et al. (1988), except as noted

[b]From Nesbitt et al. (1991)

Thermospheres also have multiple neutral constituents, and ionospheres are composed of many ions; they are not in PCE at high altitudes. In fact, the largest peaks on the Earth and outer planets are composed of atomic ions O^+ and H^+, respectively, and are F_2 peaks (e.g., Banks and Kockarts 1973; Hinson et al. 1998; Waite and Cravens 1987). F_2 peaks are formed where the time constant for loss by chemical reactions, $\tau_c = 1/\mathcal{L}$, where $\mathcal{L} = L/n$ is the specific loss rate, is equal to the time constant for diffusion, $\tau_d = H^2/D$, where D is the ambipolar diffusion coefficient. Thus PCE breaks down as the F_2 peaks are approached from below.

In addition, the ionizing fluxes are not monochromatic, but cover a range from the ionization potentials of the species to the soft X-ray region of the solar spectrum. Ionization potentials of the common atmospheric species in the atmospheres of the planets are shown in Table 1. The photoionization cross sections, $\sigma^i(\lambda, j)$ and the photoabsorption cross sections $\sigma^a(\lambda, j)$ are functions of wavelength λ and are species dependent. The dissociative recombination coefficient α_{dr} depends on the identity of the ion and has a dependence on the electron temperature that is usually expressed as $(300/T_e)^b$. In this formula, the exponent b has a theoretical value of 0.5, but is found experimentally to be in the range 0.2−0.7, and may itself be temperature dependent. Most important, ionization by solar photons is supplemented by that of photoelectrons, which in general deposit their maximum energy below that of photons.

On the topsides, the ion and electron density profiles are determined to varying extents by the electron (T_e) and ion (T_i) temperatures which are equal to the neutral temperatures only in the lower ionosphere where collision rates between neutrals, ions and electrons are high. The plasma temperatures are larger than T_n at higher altitudes. Some examples of neutral, ion and electron temperature profiles are given in Fig. 3 of Witasse et al. (2008).

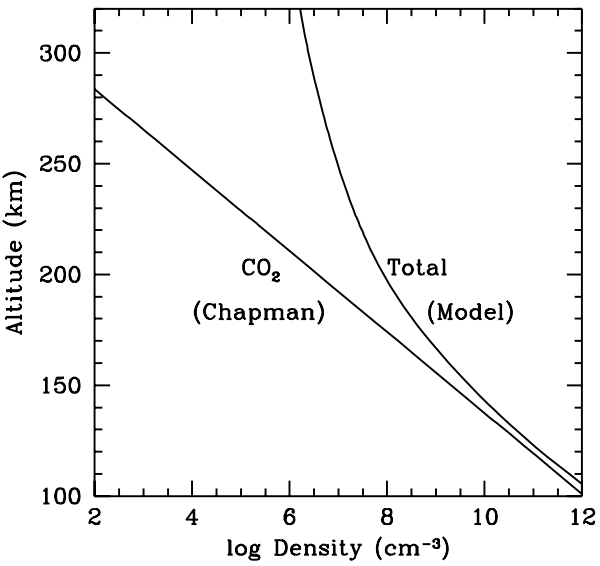

Fig. 3 Altitude profiles of total neutral densities for models based on Chapman profiles and a realistic profile from a model of Mars. The Chapman neutral model profile consists of pure CO_2, while the realistic model profile is made up of 12 neutral species. It is clear that the scale height increases with altitude in the realistic model. This is a result of increasing neutral temperatures, and increased abundances of lighter species

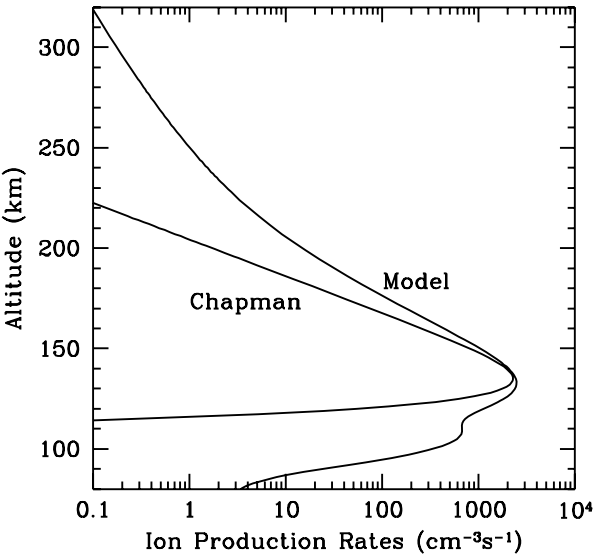

Fig. 4 Ion production rates for the models shown in Fig. 3. Neither the topside nor the bottomsides of the Chapman profiles fit the model profiles

In order to compare Chapman profiles with detailed, realistic numerical models, we have constructed a 60° SZA low solar activity model of the Martian thermosphere/ionosphere similar to those of Fox (2004). In order to fit the Chapman profile, we have determined the CO_2 number density profile for which the ionospheric peak magnitude and altitude reproduce the F_1 peak of the realistic model. This CO_2 profile is compared to the total neutral number density profile of the realistic model in Fig. 3. The resulting ionization profile from 100 to 320 km for the realistic model is presented in Fig. 4 where it is compared with that of the Chapman layer production profile. It is obvious that the realistic ionization profile does not fit the Chapman model at either low or high altitudes. At high altitudes the temperature

increases above that at the peak, and the abundance of light atoms increase. This results in an increasing neutral scale height above the peak, rather than a constant scale height as required by Chapman theory.

Photoionization of the various atmospheric species by EUV photons occurs over a broad wavelength range, which in turn causes broadening of the upper F_1 electron density peak. The major mechanism for production of ions in this region is absorption of EUV photons. In fact, this is how we define the F_1 peak here (Banks and Kockarts 1973; Bauer 1973; Bauer and Lammer 2004). Other workers have defined it differently. The photoelectrons produced near the F_1 peak may cause further ionization. The maximum in the ion production rate profile for photoelectrons is slightly below that of photons in the F_1 region. Solar soft X-rays penetrate to lower altitudes in the thermosphere, and produce very high energy photoelectrons. These photoelectrons may produce multiple ionizations at altitudes below the lower E-region peak in the photoionization profile. For example, in a high solar activity model of the Martian ionosphere, the average energy of the photoelectrons produced near the F_1 peak at 135 km is 25.1 eV, and that near the E peak at 117 km is 161 eV.

In fact, ionization at the lower (E-region) peak is caused mainly by impact of photoelectrons and secondary electrons:

$$CO_2 + e^* \rightarrow CO_2^+ + e^* + e, \tag{17a}$$

$$CO_2 + e^* \rightarrow CO^+ + O + e^* + e, \tag{17b}$$

$$CO_2 + e^* \rightarrow O^+ + CO + e^* + e, \tag{17c}$$

where the asterisk denotes an electron with enough energy to potentially produce further ionization. Equations (17b) and (17c) illustrate dissociative ionization of CO_2, which is the main source of the fragment ions O^+ and CO^+ ions at the E-region peak. A comparison of the sources of ionization caused by photons and photoelectrons is shown in Figs. 5a and 5b.

The model electron density profile between the altitudes of 100 and 320 km is compared to that of a Chapman layer in Fig. 6. It is easily seen that the model profile and the Chapman layer are very different both above and below the peak. The Chapman layer is characterized by a constant scale height above the peak, and the electron densities fall off rapidly below the peak. The model electron densities are, however, larger and are characterized by scale heights that vary above the peak. Above about 180 km the scale height increases rapidly, so that near the 300 km, the difference in densities is nearly 3 orders of magnitude. The ion number density scale height H_n^i differs from the plasma pressure scale height $H_p^i = kT_p/(m^i g)$, where m^i is the ion mass and $T_p = T_i + T_e$ is the plasma temperature according to the equation

$$\frac{1}{H_n^i} = \frac{1}{H_p^i} + \frac{1}{T_p}\frac{dT_p}{dz}. \tag{18}$$

At high altitudes where the plasma temperatures increase rapidly in the model, the second term on the right becomes larger than the first, and all the ions are characterized by the same scale height. In addition, PCE breaks down for O_2^+ in the Mars models above an altitude of about ~ 184 km at low solar activity and near ~ 216 km at high solar activity.

As Fig. 6 illustrates, in the region below the F_1 peak, where the Martian ion production rate is dominated by absorption of soft X-rays and the concomitant ionization by high energy photoelectrons and secondary electrons, the model densities are much larger than those of the single Chapman layer model, in which the ionizing photons are monochromatic. The total electron content (TEC) of the model is $\sim 4.9 \times 10^{11}$ cm^{-2}, whereas the TEC for the Chapman profile is 2.7×10^{11} cm^{-2}, which is smaller by almost a factor of two.

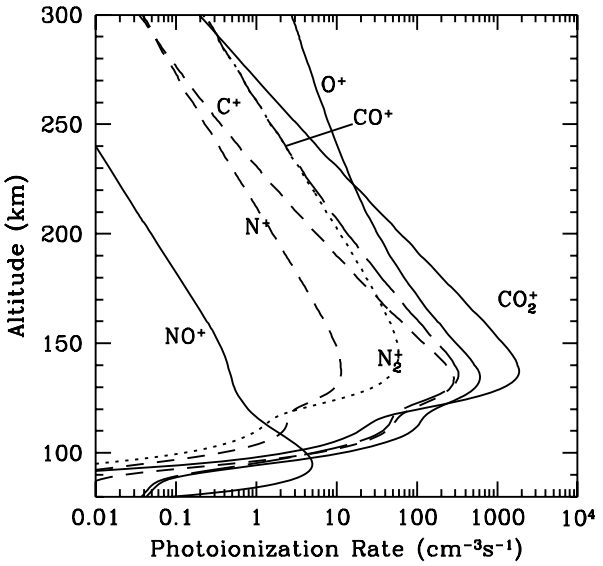

(a)

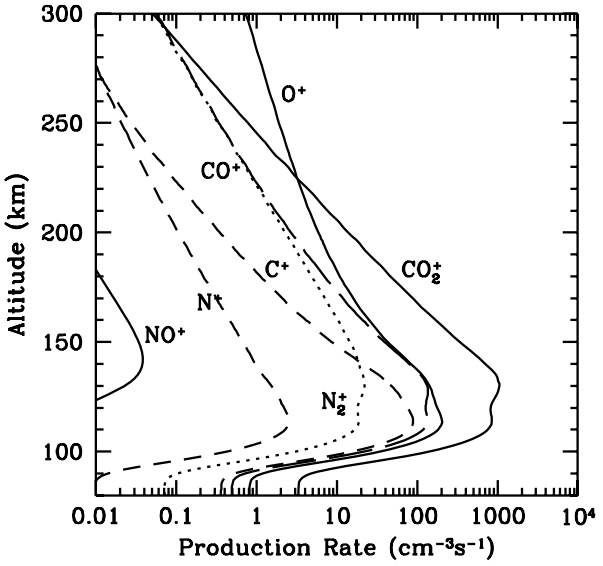

(b)

Fig. 5 Computed ionization rate profiles from 80 to 300 km for 7 ions for a high solar activity 60° SZA model of Mars. (**a**) Production rates by photoionization. (**b**) Production rates by energetic photoelectron and secondary electron impact. Near the F_1 peak, the ionization is mostly by EUV photons. Near the E-region peak, however, ionization by very energetic photoelectrons and further electrons produced by electron impact ionization dominate

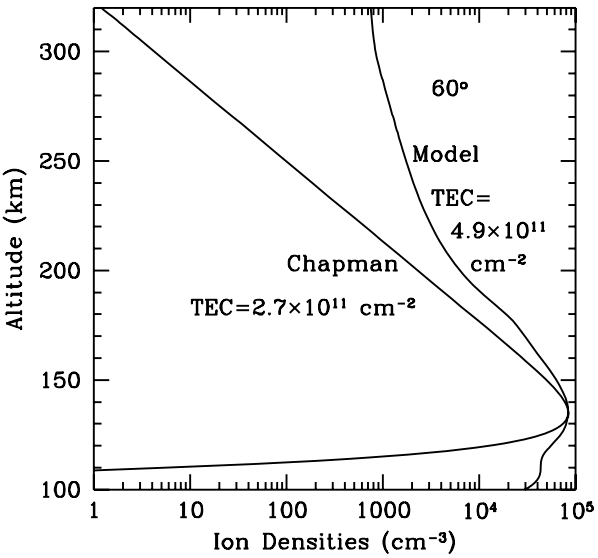

Fig. 6 Total ion or electron density profiles for the Chapman model and the realistic 60° SZA Mars models. These densities correspond to the neutral density profiles and production rates in Figs. 3 and 4. The total electron contents (TEC) are compared

2.5 Photodissociation

Photodissociation is a major source of thermal, and translationally or electronically excited atoms and small fragments in the thermospheres and mesospheres of the planets. Photodissociation can be represented as

$$\mathrm{XY} + \mathrm{h}\nu \rightarrow \mathrm{X} + \mathrm{Y}, \tag{19}$$

where XY is a molecule, X and Y are fragments; the rate of dissociation, q^d, can theoretically be determined similarly to that of ionization (see (9))

$$q_\lambda^d = F_\lambda \sigma_\lambda^d n_{XY}, \tag{20}$$

where σ_λ^d is the wavelength dependent photodissociation cross section, and n_{XY} is the number density of the molecule. As always, q^d, F and n_{XY} are functions of altitude. To a first approximation, the photoabsorption cross section is the sum of the photoionization and photodissociation cross sections. To obtain the total photodissociation rate, q_λ^d must be summed over wavelengths in the solar spectrum from the photodissociation threshold to the point where the photodissociation cross section is zero, that is, where photoabsorption cross section is equal to the ionization cross section. For simple molecules, such as H_2, N_2, O_2, CO, and CO_2, that wavelength is the range ~600–750 Å (e.g., Berkowitz 2002). Model calculations of photodissociation rates in atmospheres may appear to be simple, but in practice, they are complicated by several factors. Measured photoionization cross sections in the continuum shortward of about 600 Å, where photodissociation does not compete with ionization are fairly accurate. Immediately shortward of the photoionization threshold, however, the photoabsorption cross sections usually are highly structured. In this region the photodissociation cross sections are calculated as the difference between the photoabsorption cross sections and the photoionization cross sections, which may be the difference between two large numbers. In addition, if the photoionization and photoabsorption cross sections are not

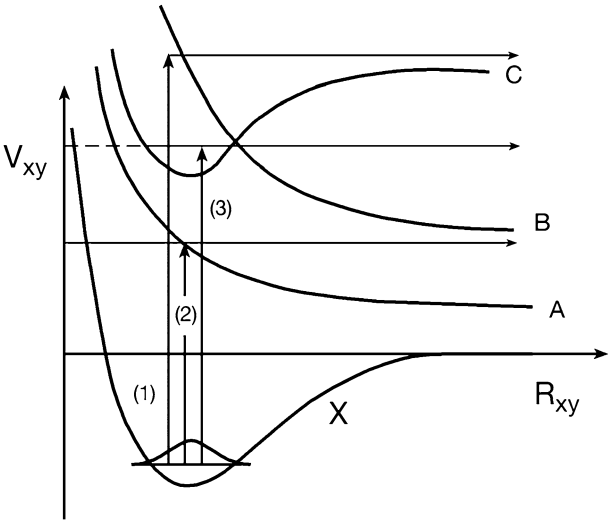

Fig. 7 Schematic representation of the three major mechanisms for photodissociation. (*1*) Excitation to the continuum of bound state (C) (*2*) Excitation to the purely repulsive state (A). Discrete excitation to a bound state (C) that is predissociated by a radiationless transition to the repulsive state (B)

adopted from a single source, there is a large potential for error in the computation of the photodissociation cross sections.

Longward of the photoionization threshold, the photoabsorption cross sections are usually taken to be equal to the photodissociation cross sections. In principle, the absorption of some photons may lead directly to fluorescence, but the fraction is generally small. For example, weak visible fluorescence in the wavelength range of 5500–7500 Å has been detected in the photoabsorption of O_2 at 1162 Å by Lee and Nee (2000), and provisionally attributed to the O_2 $D^3\Sigma_u^+(v' = 6) \rightarrow C^3\Pi_g(v'')$ transition.

Photodissociation can proceed via three possible mechanisms, which are illustrated schematically in Fig. 7. Absorption of a photon may excite a molecule into the continuum of an excited state (process 1), or to a purely repulsive state (process 2). The photodissociation cross sections for both of these processes are fairly smooth as a function of wavelength, and the photodissociation rates may usually be modeled with relatively low resolution cross sections and solar fluxes, of the order of 0.5–1 Å. Alternatively, photons may be absorbed into discrete excited states of the molecule, followed by predissociation (process 3). In order to model the rates of photodissociation proceeding via this mechanism, the individual bands must be resolved and the predissociation probabilities must be known. The photoabsorption rate must be modeled using very high resolution (of the order of 10^{-3} Å) photodissociation cross sections and a similarly high resolution solar spectrum. In addition, the photoabsorption cross sections are usually temperature dependent, and therefore the cross sections must be measured and calculations carried out at temperatures relevant to the part of the atmosphere where the absorption takes place.

We will illustrate these processes by describing the photoabsorption characteristics of some atmospherically important molecules. In order to illustrate the wealth of possible processes, we will focus on the details for O_2, which, because of its importance in the terrestrial atmosphere, has been the subject of many investigations. Photoabsorption by other relevant planetary thermospheric molecules will be discussed briefly.

2.6 Photoabsorption of O_2

In the wavelength region between the O_2 photoabsorption threshold at 2424 Å (5.11 eV) and about 2050 Å, most to the photodissociation is via the dipole forbidden absorption directly into the continuum of the $A^3\Sigma_u^+$ state (process 1). This is the upper state of the Herzberg I system:

$$O_2(X^3\Sigma_g^-) + h\nu \rightarrow O_2(A^3\Sigma_u^+) \tag{21a}$$

$$\rightarrow O(^3P) + O(^3P). \tag{21b}$$

Excitation into the continua of the O_2 ($A'^3\Delta_u$) state (the upper state of the Herzberg III band system) and the O_2 ($c^1\Sigma_u^-$) state (the upper state of the Herzberg II band system) also contribute to a lesser extent (e.g., Saxon and Slanger 1986). From 2050 to 2400 Å the cross sections decrease from about 7×10^{-24} to 1×10^{-24} cm^2 (e.g., Yoshino et al. 1988). Because the cross sections are very small, absorption by O_2 in the Herzberg continuum takes place in the terrestrial stratosphere where it competes with absorption by O_3. In the wavelength region between 192 and 205 nm, the absorption into the Herzberg continuum is much less efficient than that into the first Schumann-Runge (S-R) bands (e.g., Coquert et al. 1990; Yoshino et al. 1992).

Photoabsorption into the discrete states of the S-R band system of O_2 followed by predissociation dominates the absorption in the 1750–2050 Å range (process 3). The S-R bands arise from the dipole allowed photoabsorption process into discrete levels of the O_2 ($B^3\Sigma_u^-; v'$) state, followed by predissociation via a radiationless transfer to the repulsive $1^1\Pi_u$, $1^3\Pi_u$, $^5\Pi_u$, or $2^3\Sigma_u^+$ states:

$$O_2(X^3\Sigma_g^-; v'') + h\nu \rightarrow O_2(B^3\Sigma_u^-; v') \rightarrow O(^3P) + O(^3P) \tag{22}$$

(e.g., Julienne et al. 1997; Allison et al. 1986; Lin et al. 1996; Balakrishnan et al. 2000). As shown above, the product O atoms are in the ground ^3P states. Since the absorption cross sections in the region of the S-R bands vary greatly over wavelengths intervals of $\sim 10^{-4}$ nm, the cross sections must be measured with high resolution (e.g., Yoshino et al. 1984; Cheung et al. 1996; Matsui et al. 2003). High resolution absorption cross sections in the O_2 S-R Bands can be found on the CFA website (cfa-www.harvard.edu/amp/ampdata). Because the cross sections in the Schumann-Runge bands are of the order of $10^{-21}-10^{-19}$ cm^2, photons in this region of the absorption spectrum penetrate into the terrestrial mesosphere and stratosphere, where their photoabsorption is the principal O_2 dissociation process. They do not, however, affect the terrestrial thermosphere. The thermospheres of Mars and Venus do not contain enough O_2 to make photodissociation of O_2 an important as a source of O atoms.

Photoabsorption by O_2 in the wavelength range (130–175 nm) is mostly by direct absorption into the continuum of the $B^3\Sigma_u^-$ state, the S-R continuum (process 1):

$$O_2(X^3\Sigma_g^-; v'') + h\nu \rightarrow O_2(B^3\Sigma_u^-) \rightarrow O(^3P) + O(^1D). \tag{23}$$

The maximum cross section at 295 K is about 1.44×10^{-18} cm^2 near 1400 Å (e.g., Yoshino et al. 2005), and the products of this dissociation process are mostly $O(^3P) + O(^1D)$. Absorption of solar radiation by O_2 in the S-R continuum is the main source of atomic O in the terrestrial thermosphere.

Direct absorption from the ground state of O_2 to the $1^3\Pi_u$ state of O_2 is an approximate example of absorption into an excited state that has no bound state (process 2). Except for a

shallow minimum that is found in the 1.05–1.27 Å region, the potential curve is mostly repulsive (e.g., Allison et al. 1982). The photoabsorption cross sections into that state are small and smoothly varying at long wavelengths, but exhibit a sharp increase near 1358 Å, with considerable structure shortward of that wavelength (e.g., Allison et al. 1986; Balakrishnan et al. 2000).

In the wavelength range 1030 to 1300 Å, photodissociation of O_2 takes place via dipole allowed excitation of the $O_2(X^3\Sigma_g^-)$ ground state to discrete Rydberg states, such as the E, $E'^3\Sigma_u^-$ and the F, $F'^3\Pi_u$ states, which are strongly predissociated (process 3). This effect leads to highly structured cross sections, and an accidental, but important minimum appears at Lyman alpha (1216 Å). This is the "window" that allows penetration of solar Lyman alpha photons to low altitudes in the terrestrial atmosphere (e.g., Lee and Nee 2000, 2001). La Coursiere et al. (1999) have computed the relative yields of $O(^3P) + O(^3P)$ and $O(^3P) + O(^1D)$ over the solar Lyman alpha line, and have found that the $O(^1D)$ yield is about 0.58. Most of the rest of the yield in this region is to the products $O(^3P) + O(^3P)$. Only a small fraction of the dissociation produces $O(^3P) + O(^1S)$, with an upper limit less than 0.02.

Since the ionization potential of O_2 is 12.07 eV, photons shortward of 1027 Å can ionize or dissociate O_2. Jones et al. (1996) have shown that photons in the wavelength range 750 to 850 Å can excite O_2 to the I, I' and I'' Rydberg states that converge to the $O_2^+(a^4\Pi_u)$ state. In this wavelength range predissociation competes with autoionization, but, in general, predissociation is more important. Carlson (1974) has shown that absorption into these Rydberg states leads to production of one ground state $O(^3P)$ atom plus one excited state $O(^3S^o)$, which radiates to the ground state leading to the OI triplet at 1302, 1304, and 1306 Å.

2.7 Photodissociation of CO

Photodissociation of CO is important as a source of C on Venus and Mars. In the wavelength region 885 to threshold at 1118 Å, the photodissociation of CO takes place via discrete absorptions to a number of predissociating states (e.g., van Dishoeck and Black 1988). The line spacings in some of the bands are of the order of 10^{-4} Å. Fox and Black (1989) constructed high resolution cross sections for excitation to in six bands in the range 885–912 Å, and 33 bands considered by Black and van Dishoeck (1987) in the range 912–1118 Å, for a total of 39 bands to several electronic states. Fox and Black combined the computed high resolution cross sections with a model high resolution solar flux spectrum, which included measured or estimated lineshapes for the strong solar lines in this region of the spectrum. The photodissociation rates for the various bands in the Venus thermosphere were computed, and the total photodissociation rate was found to be smaller by a factor of two than those computed using the low resolution cross sections. The correction was small because CO is not the primary absorber in this region of the spectrum in the Venus atmosphere.

More recent measurements of high resolution photoabsorption cross sections for CO have been carried out for the wavelength regions 967–988 Å, and 925–974 Å by Stark et al. (1993) and Yoshino et al. (1995), respectively.

2.8 Photodissociation of N_2

Photodissociation of N_2 is potentially important for production of translationally and electronically excited N atoms in the planetary thermospheres. Low resolution cross sections for photoabsorption and photoionization of N_2 from 1 Å to the experimental threshold at 1021 Å (12.14 eV) are shown in Fig. 8. Photodissociation of N_2 in the region longward of the IP at 796 Å (15.58 eV) to 1021 Å takes place via line absorptions into discrete valence and

Rydberg states in the singlet manifold, which may decay by emission or preferably by predissociation (e.g., Helm and Cosby 1989). Although the energetic threshold for production of two ground state N atoms:

$$N_2 + h\nu \rightarrow N(^4S) + N(^4S) \tag{24a}$$

is 1270 Å (9.76 eV), the photodissociation cross sections longward of 1021 Å ($E <$ 12.14 eV) are found to be negligible. The possible channels for photodissociation of N_2 thus include

$$N_2 + h\nu(E > 12.14\text{ eV}) \rightarrow N(^4S) + N(^2D), \tag{24b}$$

$$N_2 + h\nu(E > 13.34\text{ eV}) \rightarrow N(^4S) + N(^2P), \tag{24c}$$

and

$$N_2 + h\nu(E > 14.52\text{ eV}) \rightarrow N(^2D) + N(^2D). \tag{24d}$$

For photon energies smaller than 14.52 eV, the dissociation produces one ground state and one excited state N atom. At energies larger than 14.52 eV (wavelengths shortward of 854 Å), in addition to line absorptions, there may also be some photodissociation directly into the continua of singlet *ungerade* repulsive states that result in the production of channel (24d) above (Michels 1981; Walter et al. 1993). Shortward of the ionization threshold at 796 Å ($E > 15.58$ eV) the photoabsorption cross sections are highly structured, and autoionization competes with predissociation. Photodissociations via the channels

$$N_2 + h\nu(E > 15.7\text{ eV}) \rightarrow N(^2D) + N(^2P) \tag{24e}$$

$$N_2 + h\nu(E > 16.9\text{ eV}) \rightarrow N(^2P) + N(^2P) \tag{24f}$$

are also possible, although the photoabsorption and photodissociation cross sections are difficult to measure in this spectral region (G. Stark, private communication, 2008).

In the highly structured regions of the N_2 photoabsorption spectrum, ultrahigh resolution cross sections and predissociation probabilities are required in order to quantitatively model the production of N atoms. Cross sections with resolutions of the order of $\sim 6 \times 10^{-3}$ Å are currently being measured by, for example, Stark et al. (2005, and references therein) and

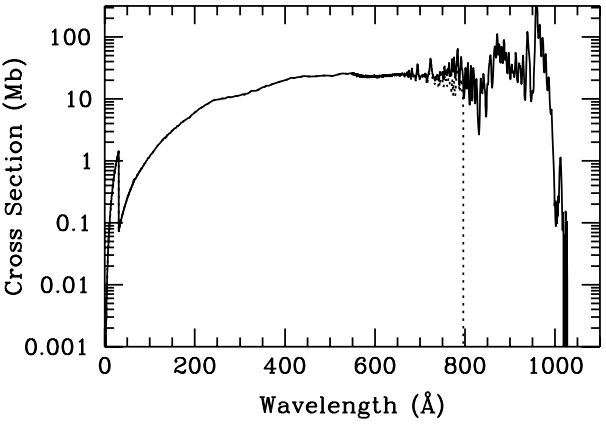

Fig. 8 Low resolution N_2 photoabsorption cross sections (*solid curve*). The photoionization cross sections are represented by the dotted curve. The experimental threshold for photodissociation is about 1021 Å (12.14 eV). In the highly structured region shortward of the ionization threshold at 796 Å predissociation and autoionization compete. Below about 650 Å the photoabsorption and photoionization cross sections are equal

Sprengers et al. (2005, and references therein). Lewis et al. (2005, and references therein) have computed predissociation lifetimes. Calculations carried out with lower resolution cross sections and low resolution solar fluxes can be considered to be accurate to a factor of only a few.

In addition, branching ratios to the various possible channels (24b–24f) must be known over the entire range of photodissociation. These data are not available, except for some information at energies less than 14.52 eV (see Fox 2007 for a review of this subject). Although progress is being made in determining high resolution cross sections and product yields of N_2, not enough information is currently available to accurately compute the production rates of various states of N atoms or the total photodissociation rate of N_2 in thermospheres/ionospheres of the earth, Venus, Mars, Titan or Triton.

2.9 Photodissociation of CO_2

The photoabsorption cross sections of CO_2 are also highly structured. Temperature dependent cross sections have been measured by Stark et al. (2007) from 1061 to 1187 Å with a moderate resolution of 0.05–0.1 Å. The values of the cross sections range from 5×10^{-16} to 2×10^{-20} cm^2 at 195 K, and thus photons in this region of the spectrum are absorbed over a wide altitude range in the atmospheres of Mars and Venus. In the wavelength region 1187 to 1755 Å, the CO_2 photoabsorption cross sections exhibit considerable structure. Photoabsorption cross sections in the 1178.08 to 1633.99 Å range have been measured by Yoshino et al. (1996) at moderate (~ 0.05 Å) resolution, and are available on the CFA website referenced above. Anbar et al. (1993) showed that the use of moderate resolution temperature dependent cross sections in the 1225 to 1970 Å region changed the CO_2 photolysis rates in the Martian lower atmosphere by about 33%, and those of H_2O by 950% as compared to those arising from the use of cross sections averaged over 50 Å bins.

2.10 Photodissociation of H_2

Dissociation of H_2 has a thermodynamic threshold of 4.48 eV (2769 Å), but the photoabsorption cross sections longward of 1116 Å are negligible. Photodissociation in the wavelength region 845–1116 Å proceeds largely by dipole-allowed absorption from the ground $X^1\Sigma_g^+(v'')$ state into discrete states, including $B^1\Sigma_u^+(v')$, $C^1\Pi_u(v')$, $B'^1\Sigma_u^+(v')$, and $D^1\Pi_u(v')$, which may then radiate either to the discrete levels of the ground state, producing emission, or to the continuum of the ground state, producing dissociation to form two H($1s$) atoms (e.g., Dalgarno et al. 1970; Abgrall et al. 1997). The $B^1\Sigma_u^+(v')$ and $C^1\Pi_u(v')$ states are the upper states of the Lyman and Werner band systems, respectively, of H_2. Black and van Dishoeck (1987) have investigated these processes as they relate to the interstellar medium, where only radiation longward of the H ionization threshold of 912 Å is important. They found that about 10–15% of the initial line absorptions fluoresce to the continuum of the $X^1\Sigma_g^+(v'')$ state.

Except for a small contribution from predissociation of the $D^1\Pi_u$; v' state for $v \geq 3$ (e.g, Mentall and Gentieu 1970), these excited states are not predissociated in the usual sense because no suitable crossings to repulsive states are available. The lowest purely repulsive state of H_2 is the $b^3\Sigma_u^+$ state (Herzberg 1950), which, because of dipole selection rules, cannot be significantly populated by photoabsorption. Shortward of 845 Å, direct absorption into the continua of the $B^1\Sigma_u^+$, $C^1\Pi_u$, $B'^1\Sigma_u^+$, and $D^1\Pi_u$ states dominates the photodissociation. The cross sections for these processes are substantial, and the products of dissociation are one H($1s$) atom and one H($2s$, $2p$) (e.g., Glass-Maujean 1986).

Autoionization of H_2 begins to compete with dissociation shortward of the ionization threshold at 803 Å, and the cross sections exhibit complicated structure in this region, which has not been fully analyzed (e.g., Yan et al. 1998). For example, dissociation of the $B''\bar{B}^1\Sigma_g^+$ double-welled state proceeds by radiation to the continuum of the $B'^1\Sigma_u^+; v'$ state, with a rate of the order of 5×10^{10} s^{-1} (e.g, Glass-Maujean et al. 2007).

In environments in which H_2 is the major absorber, such as the thermosphere of Jupiter, radiation shortward of 912 Å is important. Significant effects of discrete absorption on the atmospheric absorption profiles are predicted. Kim and Fox (1991, 1994) used the compilations of oscillator strengths, transition probabilities, and fluorescent dissociation fractions of Black and van Dishoeck (1987) and some additional lines provided by J. H. Black (private communication, 1990) shortward of 912 Å to construct high resolution H_2 photoabsorption cross sections. Kim and Fox combined these cross sections with a similarly high resolution solar flux spectrum, and found that, in the Jovian atmosphere, solar radiation in the line centers penetrates to only 420 km above the ammonia cloud tops, but in the wings of the photoabsorption lines, two strong solar lines, CIII at 977.02 Å and OVI at 1031.91 Å, and about 30% of the continuum, penetrate 100 km further to below the methane homopause, where the production of a layer of hydrocarbon ions was predicted.

2.11 Photodissociation of Hydrocarbons

The photoabsorption cross sections for methane fall off rapidly longward of about 1450 Å (e.g., Lee and Chiang 1983), but other hydrocarbons expected to be found below the methane homopauses of the giant planets, such as acetylene, ethane, and ethylene, absorb at longer wavelengths. The cross sections are found, however, to be highly structured and temperature dependent. Photoabsorption cross sections for acetylene have been measured, for example, by Smith et al. (1991) at a resolution of $\sim 0.1-0.5$ Å. Temperature dependent cross sections for ethylene have recently been measured with a resolution of 0.6 Å by Wu et al. (2004). For other hydrocarbons, the reader is referred to the *science-softCon UV/Vis Spectra Data Base*, in which the available data on photoabsorption of hydrocarbons and other molecules of atmospheric interest are summarized and presented (Noelle et al. 2007; see also Huestis et al. 2008).

2.12 Heating by Absorption of Solar Photons and Heating Efficiencies

The heating efficiency is usually defined as the fraction of solar energy absorbed that is deposited locally as heat. Solar energy is transformed into heat in photodissociation and photoelectron-impact dissociation of molecules, and in exothermic reactions, including ion-molecule reactions, neutral-neutral reactions, and dissociative recombination of ions with electrons. Quenching (or collisional deactivation) of metastable ions, such as $O^+(^2D)$, or neutrals, such as $O(^1D)$ or $N(^2D)$, is a particularly important class of reactions that lead to heating. A major uncertainty in modeling heating efficiencies is determining the fraction, f_v, of the exothermicities in these processes that appears as vibrational excitation of molecular products. Vibrational excitation usually leads to cooling either by direct radiation to space for heteronuclear diatomics or polyatomics, or by vibrational energy transfer from homonuclear diatomics to heteronuclear species, and subsequent radiation. By contrast rotational and translationally excited products are thermalized rapidly.

In photodissociation, the amount of energy that appears as kinetic energy is the difference between the energy of the photon and the dissociation energy (which may include some electronic excitation of the fragments). The energy that appears as vibrational excitation in

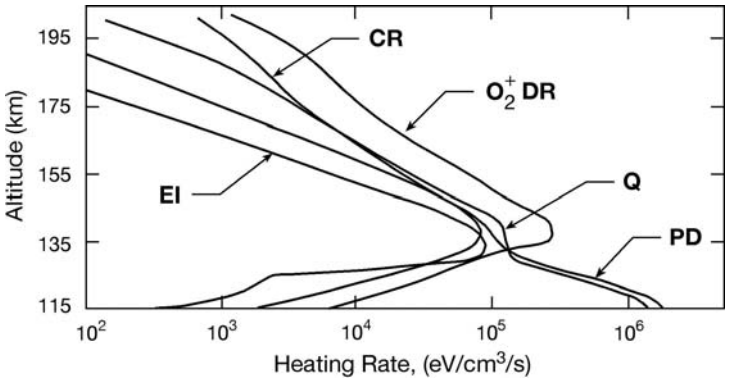

Fig. 9 Altitude profiles of computed heating rates in the Venus thermosphere. The *curve labeled CR* represents the heating rate due to exothermic chemical reactions; the *curve labeled* O_2^+ *DR* is that due to dissociative recombination of O_2^+; the *curve labeled Q* represents the heating due to quenching reactions of metastable species; the *curve labeled PD* is the heating rate due to photodissociation; the *curve labeled EI* is that due to electron impact processes. Adapted from Fox (1988)

photodissociation is found to be small, of the order of 25%. A half-collision model suggests that this fraction is particularly small if one of the fragments is light, such as H or H_2. Vibrational excitation fractions of 10–15% are indicated for this case (cf., Fox 1988, and references therein). In suprathermal electron-impact dissociation, most of the energy is carried away by the electron, and the energy that appears as translation has been found to be of the order of 1 eV (cf., Fox and Dalgarno 1979).

Exothermic ion-neutral and neutral-neutral reactions can be a significant source of heating for the ions and neutrals. The energies of the atomic products are determined by conservation of momentum and energy, but if there are molecular products, some of the available energy can appear as vibrational excitation. That fraction depends on the mechanism of the reaction, and is generally greater for reactions that proceed via a collision complex than those that proceed via a direct insertion/decomposition mechanism. Energy tends also to be deposited in vibration when a new bond is formed. In quenching of metastable species, such as $O(^1D)$, especially those that proceed via the formation of a collision complex, a significant (usually statistical) proportion of the energy can appear as vibrational excitation of the molecular products.

The most important reactions for heating on Venus and Mars are generally dissociative recombination reactions (see (8)). DR reactions tend to be very exothermic, and are the main loss process for ions whose parent neutrals have low ionization potentials. For DR of diatomic molecules, all the exothermicity that does not appear as electronic excitation appears as heat.

Fox (1988) computed the heating rates and efficiencies for a high solar activity model of Venus. The heating rates due to various processes are shown in Fig. 9. It can be seen that the most important source of heating is the DR reaction of the major molecular ion, O_2^+, above about 130 km. Below that altitude the most important sources of heat are almost equally photodissociation and quenching of metastable species. Electron impact dissociation and chemical reactions other than DR or quenching of metastable species are unimportant. Altitude profiles of resulting heating efficiencies are shown in Fig. 10a. The heating efficiency curve labeled "A" is for the standard model, and that labeled "B" is a lower limit. The lower limit model is based on extreme assumptions about the fraction of energy being deposited

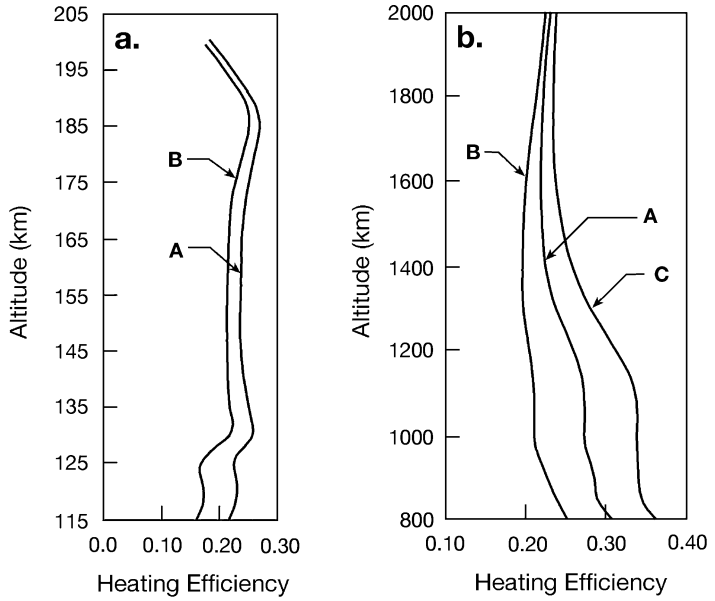

Fig. 10 Altitude profiles of heating efficiencies in the atmospheres of (**a**) Venus (adapted from Fox 1988) and (**b**) Titan (Fox and Yelle, unpublished calculations). The *curves labeled A* are from the standard models; those *labeled B* are lower limits. The *curve labeled C* in (**b**) is the upper limit for the Titan model (see text)

as vibrational excitation. The heating efficiencies range from 16 to 22% at altitudes near 100 km. A similar model for Mars exhibits heating rates and efficiencies that are comparable to those obtained for Venus (Fox et al. 1995).

By contrast, the heating rates on Titan are not dominated by DR reactions, partly because the dominant ions have been "processed more", that is, they have been transformed via many ion–molecule reactions before they can recombine. In addition, since most of the DR reactions are of polyatomics, some of the exothermicity may appear as vibration of the fragments produced. DR of N_2^+ is not an important heat source because N_2 has a high ionization potential, and therefore in the region near and for a significant distance above the main ion peak, N_2^+ tends to destroyed by ion–molecule reactions, rather than by DR. The main sources of heat are found to be photodissociation of N_2 and CH_4, and neutral-neutral chemical reactions. The standard "best guess" and upper and lower limits for the heating efficiencies on Titan are presented in Fig. 10b. These heating efficiency profiles correspond to different assumptions about the fraction of the exothermicities that appears as vibrational excitation in different processes. For example, in neutral-neutral and ion-neutral reactions, fractions of 60%, 40% and 80% are assumed for the standard, upper limit and lower limit models. The heating efficiencies are found to be in the range 25–35% at the lower boundary, and decrease with altitude to values near 22% at the top boundary of the model near 2000 km.

Roble et al. (1987) computed the heating efficiencies in the terrestrial thermosphere, and reported values that increased from 30% at about 100 km to $\sim$ 55% near the F_1 peak ($\sim$ 175 km) and then decreased to $\sim$ 30% near the exobase at 400–500 km. The main sources of heat for the earth are similar to those for Titan, and are photodissociation of O_2 in the Schumann-Runge continuum, and exothermic neutral–neutral reactions. The heating rates are significantly larger than those for Venus and Mars. The reasons for this are various,

but may be related to the fact that the major metastable species in the terrestrial ionosphere ($N(^2D)$ and $O(^1D)$) have long radiative lifetimes and are therefore quenched before they can radiate. The major metastable species produced on Venus and Mars, $CO(a^3\Pi)$, is characterized by a short radiative lifetime that exhibits a strong dependence on vibrational and rotational levels, and is in the range $\sim 3-150$ ms (e.g., Jongma et al. 1997). The $CO(a^3\Pi)$ state therefore mostly emits to the ground $X^1\Sigma$ state, producing the Cameron bands, before it can be quenched.

Also, the major species on Venus and Mars, CO_2, is a triatomic molecule. Its interaction with photons and electrons, and its chemical reactions, produce more molecular species for which the exothermicity can be taken up as vibrational excitation, than do reactions of O_2 and N_2 in the terrestrial atmosphere.

2.13 Auger Electrons and Characteristic X-rays

Measurements of doubly charge ions in the terrestrial thermosphere began with the Atmosphere Explorer in the mid 1970's, and in the Venus ionosphere by Pioneer Venus beginning in 1978. Since then, many models of altitude profiles of doubly charged ions densities have been constructed. The first studies were of O^{++} in the terrestrial and Venus atmospheres. More recently, studies of O^{++} and doubly charged molecular ions on other bodies have been carried out. The mechanisms for the production and loss of these ions are uncertain. The production processes include double valence shell ionization and Auger ionization, which may be produced by absorption of X-rays or by impact of very energetic particles. Signatures of Auger ionization have been identified in suprathermal electron flux measurements or predicted by models. Little is known about the loss processes for doubly charged ions, which complicates their modeling.

In addition, measurements of X-rays from various solar system bodies have been made, and their sources have been modeled. We describe the ways in which X-rays interact with atmospheric species, the cross sections for various competing processes, and the mechanisms for emission of X-rays that have been identified for various solar system bodies. We begin by describing the Auger effects and the production of characteristic X-rays.

Most atmospheric molecules are made up of atoms with atomic numbers $Z < 10$, and therefore only the K-and L-shells, defined as those characterized by principal quantum numbers $n = 1$, and $n = 2$, respectively, are populated in the ground states. The ground state of the noble gas He ($Z = 2$) has a filled K-shell with electron configuration $1s^2$; Ne ($Z = 10$) has filled K and L shells with electron configuration $1s^2 2s^2 2p^6$. Ar ($Z = 18$), a minor constituent in planetary atmospheres, has electrons in the ($n = 3$) M-shell; its ground state electron configuration is $1s^2 2s^2 2p^6 3s^2 3p^6$. Metals and other atoms that are formed from ablation of meteors in the mesospheres/thermospheres of planets also have electrons in levels with principal quantum numbers greater than 2. These atoms include, for example, Na (11), Mg (12), Si (14), Ca (20), and Fe (26), where the atomic numbers Z are shown in parentheses. Meteoric ion layers are present in all planetary atmospheres with substantial neutral densities.

The first ionization potentials of atoms and molecules, which are listed in Table 1, pertain to the ejection of outer shell electrons, which are fairly loosely bound. An inner K-shell or "core" ($1s$) electron can be ejected from an atom by absorption of an energetic photon or via a collision with an energetic electron. For atoms with atomic numbers greater than 4, the core-ionizing photons must be in the X-ray region of the spectrum, and the impinging electrons must be characterized by energies of the order of kilovolts.

After the ejection of the core electron, an electron in the L-shell may then make a transition to the $1s$ orbital. Selection rules for one-electron jumps (i.e., $\Delta\ell = \pm 1$) require that

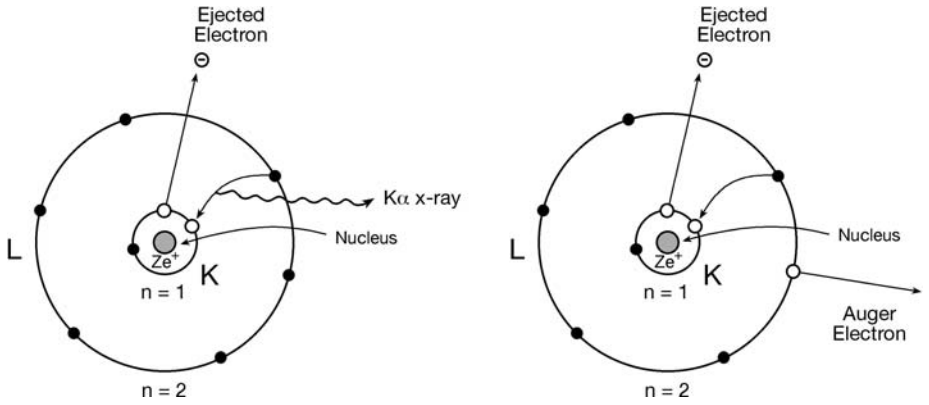

Fig. 11 Cartoon that represents the production of characteristic X-rays and Auger electrons. Only the K and L shells are shown. (*Left*) Characteristic X-rays are produced when absorption of an X-ray photon or energetic charged particle causes the ejection of a K-shell electron (*labeled "Ejected electron"*). An outer shell electron the makes transition to fill the hole in the inner shell. In this process, the excess energy is carried away by a $K\alpha$ X-ray. The ion is left in a singly ionized state. (*Right*) Auger electrons are produced by a similar sequence, except that the excess energy released in reorganization of the ion is carried away by an energetic "Auger" electron, which leaves the ion in the ground or an excited doubly ionized state

this electron be a $2p$ electron. The energy released in the decay of the core ionized state of the ion may be carried away by a characteristic X-ray of approximate energy,

$$E = 13.6(Z-1)^2\left(\frac{1}{{n_1}^2} - \frac{1}{{n_2}^2}\right)\text{eV}. \tag{25}$$

In this equation n_1 is the principal quantum number of the ejected electron and n_2 is the principal quantum number of the valence electron that replaces the inner electron. The characteristic X-ray is designated as "Kα" for $n_1 = 1$ and $n_2 = 2$. The English physicist H. G. C. Moseley studied this effect, which allowed him to determine the atomic numbers of many elements. This simple formula (25) yields energies of 255, 367, 499 and 2947 eV for the Kα X-rays for the atmospherically important atoms C, N, O, and Ar, respectively. If an atom has electrons in the shells with $n \geq 3$, it may, after ejection of an electron from the L-shell, produce a characteristic $L\alpha$ X-ray, which corresponds to $n_1 = 2$ and $n_2 = 3$ in (25). Kβ X-rays may also be emitted, if, after core ionization, an electron from the $n = 3$ (M-shell) drops down to fill the core hole; this corresponds to $n_1 = 1$ and $n_2 = 3$ in (25).

Alternatively, as the valence electron drops down to fill the vacancy in the K-shell, the excess energy may be carried away by the ejection of an outer shell electron, leaving the ion in a doubly ionized state. This ejected "Auger electron" is named after the physicist Pierre Auger, who discovered the phenomenon in the 1920's. These alternatives for relaxation of a core-hole ion are illustrated in Fig. 11. Alternatively, a related phenomenon, the radiative Auger process, may take place; here the excess energy is shared by the Auger electron and a simultaneously emitted photon (e.g., Mühleisen et al. 1996; Penent et al. 2005). For light elements, such as those that are found in the atmospheres of the planets, the Auger process is more important than the emission of characteristic X-rays, while the reverse is true for heavy elements. This is due to the increasing importance of photon emission as the atomic number increases, rather than to a decrease in the probability of ejection of an Auger electron (e.g., Condon and Shortley 1964). Krause (1979) has summarized the X-ray emission and Auger yields for K and L shells for atoms with $5 \leq Z \leq 110$, and showed that they are

equally probable for an atomic number of about 31. The Auger yields are 0.997, 0.995, and 0.992, and 0.882 for C, N, O and Ar, respectively. The thresholds for core ($1s^{-1}$) ionization of C, N, O and Ar are 291 eV (42.6 Å), 404.8 eV (30.6 Å), 538 eV (23.0 Å), and 3203 eV (3.87 Å), respectively, (e.g., Verner and Yakovlev 1995) and the Kα X-rays are characterized by wavelengths of 43.7, 30.9, 23.3, and 3.87 Å, respectively (Lide 2008).

We shall describe the details of these processes, specifically for atomic oxygen in the text that follows. The K-shell ionization of O by an X-ray or keV electron can be represented by

$$\mathrm{O}(1s^2s^22p^4) + (h\nu, e^*, [E > 538\ \mathrm{eV}]) \rightarrow \mathrm{O}^{+*}(1s2s^22p^4) + (e, 2e), \tag{26}$$

where O^{+*} represents a core-hole ion. In (26) the electron configurations of the ground state of the neutral and of the core-ionized ion are shown explicitly. After the ejection of the $1s$ electron, an outer L-shell electron may make a transition to the inner shell to fill the vacancy left by the ejected electron; this may be followed by the emission of a characteristic $K\alpha$ X-ray photon, e.g.,

$$\mathrm{O}^{+*}(1s2s^22p^4) \rightarrow \mathrm{O}^{+}(1s^22s^22p^3) + h\nu\ (\sim 23.6\,\text{Å}). \tag{27}$$

In the competing Auger process, after the ejection of the core electron, as the outer shell electron makes a transition to fill the core hole, the excess energy may be carried away by emission of an Auger electron from an outer shell, e.g.,

$$\mathrm{O}^{+*}(1s2s^22p^4) \rightarrow \mathrm{O}^{++}(1s^22s^22p^2) + e\,(\text{Auger}). \tag{28}$$

The energy of the Auger electron may be approximated as that of the $K\alpha$ X-ray minus the binding energy of the $n = 2$ electron. For O^+, the binding energy of the outer electron is approximately equal to the second ionization potential, ~ 35 eV, so that the Auger electrons are expected to have energies of about 500 eV.

This energy is, however, only an approximation. In fact, the core excited O^{+*} ion with electron configuration ($1s2s^22p^4$) ion actually corresponds to any of four electronic states with term symbols $^4P_{5/2,3/2,1/2}$, $^2P_{3/2,1/2}$, $^2D_{5/2,3/2}$ and $^2S_{1/2}$. Only the ^4P and ^2P states, however, have been observed experimentally from the $\mathrm{O}(^3P)$ ground state (e.g., Petrini and de Araújo 1994). The energies of the $^2P_{3/2}$ and $^2P_{1/2}$ states have been computed by Lohmann and Fritzsche (1996) to lie 4.675 and 4.708 eV, respectively, above the lowest $^4P_{5/2}$ state. The $^4P_{3/2}$ and $^4P_{1/2}$ fine structure levels lie 0.04 eV and 0.053 eV, respectively, above the $^4P_{5/2}$ level.

The $K\alpha$ X-rays may arise from any of ten dipole allowed transitions from the two observed core-excited O^+ states to the three electronic states characterized by the ground state electron configuration $1s^22s^22p^3$, including the ground $\mathrm{O}^+(^4S^{\mathrm{o}}_{3/2})$, and the excited $\mathrm{O}^+(^2D^{\mathrm{o}}_{5/2,3/2})$, and $\mathrm{O}^+(^2P^{\mathrm{o}}_{3/2,1/2})$ states; the energies of the latter two states are about 3.32 and 5.02 eV, respectively, above the ground state. The allowed radiative transitions between the core hole upper O^+ states and the lower states with the ground state electron configuration obey the dipole selection rules for radiative transitions: $\Delta S = 0$, $\Delta L = 0, \pm 1$; $\Delta J = 0, \pm 1$; $L = 0 \nleftrightarrow L = 0$; $J = 0 \nleftrightarrow J = 0$; e $\leftrightarrow$ o). Thus the X-rays produced in dipole-allowed transitions will be characterized by slightly different energies and intensities, and the $K\alpha$ "line" actually represents a series of closely spaced lines.

In the Auger process (see (28)) a radiationless transition takes place between the core hole ^4P and ^2P states of O^+ and the final O^{++} states. The end state with electron configuration $\mathrm{O}^{++}(1s^22s^22p^2)$ comprises three electronic states ^3P, ^1D, and ^1S with Auger electron energies in the range 492–498 eV; six states comprise the O^{++} final state with

electron configuration $1s^2 2s 2p^3$: $^5S^o$, $^3D^o$, $^3P^o$, $^1D^o$, $^3S^o$, and $^1P^o$ with Auger energies in the range 470–491.6 eV; three states of O^{++} are associated with the electron configuration $1s^2 2p^4$: ^3P, ^1D, and ^1S with Auger energies in the range 452–461 eV above the ground state. The total angular momentum quantum numbers J for these terms have been suppressed for compactness. The more stringent selection rules for Auger transitions apply to this process ($\Delta L = \Delta J = 0$; $\Delta S = 0$; $\Delta M_L = \Delta M_S = 0$) (Craseman 2006). Figure 12 illustrates some of the processes that may occur after ejection of a $1s$ electron from oxygen by absorption of an X-ray photon or a collision with a keV electron.

Ten oxygen Auger transitions were observed for Auger electron energies from 465 to 505 eV by Caldwell and Krause (1993). Figure 13 shows an Auger electron spectrum for atomic oxygen. Lohmann and Fritzsche (1996) have computed the energies and the rates of 59 transitions between the core-hole O^{+*} $^4P_{5/2,3/2,1/2}$ and $^2P_{3/2,1/2}$ states and the fine structure levels of the O^{++} states listed above. In general, the dominant Auger transitions are those that terminate on the O^{++} $(1s^2 2s^2 2p^2\, ^3P)$ ground state configuration, but several other transitions are predicted to occur with significant probabilities.

If the O^{++} ion is left in an excited state after ejection of the Auger electron, photons may be emitted that arise from dipole allowed transitions to a lower state. Figure 12 illustrates one example of a radiative transition from the excited $O^{++}(1s^2 2s 2p^3)$ $^3P^o$ state to the ground $O^{++}(1s^2 2s^2 2p^2)^3P$ state. This transition results in the appearance of a multiplet which is characterized by the emission of photons in the 702–704 Å range.

2.14 The Auger Effect and Double Valence Shell Ionization in Molecules

In atmospheric molecules, such as N_2, CO, NO, CO_2, and O_2, the inner shell electrons are tightly held around the atomic nuclei, and have large binding energies. By contrast, the valence electrons are in more diffuse molecular orbitals that surround all the nuclei. These electrons are more loosely held and are characterized by much smaller binding energies, which differ, however, from those for the constituent atoms. In addition, the Auger spectra of molecules are more complex than those of atoms. For example, 22 peaks have been identified in the Auger spectrum of O_2 compared to 10 peaks for that of O (e.g., Larsson et al. 1990).

In general, the thermodynamic limit for dissociation of the doubly charged molecular to fragment ions lies below that for production of the doubly excited ion. (A noteworthy exception to this rule is the $CaCl^{++}$ ion, for which the $^2\Pi_{3/2,1/2}$ states are stable by 0.87–0.95 eV (Wright et al. 1997)). Almost all states of doubly charged ions are inherently unstable or metastable against dissociation to two ionized fragments in a "Coulomb explosion". This process can take place via predissociation or through tunneling through the Coulomb barrier. This fragmentation is an important effect that differentiates atomic and molecular Auger processes.

The identification of electronic states of doubly ionized molecules, their potential energy curves, and decay processes have been the subject of numerous investigations over the last $\sim$ 40 years. Mathur (1993, 2004) has reviewed the subject of multiply charged molecules. In many cases, the identification of the ground state is not yet secure. It is difficult to determine the second ionization potential (IP) of a molecule, which is not necessarily the same as the appearance potential for production of doubly ionized species by photons or charged particles. The appearance potential is the minimum energy for double ionization by a vertical (Franck-Condon) transition; the doubly ionized molecules produced may then fragment into ions with substantial kinetic energy.

Theoretical studies of doubly ionized molecules have included calculation of potential energy curves, the Coulomb barriers and identification of states responsible for predissociation of these ions. Many experimental studies of doubly ionized molecules have focused

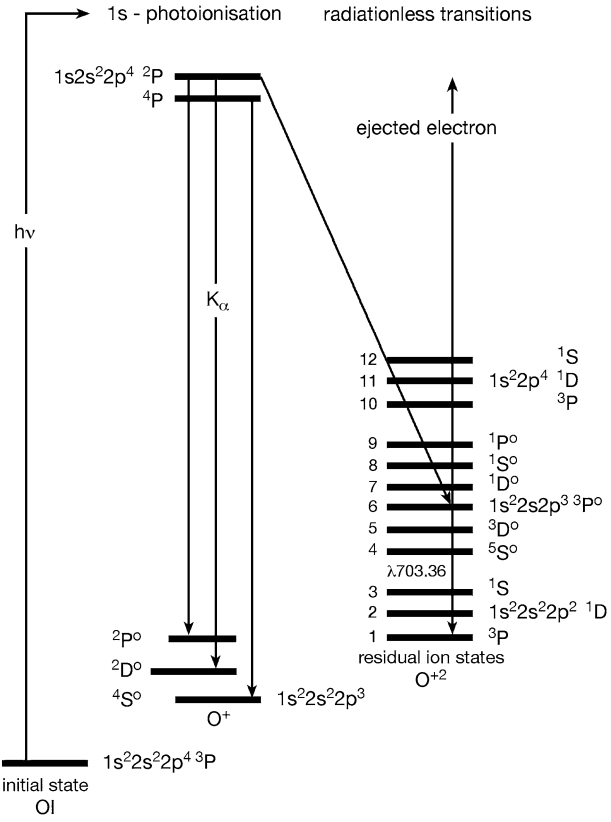

Fig. 12 Diagram of the states involved in the production of $K\alpha$ X-rays and Auger electrons from atomic oxygen (not to scale). (*Left*) An X-ray (or energetic particle) causes the ejection of a "core" ($1s^{-1}$) electron (*middle*) One of the core-ionized states of O^+ (^4P or ^2P) is produced. A $K\alpha$ photon is emitted in the transition from one of these states to any of the three states of O^+ with ground state electron configuration, $1s^2 2s^2 2p^3$. (*Right*) Alternatively, a radiationless transition to one of the states shown on the right may occur (although selection rules must be obeyed). For each transition, an Auger electron is produced with a different energy. The figure also shows a radiative transition between the O^{++} $^3P^o$ state, which may be produced in Auger decay, and the ground ^3P state. A photon with wavelength of 702–704 Å is produced. (Adapted from Petrini and de Araújo 1994)

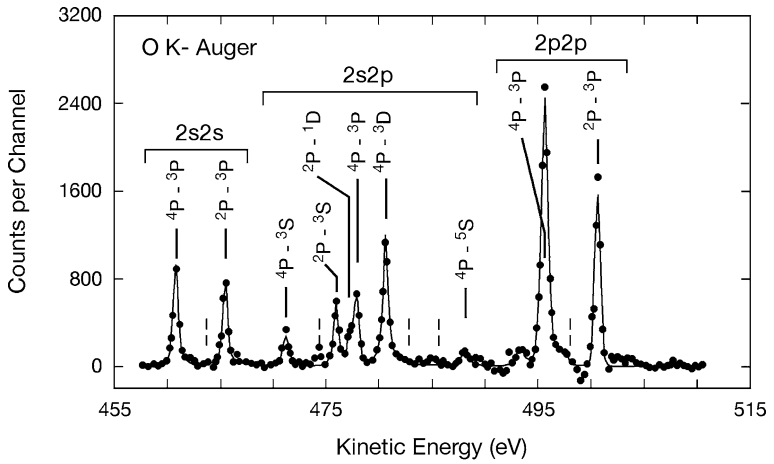

Fig. 13 K-shell Auger spectrum of atomic oxygen, showing 10 discrete transitions. The experimental points are shown; the *solid curve* is a fit to the data. The vertical *dashed lines* indicate transitions from the ^2P state that are too weak to measure. Adapted from Caldwell and Krause (1993). Copyright 1993 by the American Physical Society

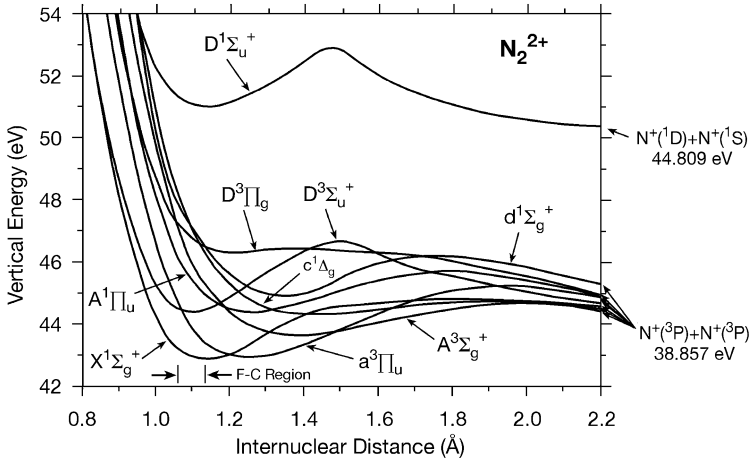

Fig. 14 Potential curves of some low-lying states of N_2^{++}. The energy scale on the *vertical axis* is relative to the $v = 0$ ground state of N_2, and the Franck-Condon region from this state is indicated at the *bottom*. The energy of the $N_2^{++}\ ^1\Sigma_g^+ (v'' = 0)$ state relative to the ground state is 43.0 eV. See text for a discussion of the various potential curves. From Lundqvist et al. (1996). Reprinted by permission of IOP Publishing, Ltd

on the Auger electron spectra (e.g., Moddeman et al. 1971), which is an important tool to investigate the properties of doubly charged ions. Recently a more powerful tool, the photoelectron-Auger electron coincidence method has been developed (Penent et al. 2005). In Kinetic Energy Release (KER) experiments, the distributions of fragment ions that arise from decay of doubly ionized molecules are determined. In order to study the KER spectrum of a doubly charged ion, the lifetime of the ion must be in the "experimental window", which is generally less than of 100's of ns.

A wide range of lifetimes of doubly ionized molecules has been found, which complicates studies of their properties. The lifetime of the doubly ionized molecule depends strongly on its electronic state, and the details of its potential curve, including the availability of curve crossings which can predissociate it, and the width of the Coulomb barrier, which varies with the vibrational energy level of the doubly charged molecular ion. Lifetimes range from many seconds to several μs for low vibrational levels of discrete "quasi-bound" states with large Coulomb barriers, to nanoseconds for states that are observed in Kinetic Energy Release (KER) spectroscopy to picoseconds for states whose potential curves are characterized by very shallow minima. Often the higher vibrational levels of a state may be characterized by lifetimes that are too short to be detectable, while those of lower vibrational levels have been inferred to be as long as μs (e.g., Curtis and Boyd 1984). In a seminal study, Mathur et al. (1995) investigated the lifetimes of multiply charged molecular ions using an ion storage ring. They found that all the doubly charged ions studied had components with lifetimes that were of the order of seconds or more.

We will illustrate the molecular Auger process and the related process of double valence ionization specifically for N_2, which, has been the subject of many experimental investigations in the last several decades, including Auger electron spectroscopy (e.g, Moddeman et al. 1971; Svensson et al. 1992, and references therein), X-ray absorption spectroscopy, (e.g., Shigemasa et al. 2002; Svensson 2005 and references therein), photofragment spectroscopy (e.g., Martin et al. 1994; Larsson et al. 1992; Cosby et al. 1983; Sundström et al. 1994), ion coincidence Kinetic Energy Release experiments (e.g, Stockdale 1977; Brehm and de Frênes 1978; Lundqvist et al. 1996), electron–ion coincidence (e.g, Benndorf et al. 1998;

Hsieh and Eland 1996; Fainelli et al. 2002), and translational energy spectroscopy (e.g., Mathur et al. 1995). Double ionization of N_2 by electron impact has been studied by Märk (1975) from threshold (~ 43 eV) to 170 eV. Ab initio calculations include, for example, those by Wetmore and Boyd (1986), Taylor and Partridge (1987), Koslowski et al. (1991), and Mathur et al. (1995). Figure 14 from Lundqvist et al. (1996) shows some of the low-lying potential curves of N_2^{++}, and indicates the Franck-Condon region from the ground state of N_2. We will discuss some of the features of N_2^{++} by reference to this figure.

In a molecule, as in an atom, an inner shell electron may be ejected by absorption of an X-ray photon, a keV electron, or a heavy charged particle (e.g., Edwards and Wood 1982)

$$N_2 + (h\nu, e^*) \rightarrow N_2^{+*} + (e, 2e), \tag{29}$$

where the asterisk represents an excited core hole state of the molecular ion. The K-shell ionization threshold of N_2 is 409.9 eV, compared to 404.8 eV for an atomic N (e.g., Shigemasa et al. 2002). Just as for core-ionized atoms, a valence electron may make a transition to fill the core hole, and the excess energy may be carried away by ejection of an outer shell Auger electron:

$$N_2^{+*} \rightarrow N_2^{++} + e^* \text{ (Auger)}. \tag{30}$$

This process occurs on a femtosecond time scale (Benndorf et al. 1998). As with small atoms, small core hole molecular ions may emit characteristic X-rays, but Auger processes are more probable. Subsequent fragmentation of the doubly charged N_2^{++} ion produces N^+ ions with kinetic energies of the order of a few electron volts:

$$N_2^{++*} \rightarrow N^+ + N^+ + \Delta E. \tag{31}$$

The states shown in Fig. 14, except for the $D^1\Sigma_u^+(v')$ state dissociate to two ground state N^+ ions.

The $v'' = 0$ level of the ground $^1\Sigma_g^+$ state of N_2^{++} lies about 43 eV above the $^1\Sigma_g^+(v = 0)$ ground state of N_2 (Benndorf et al. 1998; Lundqvist et al. 1996), whereas the minimum energy for production of two ground state $N^+(^3P)$ fragment ions with zero kinetic energies from N_2 is about 38.9 eV, about 4 eV below that for production of the doubly charged ion. The ground state of N_2^{++} shown in Fig. 14 exhibits a deep well, and supports a large number of long-lived vibrotational levels. Higher excited states of N_2^{++} may, however, be produced in the Auger process.

A wide range of heights of the Coulomb barriers are apparent for all the states. Highly vibrationally excited levels in the "quasi-bound" states may tunnel through the Coulomb barrier, while lower vibrationally excited levels may predissociate via a repulsive curve crossing. The ground $X^1\Sigma_g^+$ and $a^3\Pi_u$ states can be seen to have large Coulomb barriers for low vibrational levels, and significant lifetimes are predicted for these states. Mathur et al. (1995) found that a significant N_2^{++} component exists with lifetimes of the order of 3 s.

Hsieh and Eland (1996) identified eight electronic states of N_2^{++} in the Franck-Condon region, although the ground $X^1\Sigma_g^+$ and the $c^3\Sigma_u^+$ (identified in Fig. 14 as $D^3\Sigma_u^+$) states were not observed, apparently because the vibrational states accessible are too low for tunneling through the Coulomb barriers. The energies of the N^+ ions produced by the absorption of 48.4 eV photons were observed to range from 5 to 10 eV. In this experiment, the lifetimes of the doubly ionized N_2^{++} states observed in KER distributions of fragment ions produced from decay of doubly ionized states were on the order of 100's of ns.

Excited doubly charged ions may be optically active, and they may be studied by photofragment spectroscopy (e.g., Cosby et al. 1983; Larsson et al. 1992). The N_2^{++}

$A^1\Pi_u(v')$ and $D^1\Sigma_u^+(v')$ states are connected to the ground $X^1\Sigma_g^+(v'')$ states by optically allowed transitions. These states were studied by Lundqvist et al. (1995, 1996), who observed KER spectra with 19 vibrationally resolved peaks. The $A^1\Pi_u$ state supports 9 or 10 metastable bound states; vibrational levels with $v \geq 7$ were observed, with lifetimes ranging from 1 ns to $\sim$ 300 ns. Larsson et al. did not observe the vibrational levels for $v < 7$ in their experiment; they were inferred to have lifetimes greater than 10 μs. The method of decay for the high vibrationally excited states was assumed to be tunneling or predissociation. A broad peak in the KER spectrum may correspond to excitation to the purely repulsive part of the $A^1\Pi_u$ state. Because the potential curves of the $N_2^{++}(A^1\Pi_u)$ state and the ground $X^1\Sigma_g^+$ state are significantly offset, the emission from this state is expected to be diffuse, and has not been observed.

By contrast, low vibrational levels are populated in the Franck-Condon transitions to the $D^1\Sigma_u^+(v')$ state. The large Coulomb barrier for this state can be seen in Fig. 14. The decay of the $v = 0$ state is dominated by optical transitions to the ground state. The (0,0) and (0,1) bands emit photons that are characterized by wavelengths 1587 and 1594 Å, respectively (e.g, Ehresmann et al. 2000). Higher vibrational levels decay by predissociation. The $D^3\Pi_g$ state shown in Fig. 14 exhibits a shallow minimum which supports two vibrational levels; the lifetimes of these states against tunneling are less than 70 ps (Mullin et al. 1992).

Since the fragment ions produced in the decay of doubly ionized molecules have kinetic energies of the order of several eV, it is not easy to estimate the energies of the Auger electrons. In order to include Auger processes of molecules in atmospheric modeling, it is necessary to use data from Auger spectroscopy, calculations of potential curves and the transitions between them, and/or measurements of the energies of fragment ions produced from X-ray absorption spectroscopy. We should note here that the contribution of $1s$ ejection and Auger decay is very small for the production of doubly ionized species and energetic ion pairs for atmospherically important molecules. Just as for atomic oxygen in the atmosphere, we expect double ionization of valence electrons in molecules to be more important than Auger ionization. If the double ionization in the Franck-Condon region of a molecule proceeds via a transition to a purely repulsive state, or to the repulsive part of a "quasi-bound" potential energy curve, two energetic ionic fragments may be produced directly. The relative rates of the processes depend on the details of the potential energy curves and by the vibrational level (if any) of the doubly charged ion, as well as the energy of the impinging photon or charged particle.

2.15 X-ray Cross Sections for Atoms and Molecules

Berkowitz (2002) has summarized the photoabsorption cross sections for several atoms, and diatomic, triatomic, and polyatomic molecules for a wide range of wavelengths from threshold to the X-ray regions. Although Berkowitz does not differentiate photodissociation and photoionization cross sections, the references in this work cover a nearly complete range of photoabsorption data from threshold to very high energies to which the reader is referred. Svensson (2005) has reviewed the soft X-ray photoionization cross sections of atoms and molecules as determined with synchrotron radiation.

Henke et al. (1993; cf., 1982) have tabulated the cross sections for absorption and scattering of X-rays for the elements with atomic numbers from 1–92, for photon energies from $\sim$ 50 to 30 keV. The cross sections for core ionization of atomic species can be estimated fairly accurately by the fitting functions of Verner and Yakovlev (1995) or Verner et al. (1996). X-ray absorption cross sections of Ar, N_2, O_2, CH_4, He and H_2 have been measured by Denne (1970) in the wavelength range 23.7–82.1 Å. We discuss below the X-ray absorption cross sections of a number of atmospherically relevant species.

Atomic hydrogen has only one electron, for which the ground state is ($1s\ ^2S$), and the ionization potential is 13.598 eV (911.8 Å). There is obviously no Auger effect for H, and the cross sections in the soft X-ray region are very small. For example, at 30 Å, the H ionization cross section is about 2×10^{-22} cm^2, compared to those for C and N of 4.5×10^{-19} and 6.8×10^{-19} cm^2, respectively. At very high energies the Compton ionization (or scattering) cross sections become larger than the photoionization cross sections (e.g, Hubbell et al. 1975). In Compton ionization the photon is scattered rather than absorbed, and the photon and the ejected electron share the energy and momentum. The atomic hydrogen Compton ionization cross sections exceed the photoionization cross sections for energies greater than ~ 2.8 keV (4.4 Å) (Yan et al. 1998). The maximum Compton cross section for H falls in the energy range of 10–15 keV (0.8–1.2 Å), and has a value of about 6×10^{-25} cm^2.

The ionization potential of H_2 is 15.43 eV (~ 803 Å), and only one state of the H_2^+ ion, $X^2\Sigma_g^+$, is bound. Samson and Haddad (1994) have measured the H_2 photoionization cross sections from 18 to 113 eV (688–110 Å); Yan et al. (1998) have extended the experimental cross sections with theoretical cross sections to the soft X-ray region, from 113 eV to 300 eV (41.3 Å), and they have provided a formula for the cross sections at higher photon energies. The maximum Compton cross section for H_2 is about 1.2×10^{-24} cm^2 for incident photons with energies of about 15 keV (0.8 Å) (Hubbell et al. 1975). The H_2 Compton ionization cross sections are larger than those for photoionization at about 3.1 keV (4 Å) (e.g., Yan et al. 1998). The ratio of the Compton cross sections for H_2 to those for H are about 2.

Since there are no bound states of H_2^{++}, there is no true "threshold" for double ionization. The energy required to produce two protons with zero kinetic energy from H_2 is about 31.7 eV. Double ionization proceeds, however, via excitation from the H_2 ground state to a repulsive $H_2{}^{++}$ state for which the vertical (Franck-Condon) transition energy is about 50.5 eV. Double ionization is followed by a "Coulomb explosion", in which two protons are produced with combined energies of 14–26 eV, with a most probable energy of 18 eV (e.g., McCulloh 1968; Brehm and de Frênes 1978).

The first double photoionization cross sections of H_2 were measured by Dujardin et al. (1987) from 50 to 140 eV (88.5–248 Å). Sadeghpour and Dalgarno (1993) computed the high energy cross sections for double ionization of H_2 and showed that asymptotic ratio of the double-to-single photoionization is about 0.0225. The maximum cross section for double photoionization peaks near 64 eV, and the maximum ratio is about 0.058 near 132 eV photon energy (94 Å).

The inert gas He has two K-shell electrons in the ground electronic state ($1s^2\ ^1S$), for which the first and second ionization potentials are 24.59 and 54.4 eV, respectively. The thresholds for single and double photoionization are therefore 504.2 and 157 Å, respectively. Although He does not exhibit Auger behavior, double ionization can take place to produce an α-particle for photons with energies greater than 79 eV (157 Å). At high energies, the ratio of the cross sections for double to single ionization tend to a limiting value of 0.0164 (e.g., Dalgarno and Sadeghpour 1992). The photoionization cross sections of He at soft X-ray wavelengths are, however, small compared with those of heavier elements. For example, the cross section at 40 Å is about 1.5×10^{-20} cm^2. Photoionization cross sections of He that are accurate for X-ray wavelengths have been computed by Yan et al. (1998). Compton ionization becomes more important than photoionization at a photon energy of 6.5 keV (1.9 Å).

Because the K-shell electrons are localized around the constituent nuclei, the cross sections for K-shell ionization of most molecules can be approximated as the sum of the cross sections for the constituent atoms. For H, the core electron is also the valence electron, but X-ray photoabsorption cross sections for molecules containing H can

be estimated as the sum of the constituent atoms, if only because the cross sections for H are very small compared to other species. For example, the H photoabsorption cross section at 42.6 Å, the K-shell threshold for C, is $\sim 6.6 \times 10^{-22}\,\mathrm{cm}^2$, compared to that for C of about $10^{-18}\,\mathrm{cm}^2$. The CH_4 K-shell ionization cross sections shortward of about 200 Å are approximately equal to that of C (e.g., Denne 1970; Carter and Kelly 1976; Jannitti et al. 1990) with only a small correction for the presence of the H atoms. For $CH_4{}^{++}$ and $NH_3{}^{++}$, the hydrogen atoms are embedded in the electron clouds of the central atoms and the positive charges are located further apart, which leads to greater stability of the doubly charged ion. Similarly, for CO_2^{++}, the larger volume the positive charges occupy leads to a smaller Coulomb repulsion and longer lifetimes. In addition, the two outer electrons in ground state CO_2 are in non-bonding orbitals, so their removal does not decrease the stability of the ion, and leads to ground state lifetimes of about 4 s (Mathur 2004).

It should be noted that the inner shell binding energies for molecules may be shifted by a few eV due to chemical effects (e.g., Svensson 2005). Carbon Kα X-ray emission rates and Auger transition rates from ethane, ethylene, and acetylene have been studied by Kimura (1992), who showed that the X-ray emission rates decrease as the C–C bond order increases (or as the bond length decreases). Uda et al. (1979) showed that K-shell X-ray emission from an atom within a molecule increases as the electronegativity of the neighboring atom increases. Svensson (2005) showed that the core hole ionization energy of alkanes depends on the location of the C atom in each molecule.

2.16 Applications of the Auger Process, Double Ionization and Characteristic X-rays to Ionospheres

The effect of Auger electrons on the terrestrial ionosphere was explored by Avakyan (1978), who suggested it as the major source of O^{++}. O^{++} was detected by the mass spectrometers on the Atmosphere Explorer (AE) Satellites (e.g., Breig et al. 1977). The measurement of rate coefficients of O^{++} with atmospheric neutrals has enabled modeling of O^{++} density profiles. Rate coefficients for reaction of O^{++} with N_2, O_2, and Ar were measured by Howorka et al. (1979); with CO_2 by Johnsen and Biondi (private communication to Fox and Victor, 1980); and with H by Honvault et al. (1995). Victor and Constantinides (1979) showed that double ionization of valence electrons was more important than the Auger effect for the production of the doubly ionized species. Avakyan (1980) came to the same conclusion, but pointed out that during solar flares when the X-ray fluxes were elevated, the Auger process could be more important. Breig et al. (1982) analyzed four AE-C orbits, with the assumption that the most important source of O^{++} was double ionization of valence electrons. The measured O^{++} densities exceeded those that were modeled particularly below 200 km. Breig et al. (1982) attributed this phenomenon to a spacecraft effect, but considered other possibilities for this source, including production of O^{++} by the Auger effect, or general X-ray ionization. They concluded that there was no evidence for enhanced X-ray fluxes for these orbits, and these sources were not likely to account for the data for the orbits considered. Kudryashev and Avakyan (2000) later explored in more detail the effect of solar flares on the ionization and excitation of the terrestrial upper atmosphere, and showed that Auger electrons made a substantial contribution to the high energy electron fluxes and to increased intensities of emissions produced by electron impact on atmospheric species. Simon et al. (2005) modeled doubly charged ions in the terrestrial ionosphere. They fitted the O^{++} densities to those derived from AE-C and obtained excellent agreement with AE-C O^{++} density profiles.

Fox and Victor (1981) modeled the Venusian O^{++} profiles that were returned by the Pioneer Venus ion mass spectrometer, (e.g., Taylor et al. 1980), and showed that double valence

shell ionization of O could explain the measured densities; the Auger process was found to be a minor effect. The solar fluxes, in the X-ray region were not, however, known to a great deal of accuracy at that time. Since no measurements of the rate coefficient for the charge transfer reaction of O^{++} with O are available, the rate coefficient in all the models was varied to fit the altitude profiles of O^{++}. Values of $1.5 \times 10^{-10}\,cm^3\,s^{-1}$, $6.6 \times 10^{-11}\,cm^3\,s^{-1}$, and $1.06 \times 10^{-10}\,cm^3\,s^{-1}$, were derived by Fox and Victor (1981), Breig et al. (1982) and Simon et al. (2005), respectively. Note that the rate coefficients quoted by Gronoff et al. (2007) for these reactions are too large by a factor 10 in the text (but not in the table).

Recently, there have been several measurements of the dissociative recombination of molecular doubly charged ions in their vibrational ground states using ion storage rings. For example, Safvan et al. (1999) measured the DR coefficient for CO^{++} with electrons, and reported a value of $0.9 \times 10^{-7}\,cm^3\,s^{-1}$ at 300 K, with a quoted accuracy of a factor of 2. Seiersen et al. (2003a, 2003b) remeasured the DR coefficient for CO^{++} along with that for CO_2^{++} and N_2^{++} and obtained values of $3.0 \times 10^{-7}(300/T)^{0.5}$, $6.2 \times 10^{-7}(300/T)^{0.5}$, and $5.8 \times 10^{-7}(300/T)^{0.5}\,cm^3\,s^{-1}$, respectively.

Experimental studies of the reactions of doubly charged molecular ions with atmospheric species are sparse. The rate coefficients for reactions of O_2^{++} with O_2, N_2, CO_2, NO, and Ne were measured by Chatterjee and Johnsen (1989) using a drift-tube/mass spectrometer experiment. In this experiment the doubly charged ions were formed in vibrationally excited states by the electron impact ion source. Vibrational excitation may reduce the lifetime of a doubly charged ion if its decay process is by tunneling through a Coulomb barrier.

The products of all the reactions of O_2^{++} measured by Chatterjee and Johnsen except that with NO were observed to be simple charge transfer reactions. The dominance of charge transfer reactions that lead to charge separation of the products is a general feature of reactions of multiply ionized species with neutrals, although bond rearrangements of the products may occur (e.g., Mathur 2004). Chemical reactions of CO_2^{++} with neutrals have, however, been observed to compete with simple charge transfer reactions (e.g., Mrázek et al. 2000; Franceschi et al. 2003). In particular, dissociative charge transfer may be the most important channel for these very exothermic reactions.

Witasse et al. (2002) measured a rate coefficient for the reaction of CO_2^{++} with CO_2 and reported a value of $2.13 \times 10^{-10}\ (T/300)^{0.5}\,cm^3\,s^{-1}$. Rate coefficient for reactions of N_2^{++} with N_2 and CH_4 of 2.7×10^{-9} and $1.8 \times 10^{-9}\,cm^3\,s^{-1}$, respectively, were measured by Lilensten et al. (2005). Simon et al. (2005) reported measurements of the rate coefficients for the reaction of N_2^{++} with O_2, and obtained a value of $2.8 \times 10^{-9}\,cm^3\,s^{-1}$.

By employing these measured rate coefficients, models have been constructed of CO_2^{++} in the Martian ionosphere (Witasse et al. 2002), N_2^{++} in the Titan ionosphere (Lilensten et al. 2005), N_2^{++} and O_2^{++} in the terrestrial atmosphere (Simon et al. 2005), and CO_2^{++} and N_2^{++} in the Venusian ionosphere (Gronoff et al. 2007). With the exception of CO_2^{++} at high solar activity, the computed doubly charged molecular ion density profiles exhibited maxima that were of the order of or less than of than $1\ cm^{-3}$. In addition, because the doubly charged ions are not necessarily formed in the long-lived states, and many potentially important reactions were neglected, the computed density profiles are probably upper limits.

Winningham et al. (1989) used data from the low altitude plasma instrument on the Dynamics Explorer Spacecraft and found a population of high energy photoelectrons, which were shown by models to be produced by solar soft X-rays; the peaks in the electron spectrum were ascribed to Auger electrons emitted from oxygen and nitrogen. Siskind et al. (1989) included the Auger effect for the first time in their models of thermospheric NO densities. Along with several other changes to their model, they found that the new computed NO profiles better fit the more recent data.

Recently, Mitchell et al. (2000) have interpreted a feature in the Martian electron fluxes at ~ 500 eV measured by the Electron Reflectometer on board the MGS spacecraft as oxygen Auger electrons. Cravens et al. (2004) modeled the photoelectron flux at an altitude of 1220 km on Titan, and predicted peaks near the 284 and 402 eV arising from the C and N K-shell Auger electrons.

X-rays have been detected from many solar system objects, including Venus, Earth, Mars, Jupiter, Saturn, the moon, Io, Europa, Ganymede, comets, the Io plasma torus, the rings of Saturn, and the coronas of Earth and Mars. This subject has been recently reviewed (Bhardwaj et al. 2007a). For example, the X-ray spectrum from Venus was observed with the Chandra X-ray observatory, and discrete emissions were seen from the unresolved O-$K\alpha$ emission lines near 530 eV, from the C-$K\alpha$ lines near 280 eV, with a marginal detection of the N-$K\alpha$ lines near 400 eV (Dennerl et al. 2002). A similar spectrum of Mars exhibited only O-$K\alpha$ lines (Dennerl 2002) Additional emission was attributed to scattering of solar X-rays and bremmstralhung emission, and charge exchange between highly stripped heavy ions in the solar wind and H and O atoms in the coronas.

Bhardwaj et al. (2005a) have reported the discovery of oxygen Kα X-rays at 530 eV from the rings of Saturn with the Chandra X-ray Observatory. The rings are known to be made up of mostly water ice. They also proposed that fluorescent scattering of solar X-rays from the icy H_2O ring material plays a role.

Maurellis et al. (2000) modeled the X-ray emission spectrum from Jupiter and predicted that the C-$K\alpha$ lines contributed 8–12% of the spectrum. Bhardwaj et al. (2005b) found that Jovian low-latitude X-ray emissions varied as the solar X-ray flux, and suggested that resonance scattering of solar radiation dominated, with a 10% contribution from characteristic X-rays. They argued against the theory of Waite et al. (1997) that the X-rays were produced by precipitation of ring current particles.

On the other hand, the X-ray emission from comets is proposed to arise mainly from charge-exchange of highly stripped solar wind ions with cometary neutrals (e.g., Cravens 2002). A similar mechanism may be responsible for X-rays from the Jovian auroral regions. For example, Kharchenko et al. (2006) modeled the precipitation of O^+ and S^+ ions with energies of 1–2 MeV/amu and found that stripping produced very high charge state O^{q+} and S^{q+} ions, which emit X-rays when they charge exchange with neutral species, such as H, He and H_2, in the Jovian auroral regions.

When characteristic X-rays are detected from the atmospheres of the solar system objects, the dominance of Auger electron ejection over that of these X-rays for small atoms dictates that there must be many more Auger electrons produced. When these electrons are ejected from molecules, it is likely that ion fragments are produced with substantial kinetic energy. The production of energetic ion fragments from the molecular Auger effect could play a role in heating in the lower ionospheres of the planets, especially during solar flares. This effect and others due to Auger processes, and the emission of characteristic X-rays on various planetary bodies remain to be modeled. In any case, the primary uncertainty in modeling the effects of X-rays on planetary atmospheres is determining the solar fluxes in this region of the spectrum, which are not well known and are quite variable.

3 Auroral Particle Deposition

3.1 Introduction

Auroral particles are energetic, extra-atmospheric particles, which arise from the magnetized environment of a planet or satellite and precipitate into the upper atmosphere, where

they deposit their energy. The particles can be electrons, light ions, such as protons, or heavy ions, such as O^+ or S^+. Precipitating ions may charge transfer to atmospheric species to produce energetic neutrals. For magnetized planets, where magnetospheric acceleration processes are effective, the auroral particles have energies ranging from a few hundred eV to a few hundred keV for electrons, and from a few keV up to a few MeV/amu for heavy ions (Kharchenko et al. 2006). Auroral heavy particles at Jupiter mainly originate from the moon Io. At Earth, auroral electrons and heavier particles come originally from the ionosphere, as shown by the presence of oxygen ions in the magnetospheric plasma. There is also a contribution from the solar wind, especially in the cusp regions, where the particles can enter the atmosphere directly. At Venus and Mars, which have induced magnetospheres, the auroral particles originate from the shocked solar wind population and from the planetary atmosphere. The energization processes are weaker at these planets than at magnetized planets. The auroral particles at Venus and Mars are therefore softer than at Earth, Jupiter, and Saturn, with energies ranging from a few tens of eV to a few hundred eV.

Particle precipitation represents a significant source of energy for the auroral regions of magnetized planets and on the nightsides of non-magnetized planets. The total energy input from auroral particles and Joule heating is also often comparable to or exceeds that due to solar photons (e.g., Strobel 2002). Auroral particles deposit their energy in a planetary atmosphere through impacts with the atmospheric neutrals via ionization, excitation, dissociation, and elastic scattering. In addition, suprathermal electrons heat the ambient electrons via Coulomb collisions. All these processes cause the upper atmosphere to respond through changes in its electrodynamical and dynamical processes, thermal structure and constituent distributions. The focus in this section is on one aspect of auroral particle deposition, namely, the auroral emissions. First, the rationale for analyzing auroral emissions is discussed, followed by a short description of the modeling of transport and energy deposition of auroral particles. Then different approaches for the spectroscopic analysis of auroral emissions which are used for identifying and retrieving the spectral characteristics of auroral particles are presented. Finally, some concluding remarks on the spectroscopic analyses are given. The specific examples of aurorae given here are taken from the X-ray, FUV, and visible spectral regions. Discussion of infrared aurora as well as complementary information on the X-ray aurora can be found in Slanger et al. (2008).

3.2 Relevance of Auroral Emission Analysis

The term "aurora" refers to the observed emission spectra (from γ-rays and X-rays to ultraviolet, visible and infrared) arising from the interaction of these extra-atmospheric, energetic particles with an atmosphere (Galand and Chakrabarti 2002). Auroral emissions are associated with an excited state of an atmospheric species that is either (1) the result of a direct impact of an auroral particle with an atmospheric species (e.g., the N_2 Lyman-Birge-Hopfield (LBH) bands) or (2) the result of a chain of chemical processes initially originated with the impact of an auroral particle with an atmospheric gas. Auroral emissions may also be produced by the energetic particles themselves, as is the case of the Doppler-shifted H emissions produced in an energetic H^+/H beam, the K-shell lines produced by charge transfer from highly stripped heavy ions to atmospheric gases, or Bremsstrahlung continuum radiation produced by very energetic electrons.

While the auroral emissions were first observed from the ground in the high latitude regions of Earth, the capability to image aurorae from space opened a new era. The entire terrestrial auroral oval has been imaged from several Earth radii by orbiting spacecraft, including Dynamics Explorer 1 (DE1), Polar, and IMAGE, in the far ultraviolet (FUV),

visible, and X-ray spectral regions. This approach is the only way to obtain snapshots of the particle input over entire auroral regions and permits inference of the time variability of the total hemispheric auroral particle power (e.g., Lummerzheim et al. 1997; Germany et al. 1997; Frey et al. 2002; Østgaard et al. 2000, 2001; Liou et al. 2001). *In situ* particle measurements acquired over many years have been used to derive statistical patterns of the particle energy input (e.g., Fuller-Rowell and Evans 1987; Hardy et al. 1989; Brautigam et al. 1991). While such an approach is of significant relevance for morphological trend studies, it is not appropriate for studies of a particular day or geomagnetic event (e.g., Østgaard et al. 2000). Spectroscopic analyses of global auroral images have been used for a wide range of purposes, such as assessing the atmospheric response to particle precipitation (Rees et al. 1995; Doe et al. 1997; Aksnes et al. 2004, 2006; Sætre et al. 2007), estimating the overall budget during a magnetic cloud event (Lu et al. 1998), inferring the ionospheric contribution to magnetosphere-ionosphere coupling (Liou et al. 1997; Meng et al. 2001), and inferring the magnetospheric source regions of auroral precipitation during substorms (Lu et al. 2000).

In addition to the observations of auroral emissions produced in the terrestrial atmosphere, access to space has allowed the discovery and analysis of aurorae throughout the solar system. This has been made possible due to observations from flyby spacecraft (e.g., Voyager, Rosetta, New Horizons); from orbiting planetary probes, such as Galileo (Jupiter), Cassini (Saturn), Pioneer Venus, Venus Express and Mars Express; and from Earth-orbiting observatories, such as the International Ultraviolet Explorer (IUE), the Hubble Space Telescope (HST), Chandra, and XMM-Newton. Discovering and analyzing auroral emissions have led us to a greater understanding of the physical processes taking place in the upper atmospheres and magnetospheres of different solar system bodies. Investigations of aurorae have been used to determine magnetic field configuration, to trace plasma interactions, and to identify atmospheric constituents and auroral particle sources. Reviews of the modeling, observations, and analysis of auroral emissions can be found in Galand and Chakrabarti (2002) for bodies throughout the solar system, Bhardwaj and Gladstone (2000) and Waite and Lummerzheim (2002) for the outer planets and Earth and Bhardwaj et al. (2007a) for X-rays.

3.3 Modeling of Auroral Energy Deposition

Unlike solar photons which are absorbed in the atmosphere, auroral particles are scattered (and heavy ions can also charge exchange) and lose their energy in finite steps along their path through the atmosphere. As a consequence, describing the transport and energy deposition of auroral particles is more complicated than for solar photons. In addition, the contribution of secondary, tertiary (and so on) electrons produced through ionization of atmospheric species by particle-impact must be included in the calculation, as they play an important role as a further source of ionization, excitation or heating. Unlike the thermal ionospheric particles which can be described by macroscopic quantities, suprathermal, auroral particles, similar to photoelectrons, need to be treated through a kinetic approach. Their energy distribution changes as they propagate through the atmosphere. A comprehensive description of the modeling of auroral particle transport and induced emission brightnesses is presented by Galand and Chakrabarti (2002) and hence in the following is only briefly outlined.

Different approaches have been used to describe the transport and energy deposition of auroral electrons. One approach is based on the continuous slowing down approximation (e.g., Rees 1963; Fox and Stewart 1991; Régo et al. 1999; Ågren et al. 2007). This method is restricted to the estimation of ionization and excitation rates. In addition to these

quantities, the following three methods provide suprathermal electron intensities and thermal electron heating rates. The first two methods are based on the analytical or numerical solution of the Boltzmann equation. First, the two-stream approximation describes the upward and downward fluxes of electrons propagating along a magnetic field line, as discussed, for example by Gan et al. (1992), Grodent et al. (2001), and Cravens et al. (2005). All of the latter studies are based on the approach developed by Nagy and Banks (1970). Second, the multi-stream approach describes the particle fluxes for a large number of pitch angles—typically 8 or 16—(e.g., Strickland et al. 1976; Lummerzheim et al. 1989; Perry et al. 1999; Galand et al. 1999; Leblanc et al. 2006). While the former method is suitable for estimating integrated quantities, such as excitation and heating rates, the latter method is required for comparison with observed particle fluxes or for studying anisotropy. The final type of calculation is the Monte Carlo approach, which is a stochastic method based on the tracking of numerous individual particles (e.g., Onda et al. 1999; Solomon 1993).

Calculations of the transport and energy deposition of auroral ions are even more complex than those of auroral electrons due to the production of neutrals and ions of different charge states through charge-changing reactions. Each charge-state population needs to be described individually while their distributions are coupled through the charge-changing reactions (e.g., Cravens et al. 1995; Galand et al. 1997; Kallio et al. 1997; Basu et al. 2001; Kallio and Barabash 2001; Kharchenko et al. 2006). In addition, when energetic neutral atoms are produced, the particle beam spreads over space, reducing the energy deposition at the center of the beam (e.g., Lorentzen 2000; Fang et al. 2005).

The heating efficiency is defined as the local rate at which the gas (e.g, electrons or neutrals) is heated divided by the total local energy deposition rate. Such heating efficiencies have been calculated using all the above mentioned approaches except the first. The neutral heating efficiency is sensitive to the composition, density and temperature of the neutral atmosphere, but this dependency can be minimized by adopting a pressure coordinate system instead of an altitude-based coordinate system (Rees et al. 1983). The vertical profile of the heating efficiency was found to be independent of the auroral electron spectrum (Rees et al. 1983), but dependent on the auroral proton spectrum (Srivastava and Singh 1988).

Transport and energy deposition models are used to estimate the excitation rate associated with auroral emissions. If the excited state has no sources other than auroral particle impact, and its radiative lifetime is very short compared with those of other loss processes, the auroral emission brightness can be easily estimated. The calculation of the emission brightness requires the inclusion of photoabsorption, when the emission undergoes "true" absorption by atmospheric species, as is the case for the emissions commonly used for auroral diagnostics, such as the N_2 Lyman-Birge-Hopfield and the H_2 Werner and Lyman bands. For excited states which have long lifetimes against radiation, the continuity equation for the excited state must be solved in order to estimate the emission brightness (Lummerzheim et al. 2001). Finally, radiative transfer calculations are required when the emitted photons undergo scattering, such as resonance scattering, through their paths in the atmosphere. This is the case for modeling the OI 1304 Å resonant triplet in the Earth's auroral regions (Gladstone 1992) and the H Lyman α spectral profile at the giant planets (Régo et al. 1999).

3.4 Spectroscopic Analysis of Auroral Emissions

Spectroscopic analysis of auroral emissions using comprehensive modeling tools, such as particle kinetic codes, can aide in identifying the type (e.g., electrons, light or heavy ions) of the precipitating particles, as well as in determining their mean energy, spectral shape, and

total energy flux. Two approaches that have been widely used include the determination of color ratios, and spectral line profiles. Here, rather than providing an exhaustive review of the subject, a few examples are presented for illustration.

3.5 Color Ratios

A "color ratio" is a ratio of total brightness in two wavelength regions, each of which includes one or more strong auroral emissions. Variants of this definition are based on ratios which are a function of the total brightnesses in two (or more) wavelength regions (Régo et al. 1999). The choice of the wavelength regions is determined by the dependence of the color ratio on the altitude of maximum emission. If one assumes an atmospheric model, i.e., altitude profiles of neutral densities, the ratio can be related to the energy of the incident auroral particles. More energetic particles deposit their energy deeper in the atmosphere, and this is manifested by a lower altitude of maximum emission. Once the mean energy of the incident particles is inferred, the total energy flux can be retrieved from the brightness in one of the spectral windows. Such an approach may be used after removal of any non-auroral contributions, such as scattered sunlight and airglow. The solar contribution has been successfully removed from FUV images by, for example, Liou et al. (1997) and Lummerzheim et al. (1997). Since visible radiation is scattered more effectively than UV radiation, high resolution auroral spectroscopy from the ground under sunlit conditions has only recently begun (e.g., Pallamraju and Chakrabarti 2006 and references therein). In addition FUV auroral emissions are prompt and originate from direct energetic particle impact compared with the visible emissions that can arise from chemical reactions of the particles that are produced. Therefore their theoretical interpretation, when multiple scattering can be neglected, is easier.

There are different ways to interpret the color ratio as an indicator of the particle energy. The "colors" associated with emissions may be produced by different mechanisms or by interaction of the particles with different neutral species whose relative density varies with altitude. Examples include the following ratios widely-used for the analysis of the terrestrial aurora: N_2 LBH/OI (1356 Å), where the wavelength range of the LBH bands is 1273–2555 Å (Frey et al. 2002), OI(6300 Å)/N_2^+ 1NG (4278 Å) (also called red-to-blue ratio) (Strickland et al. 1989; Waite and Lummerzheim 2002), OI(8446 Å)/OI(7774 Å) (Waite and Lummerzheim 2002). The analysis of the OI(1304 Å)/OI(1356 Å) intensity ratio derived from Pioneer Venus observations has provided evidence for precipitation of very soft electrons into the nightside atmosphere of Venus (Fox and Stewart 1991). At Mars, the brightness ratio of the nightside CO Cameron band emission and CO_2^+ ultraviolet doublet emission has been derived from Mars Express observations. Based on the analysis of these emissions, Leblanc et al. (2006) inferred that they are consistent with precipitation of electrons characterized by a few tens of eV, that is, of lower energies but with larger fluxes than those of the typical "auroral" electron spectra. This conclusion indicates that the emissions observed may not be auroral in origin, but rather may be induced by photoelectrons produced in a sunlit region that is magnetically connected to the region where emissions were observed.

One of the limitations of using these color ratios is their sensitivity to the ratio of the column densities of the atmospheric constituents involved. This is particularly the case for color ratios based on atomic oxygen and molecular nitrogen emissions, since the [O]/[N_2] ratio is very sensitive to magnetospheric activity and is difficult to estimate (e.g., Strickland et al. 1999; Drob et al. 1999; Meier et al. 2005). As a result, the use of more than two "colors" is required for providing additional constraints on the atmospheric composition

Table 2 Auroral spectroscopic analysis based on the use of FUV color ratios assuming pure electron precipitation in the auroral regions of Earth and Jupiter

Planet:	Earth[a]	Jupiter[b]
Auroral emission band system:	N_2 LBH	H_2 Lyman and Werner
Centered λ of selected bands[c]:	∼ 150 nm & ∼ 170 nm	∼ 125 nm & ∼ 160 nm
Absorber:	O_2	CH_4
Strong photo-absorption below:	∼ 160 nm	∼ 140 nm
Electron energy range retrieved by this technique:	∼ 0.2−20 keV	∼ 10−200 keV
Type of electron aurora identified:	Discrete aurora[d]	Diffuse and discrete aurora[e]

[a]Lummerzheim et al. (1997), Germany et al. (1997)

[b]Régo et al. (1999) and references therein

[c]The wavelength bands selected for the analysis are about 10 nm or less wide (FWHM)

[d]Primarily discrete aurora (Liou et al. 1997), with contribution of diffuse aurora, especially at storm-time (Chen et al. 2005)

[e]Hard electron component only (Grodent et al. 2001; Ajello et al. 2001, 2005)

with four key channels recently proposed by Hecht et al. (2006) for ground-based auroral analysis at Earth.

Another type of color ratio is based on the use of a band system that is attenuated strongly in one part of the spectrum and significantly less in the other. The relative shape of the spectrum of this system, and thus the associated color ratio, can be used as an indicator of the total column density of the absorber above the auroral emitting layer; if an atmospheric model is assumed, the ratio can be related to the energy of the incident auroral particles. Such an approach, which is used at Earth is based on observations of the FUV N_2 LBH band system, for which the shortward spectral component is strongly absorbed by O_2 in the Schumann-Runge continuum (e.g., Germany et al. 1997; Lummerzheim et al. 1997). The energy flux of the incident particles is inferred from the total brightness in the longward spectral window, which is not strongly dependent on the energy of the incident particles (e.g., Liou et al. 1998 and references therein). At the outer planets, FUV H_2 Lyman and Werner band emissions are used in a similar manner with the hydrocarbon layer (primarily methane) as the wavelength-dependent absorber (Régo et al. 1999, and references therein; Grodent et al. 2001; Gérard et al. 2004; Ajello et al. 2005 and references therein). In that case, the color ratio provides the altitude of the auroral emitting layer relative to the methane homopause. A comparison of the technique used at Earth and Jupiter is summarized in Table 2 and color ratios as a function of the mean energy of the incident auroral particles are presented in Fig. 15. The strong dependence of the color ratios on electron mean energy shows clear evidence of the relevance of such ratios for auroral electron diagnostics.

Analysis of auroral N_2 LBH observations allows the retrieval of the spectral characteristics of electrons ranging from a few 100's of eV to less than 20 keV. For electrons of energies below ∼0.2 keV, the altitude of maximum emission is high enough that there is no significant O_2 absorption over the whole N_2 LBH spectrum; the color ratio becomes independent of the energy of the incident electrons. For electrons with energies greater than 15–20 keV, the altitude of maximum emission is low enough that O_2 absorbs significantly over the whole N_2 LBH spectrum. Not only does the color ratio becomes insensitive to the energy of the

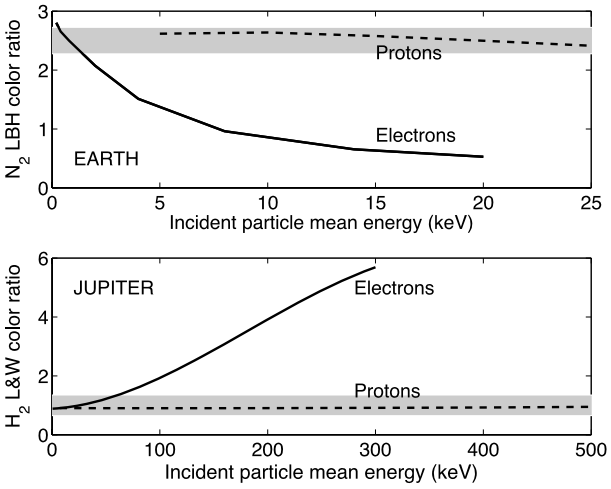

Fig. 15 Modeled FUV color ratios plotted as a function of the mean energy of the incident, auroral particles. Since they are strongly dependent on the energy of the incident electrons, they are used to infer the electron energy from FUV images. The *shaded area* highlights the similar values in color ratios between protons and low energy electrons. (*Top*) Color ratio associated with the N_2 LBH bands for Polar/UVI imaging the terrestrial auroral regions (after Galand and Lummerzheim 2004). (*Bottom*) Color ratio associated with the H_2 Lyman and Werner bands observed by IUE and HST in the auroral regions of Jupiter (after Régo et al. 1999)

incident electrons, but the energy flux cannot be derived from the total brightness of the less attenuated color. At the outer planets where the absorber is the hydrocarbon layer, the technique can be used for inferring the mean energy and energy flux of $\sim$ 10–200 keV electrons. The lower energy boundary is determined by the energy required to reach the hydrocarbon layers. At Jupiter, the FUV H_2 color ratio has been used to retrieve the hard component of the electron precipitation ($\sim$10 keV to $\sim$100–200 keV) (e.g., Morrissey et al. 1997; Grodent et al. 2001; Ajello et al. 2001; Pallier and Prangé 2004; Gustin et al. 2004; Ajello et al. 2005; Gladstone et al. 2007). Another technique is required to retrieve the soft component, such as the analysis of EUV observations (e.g., Ajello et al. 2001, 2005). At Saturn, typical auroral electrons are expected to range from a few keV to a few tens of keV. Even though the FUV H_2 color ratio, based on Jovian calculations, has been used (Gérard et al. 2004), an alternative approach, such as the analysis of the EUV emissions or the H Lyman α profile, seems more suitable for Saturn.

At Earth and Jupiter, electron aurorae may be "diffuse" or "discrete". These are the two major types of electron aurora that are identified in or close to the main auroral oval. The diffuse aurora is unstructured, at least on large spatial scales, and is located at the equatorward edge of the main oval. At Jupiter, the associated electron precipitation is induced by pitch angle scattering as a result of the interactions of a warm plasma from the inner plasma sheet with the cold plasma escaping from Io and diffusing outward. At Earth, except during storm-time conditions (Chen et al. 2005), diffuse aurora are characterized by precipitating electron energies of a few tens of keV and energy fluxes less than 1 mW m^{-2}. At Jupiter, the hard component of the diffuse aurora is associated with precipitation of electrons characterized by energies of the order of a few tens of keV. Discrete aurorae, which are brighter than diffuse aurorae, are associated with upward field-aligned currents (i.e., field-aligned precipitating electrons), which are characterized by energies of 1–10 keV at Earth and 30–100 keV at Jupiter. At Earth, discrete aurorae are very dynamic over time scales ranging from fractions of a second to hours, and are highly structured over horizontal scales smaller than a kilometer. It should also be noted that a soft electron component is often added to the electron distribution in both the diffuse and discrete aurorae in order to meet the temperature constraints (Grodent et al. 2001) or EUV observations of Jovian aurorae (e.g., Ajello et al. 2001, 2005).

There is one interesting consequence of the limited range of electron mean energies which can be recovered by the color ratio from the approaches presented in Table 1. At Earth, the approach based on N_2 LBH ratio is primarily useful for the analysis of discrete electron aurora (Liou et al. 1997). Diffuse terrestrial aurorae are primarily induced by electrons that are too hard to be diagnosed by this technique, and are not intense enough to be detected by the UV imagers from high Earth orbit (e.g., Polar), except during storm-time conditions (Chen et al. 2005). At Jupiter this technique can, however, be used to retrieve the characteristics of the harder components of both discrete and diffuse aurorae (Régo et al. 1999). Therefore, while similar techniques can be used for quantitative diagnostics of the electron aurora at different solar system bodies, different limitations apply to the derived physical quantities and to the type of aurora which can be analyzed.

When the emissions in the two colors originate from the same process and the same molecule, uncertainties in the identity of the atmospheric absorber(s) are limiting factors in the analyses, especially at Jupiter where the location of the hydrocarbon layer is variable. Pallier and Prangé (2004) used the H_2-FUV color ratio technique to analyze an atypically bright auroral region observed with HST/STIS. They identified this region as a transient bright cusp. The color ratio obtained implies that the electrons are characterized by energies as large as 200 keV, or that the hydrocarbon layer has been significantly uplifted by the power input.

Spectroscopic analyses based on the use of color ratios are commonly undertaken by assuming pure electron precipitation. Auroral particles of different types, however, such as protons and heavy ions (Régo et al. 1999, and references therein; Galand et al. 2002; Galand and Lummerzheim 2004), may also contribute to the FUV emissions. Under these conditions the color ratios may be misinterpreted. At Earth, the contribution of proton precipitation to the total energy flux averaged over the entire auroral oval is about 15% that of electrons (Hardy et al. 1989). In addition, at given locations and times, particularly in the cusp and at the equatorward boundary of the evening sector of the auroral oval, proton precipitation can become the dominant energy source for the upper atmosphere. Galand and Lummerzheim (2004) have shown that the presence of proton precipitation with an energy flux even as modest as 10% of the total can yield an underestimate of the electron mean energy and energy flux, especially in regions of hard electron precipitation. The color ratio produced by a proton aurora has values similar to that induced by soft electrons (Fig. 15a). In addition, auroral keV protons are more efficient at ionization than are soft electrons (Galand et al. 1999, 2001). The differences between proton and electron aurora can lead to misinterpretation when brightness ratios are used to derive ionospheric conductances, if pure electron precipitation is assumed. It is crucial to separate the electron and proton components of the precipitation in order to improve the auroral diagnostics (Galand et al. 2002).

Figure 15a shows that unlike electron aurorae, the color ratio for proton aurorae is weakly dependent on the mean energy of the incident particles. The decrease in brightness of the emission induced by proton/H atom impact with increasing energy of the incident protons is compensated by the increase of the secondary electron contribution. Molecular oxygen absorption is a rather secondary effect in proton aurora (Galand and Lummerzheim 2004).

Similar to the terrestrial case, auroral protons at Jupiter give the same results as soft electrons for commonly-used color ratios (Fig. 15b). The limitation of the color ratio analysis based on the assumption of pure electron precipitation is however difficult to estimate at Jupiter. To date the relative importance of proton precipitation in terms of incident energy flux is still unknown, even though it is not dominant (Régo et al. 2001). As for heavy ions, constraints on the spectral characteristics derived from the analysis of X-ray spectra could be used to estimate the induced FUV brightness.

Table 3 Analysis of auroral spectral profiles at Earth and Jupiter

H spectral profile	Planet	Earth	Jupiter
	Emission line	H Balmer	H Lyman α
	Emission characteristics (dominant process)	Doppler-shifted as emitted by energetic H atoms[a]	Produced by auroral particles with a central reversal due to H absorption[b]
	Type of auroral particles characterized	Protons	Electrons[c]
X-ray spectral profile[d]	Spectral range	(1) $\geq$ 3 keV (2) 0.1–2 keV	(1) $>$ 2 keV (2) $<$ 1 keV
	Emission characteristics	(1) Bremstrahlung emission by electrons (2) K-shell lines emitted by the atmospheric species excited by energetic electrons	(1) Bremstrahlung emission by electrons (2) K-shell lines emitted by the precipitating heavy ions
	Type of auroral particles characterized	Electrons (>3 keV) (including diffuse aurora)	(1) Electrons (2) Heavy ions (S+, O+)

[a]Galand and Chakrabarti (2006) and references therein

[b]Prangé et al. (1997), Régo et al. (1999), Régo et al. (2001)

[c]Assuming the electrons are the dominant particle source

[d]Bhardwaj et al. (2007a) and references therein

3.6 Spectral Profiles

Another approach for identifying the type of precipitating particles and for retrieving their spectral characteristics is based on the analysis of spectral profiles resulting from the interaction of the auroral particles with the atmosphere. Depending on the atmospheric composition, the type of auroral particles, and the wavelength range, the spectral profiles are either emitted by the atmospheric species or by the auroral particles. The shape of these auroral profiles may be used to determine the spectral shape or the mean energy of the impinging particles, and their total brightness may be used to infer the total energy flux input. We have chosen to focus on two types of spectral profiles: that associated with the emission of hydrogen atoms, either atmospheric or precipitating, and that associated with X-ray emissions. The dominant production mechanism and relevant physical parameters retrieved from the analysis of such profiles observed in the auroral regions at Earth and at Jupiter are summarized in Table 3.

3.7 H spectral profiles

At Earth, the H Lyman and Balmer series emissions are unique signatures of proton precipitation (e.g., Eather 1967). The high spectral resolution required for a comprehensive analysis of the H emission profiles, however, has been achieved in the visible region of the spectrum from ground-based observations (Galand and Chakrabarti 2006, and references

therein), but not yet from space (Galand and Lummerzheim 2004). While multi-spectral analysis of space-based observations has been performed for retrieving both electron and proton components of the precipitation, assumptions about the energies of the incident protons had to be made due to the low resolution of the H profiles (Strickland et al. 2001; Galand et al. 2002). IMAGE/SI12 has returned the first global images of the proton aurora over the entire oval. These images have provided crucial information about the morphology and dynamics of such aurorae and have considerably improved our understanding of them (e.g., Frey 2007, and references therein). The SI12 channel is aimed at the Doppler-shifted portion of the H Lyman α line profile induced by protons and hydrogen atoms with energies larger than 1 keV. It effectively excludes geocoronal Lyman α. Only the integrated brightness over the profiles is, however, provided, which includes the contamination by the nearby NI 1200 Å emission. No information on the spectral shape of the H line is available, which limits quantitative analyses (Frey et al. 2002; Immel et al. 2002). It is surprising that no high resolution spectral imaging has been done of the H Lyman alpha in the terrestrial atmosphere, despite the fact that such imaging has been carried out at other planetary bodies, such as Jupiter.

At Jupiter, the shape and brightness of the H Lyman α profile could be analyzed to derive the mean energy and energy flux of the incident precipitating particles (Régo et al. 1999). The "cold" or atmospheric component of the hydrogen profile is the result of the dissociative excitation of atmospheric H_2 by the auroral particles:

$$H_2 + (e, p, H) \rightarrow H(1s) + H(2p) + (e, p, H). \tag{32}$$

$$H(2p) \rightarrow H(1s) + h\nu \ (1216\text{Å}). \tag{33}$$

Absorption of the photons emitted by the hydrogen atoms is followed by re-emission in the wings of the profile. The depth and width of the central self reversal as seen on HST observations have been associated with the H column density above the emission region (Prangé et al. 1997). If an atmospheric model is assumed, the energy of the incident particles can be retrieved. These H Lyman α profiles do not depend upon the identity of the particles (electrons versus protons) for a given penetration depth; they only constrain the atmospheric H column density above the emitting layer (Régo et al. 1999). Similar to the terrestrial case, the presence of proton precipitation in the Jovian auroral regions is indicated by the presence of a strong Doppler-shifted (or "hot") component in the H profile (Régo et al. 1999). The absence of a clear detection of this component in the HST observations rules out auroral protons as a major component of the precipitating flux at Jupiter (Régo et al. 2001). The limitations of this technique lies in the uncertainties in the atmospheric density profiles of atomic and molecular hydrogen as well as the possible extinction by methane, which would uniformly affect the profile. A multi-spectral approach in which an FUV color ratio technique is combined with an H profile analysis would aid in better constraining the problem by reducing the number of uncertainties (Régo et al. 2001).

3.8 X-ray Spectral Profiles

In the hard X-ray region, which we define here as photons with energies greater than 2 keV, the auroral emission is produced by the energetic electrons themselves through continuum Bremsstrahlung radiation. This phenomenon has been extensively observed at Earth for deriving the spectral characteristics of hard electron precipitation. For more than a decade, global 2D imaging has been possible from the PIXIE instrument onboard the Polar satellite, which is sensitive to X-rays in the 2–60 keV range. Such images have allowed the retrieval of the characteristics of the energetic electrons and their morphology and variability

in time (e.g., Østgaard et al. 2000). Although its presence at Jupiter had been predicted, the Bremsstrahlung component in the aurorae has only recently been identified from analysis of XMM-Newton observations by Branduardi-Raymont et al. (2007).

In the soft X-ray region ($E \leq 2$ keV), the Jovian aurora has been extensively observed since the 1980s, while there have been few observations of X-rays in the terrestrial aurora. At Earth, the first imaging of the auroral region in the soft X-ray region was undertaken by Bhardwaj et al. (2007b). The analysis of the terrestrial spectra has provided evidence of Kα lines for nitrogen and oxygen near 0.4–0.5 keV overlying the Bremsstrahlung emission spectrum. $K\alpha$ X-rays are initiated by core-ionization of atmospheric species by X-rays or energetic particles, followed by the filling of the core hole by a valence electron. The excess energy must be carried away by a characteristic X-ray or an Auger electron. Another possible source of soft X-rays is the interaction of solar wind heavy ions with the terrestrial upper atmosphere in the cusp regions (Bhardwaj et al. 2007b). At Jupiter, high spectral resolution observations have clearly identified the presence of X-ray lines in the spectrum which are consistent with charge exchange by precipitating highly stripped oxygen and possibly sulfur ions (Elsner et al. 2005; Kharchenko et al. 2006).

3.9 Concluding Remarks on the Comparative Spectroscopic Analysis of Auroral Emissions

Spectroscopic analysis of auroral emissions allows a quantitative diagnostic of the precipitating particles. When applied to a sequence of auroral images, it provides information about the morphology and variability in time of the source(s) of the particles. For example, the analysis may provide information about the role of the solar wind in producing the emissions (e.g., Liou et al. 1998; Fillingim et al. 2005; Pallier and Prangé 2004; Frey 2007).

Such analyses, however, have limitations, which should be kept in mind. While similar techniques can be applied at different solar system bodies, the energy range covered by the analysis, the type of aurora which can be probed, or the physical quantities derived from the analysis vary from one body to another (see Tables 1 and 2). Among the limitations are the physical parameters required for spectroscopic analyses, including particle-impact cross sections (cf., Huestis et al. 2008), atmospheric neutral densities (cf., Müller-Wodarg et al. 2008), and pitch angle and energy distributions of the incident, auroral particles. For instance, recent updates in the electron impact cross sections of the N_2 LBH excitation (Johnson et al. 2005) potentially have implications for auroral FUV analyses at Earth and other bodies with nitrogen-dominated atmosphere, such as Titan. In addition, large uncertainties lie in determining the [O]/[N_2] ratio at Earth and the hydrocarbon layer and H column density at Jupiter, which are all very variable in the auroral regions.

One method of addressing these limitations is to employ a multi-spectral approach, which includes the use of more than one color ratio, or combinations of different spectral regions (e.g., EUV, FUV, soft/hard X-rays, IR). Combining the analysis of auroral emissions from different origins provides complementary information to further constrain the auroral diagnostic. Such an approach has been used: (1) to assess characteristics of different particle types. At Jupiter, the regions of bright FUV auroral emissions and hard X-ray spectra have been found to be coincident and consistent in brightness with predicted emissions from a population of energetic electrons, while soft X-ray spectra from heavy precipitating ions are located at the periphery (Branduardi-Raymont et al. 2008). (2) to cover a spectral range for the auroral particles that is larger than that covered with only one technique. The analyses of FUV color ratios and hard X-ray profiles have been combined to derive spectral characteristics of the auroral electrons from a few 100's of eV to a few 100's of keV (e.g., Østgaard

et al. 2001). Such an approach is critical for a better understanding of the energy budget and of the response of the atmosphere to particle precipitation (Aksnes et al. 2004, 2006; Sætre et al. 2007). (3) to constrain the atmospheric model used for the analysis (Hecht et al. 2006; Régo et al. 2001).

A cross body comparison, illustrated here through a comparison between Earth and Jupiter, yields a synthetic, and thus more critical view of auroral analysis and ultimately of interactions taking place at different solar system bodies, including solar wind-magnetosphere-ionosphere coupling. Such an approach is extremely relevant to planetary aeronomy (Galand et al. 2006). The optimum cross body comparison is based on multi-spectral observations of two or more solar system bodies responding to similar forcing. Prangé et al. (2004) have given a preview of such an analysis by the comparison of the global auroral response of Earth, Jupiter, and Saturn to an interplanetary shock triggered by a violent solar eruption. Another example, even though not auroral, is the observation of the response of the terrestrial and martian ionospheres to the same solar flares (Mendillo et al. 2006; Mendillo and Withers 2008).

4 Energy Deposition of Pick-up Ions

Heating and loss of the atmosphere due to plasma bombardment occur at Mars, Venus, Pluto and Titan (when it is outside of Saturn's magnetopause), due to impacting solar wind ions and pick-up ions. Such processes also occur at Titan, Triton, Io, and Europa due to impacting magnetospheric plasma and pick-up ions. Atmospheric heating also occurs at Earth, primarily due to magnetospheric O^+ ions that are formed in the corona and re-impact the thermosphere as described below. The incident plasma ions typically have energies of the order of 10's of eV to tens of keV and lose their energy in a very small column of atmosphere of the order of 10^{15} to 10^{17} atoms cm^{-2}. Therefore, even a relatively small energy flux that is deposited close to the nominal exobase ($\sim 10^{15}$ atoms cm^{-2}) (cf. Johnson et al. 2008) can cause heating and escape, processes often lumped together as "atmospheric sputtering".

Atmospheric sputtering affects the long term evolution of these atmospheres. The increased exobase temperatures can enhance Jeans escape by the lightest components, typically H or H_2. In addition, the energy transfer to the atoms in the thermosphere by momentum transfer collisions, often referred to as knock-on collisions, is much less sensitive to the mass of the escaping species and, therefore, can lead to enhanced loss of all atmospheric constituents, which is the atmospheric sputtering process (Johnson 1990, 1994). To estimate this contribution to atmospheric loss, sputtering is often divided into two components: those incident ions which penetrate the exobase and enter the thermosphere and those which only pass through the corona. For the penetrating particles, a cascade of momentum transfer collisions is initiated in the thermosphere by the incident particles. This forms a population of "hot" atoms and molecules. For the other contribution, ejection can occur in single collisions of the incident ion with a coronal molecule and by charge exchange in which the fast ion is replaced by a fast escaping neutral. The relative importance depends on the extent of the corona, the escape energy, and the escape depth from the thermosphere (cf. Johnson et al. 2008).

The composition of the thermosphere near the exobase is often atomic: e.g., O, N, or H atoms. When the composition is molecular, as it the case at Titan and Io for example, an energetic plasma ion transfers energy in close collisions with an individual atom in a molecule. These collisions cause dissociation and produce energetic fragments. Therefore,

in both atomic and molecular thermospheres, energetic "secondary atoms" are set in motion. These hot atoms either populate the corona or make further collisions with the constituents of the thermosphere. As the energies of these recoil atoms decrease, whole molecules are eventually set in motion in a molecular thermosphere (Johnson and Liu 1998). This leads to molecular escape, a process which dominates at Io (McGrath and Johnson 1987; Pospieszalska and Johnson 1996; McGrath et al. 2004).

Solar wind ions can have access to the atmospheres of bodies like Venus, Mars and Pluto that are unprotected by a magnetosphere. These are predominantly light ions that cause ionization and charge exchange but are otherwise inefficient sputtering agents. Therefore, atmospheric sputtering is dominated by locally formed ions referred to as pick-up ions (Luhmann et al. 1992; Johnson et al. 2008; Lammer et al. 2008). These ions are formed in the extended corona by electron and photon impact and by charge exchange and are accelerated by the local fields. They can either be swept away, a loss process, or can re-impact the atmospheric exobase causing sputtering. In the case of bodies trapped in a planetary magnetosphere, an additional enhancement can occur. Atoms and molecules that have escaped from the satellites or ring particles and are ionized in the rotating magnetosphere become trapped and accumulate, forming a toroidal plasma in the magnetosphere. This accumulated plasma can enhance the sputtering effect, but also provides an impacting plasma that consists of both light and heavy ions representative of the composition of the atmosphere of a satellite embedded in the magnetosphere.

Such ion acceleration processes also occur in an object's atmosphere. That is, neutrals are similarly ionized by electrons, photons or charge exchange in the object's ionosphere. If the local fields penetrate into the corona, or even below the exobase as seen at Titan and Mars, the newly formed ions can be accelerated by local electric fields. At the Earth the fields are associated with its rotating magnetosphere. At Venus, Mars and Pluto they are the induced fields due to interaction of the ionosphere with the solar wind, and on Io, Titan and Triton, they are due to the induced fields associated with the interaction of the atmosphere with the giant planet's magnetosphere (Ma et al. 2008).

The ions formed in the corona and those formed below the exobase clearly have a composition characteristic of the atmosphere and are called locally produced pick-up ions. Therefore, their detection in the ambient plasma can lead to information on the composition in the exobase region. The ionospheric outflow and pick-up in the corona are typically artificially separated, although the spatial transition from one to the other is smooth. Both sets of ions can result in loss by being swept away down the tail of the interaction region, and they can cause atmospheric sputtering by momentum transfer collisions both in the corona or below the exobase. To date the focus has been on the ions formed and accelerated in the corona. However, the ions dragged out of the atmosphere, often called "ionospheric outflow" (e.g., Fox 1997; Ma and Nagy 2007) are critically important to atmospheric loss and heating at Io (Wilson et al. 2002; Mendillo et al. 2007) and, likely, at Titan (Johnson 2008). Ions that are swept down the tail of the interaction region are an important atmospheric loss process. In addition, depending on their path length in the atmosphere's corona they can cause further ionization by charge exchange. Pick-up ions also make momentum transfer collisions in the atmosphere, both those re-impacting ions formed in the corona and the ionospheric outflow. This populates and expands the corona (Michael and Johnson 2005) producing a complex feedback process. That is, pick-up ions formed in the corona and in the atmosphere can enhance the population of the corona and, thereby, enhance the pick-up ion production and atmospheric loss (Johnson and Luhmann 1998). Approximate models for this complex interaction have been made in which the coronal processes and the ionospheric outflow are separated, but complete simulations are only recently available (Chaufray et al. 2007).

The energy deposited produces hot atoms and molecules both by dissociation or by direct momentum transfer collisions with incident ions and the energetic neutral atoms (ENAs) formed by charge exchange. In this way energized molecular fragments are seen in emission, as discussed earlier, and can initiate a set of collision processes often referred to as a collision cascade. Of particular interest is the energy that goes into producing atmospheric escape and the hot corona (e.g., Michael et al. 2005; Shematovich et al. 2003; Cipriani et al. 2007). The cascades can be described by direct solution of the transport equations, by analytic approximations to the transport equation, or by Monte Carlo simulation. Johnson et al. (2000) have compared such models for a simple O thermosphere energized by an incident O^+ pick-up ion plasma.

4.1 Transport Equations

Consistent with what was described above, a set of kinetic, time-independent Boltzmann equations for the incident particles and the atmospheric particles can in principal be written and solved. There is one such equation for each species i,

$$\mathbf{v}\partial f_i/\partial \mathbf{r} + \mathbf{g}\partial f_i/\partial \mathbf{v} = Q_i - L_i + \sum_j J_{ij}(f_i, f_j). \tag{34}$$

Here the $f_i(\mathbf{r}, \mathbf{v})$ are the distribution functions for the translational and internal degrees of freedom for particles i in the atmosphere, $\mathbf{g}$ is the gravitational acceleration, Q_i and L_i are source and loss functions for species i, and the J_{ij} describe the collisions in the atmosphere (momentum transfer excitations, dissociation, ionization, and charge transfer collisions) between particles i and all other particles j. In 1-D, single component atmospheres, such equations have been solved. Although such equations are often written down for the purpose of discussing the importance of the various processes, they are almost never solved when the spatial distribution of hot recoils is required.

4.2 Analytic Models

A useful approximation to the Boltzmann equation gives the energy distribution of recoils for a single component atmosphere. This is obtained by integrating over the spatial dimensions and ignoring gravity. It has been shown that the total number of recoils with energy between E and $E + dE$ produced by a hot atom of energy E_o colliding in a background atmosphere of identical atoms is

$$G(E_o, E_i) \approx \beta_n E_o/E^2. \tag{35}$$

This is obtained analytically as the lead term in the distribution by assuming an interaction potential which is a power law with power n where β_n is a constant that varies slowly with n. This remarkably simple expression can be used to give the energy distribution of recoil particles moving locally in a planetary thermosphere:

$$f(E) \approx \phi(E_o)G(E_o, E)/\nu_m(E). \tag{36}$$

Here $\phi(E_o)$ is the local rate at which atoms of energy E_o are initially produced by dissociation or momentum transfer collisions by the incident ions and $\nu_m(E)$ is momentum transfer collision frequency at the local density for atoms of energy E. This result can be used to describe the hot atoms in the exobase region and, thereby, give simple expressions for the

rates of production of sputtering and of the production of the hot corona. In addition, if the spatial morphology of incident radiation is known such expressions can be used to obtain the spatial structure of the hot corona.

These simple expressions were compared to atmospheric loss simulations for an O thermosphere and shown to be accurate (Johnson et al. 2000). Cipriani et al. (2007) simulated a more complex Martian atmosphere, involving both atoms and molecules excited by dissociative recombination and ion sputtering, using Monte Carlo simulations described below. They compared their steady-state recoil distribution to the expression for the total number of recoils produced, $G(E_o, E)$ rather than $f(E)$, and concluded the analytic model was only approximate. However, their steady-state recoil distributions produced by either dissociation or ion-induced sputtering compare well with the correct expression, $f(E)$ (Johnson 2008). Remarkably, the analytic expression for $f(E)$ compares well even for the steady-state distribution of molecular recoils found by Cipriani et al. (2007).

4.3 Monte Carlo Simulations

Since the above transport equations are usually not solved, simulations that are equivalent to such solutions are carried out. There are two principal types of simulations and sometimes a combination of these is used (Leblanc and Johnson 2001). 1-D, 2-D and 3-D versions have been implemented depending on the aspect being described. The most common model is a test particle simulation in which the incident radiation sets representative atoms and molecules in motion. These hot atoms and molecules, also called primary recoils, are tracked as they move under the influence of gravity in a background atmosphere obtained either from observations or a model. The hot recoils interact with the background gas causing additional excitations and momentum transfer collisions producing additional recoils. In this cascade of collisions the deposited energy can be transported away from the initial energy deposition site and a distribution of hot particles is produced. In this way the collisional energy deposited by each incident ion is rapidly dispersed. Whereas the transport equations and other approximations above typically assume some steady state for a given incoming flux, in the Monte Carlo simulations the fate of the energy deposited by sample ions, called test particles, is tracked (e.g., Shematovich et al. 1994).

The test particles are assigned a weight such that the net production rate represents the hot particle source profiles described earlier. The initially produced hot particles and their recoils are tracked until they fall below some energy cut-off after which they are assumed to be part of the background atmosphere. The size of this energy cut-off depends on what aspect of the atmosphere is being modeled, the escape rate, the structure of the corona, or the local heating, in which case the energy must be tracked to some value related to the ambient temperature.

The representative particles are tracked ballistically for time steps which are short enough that the collision probability is small. At the end of the time step the velocities of the particles are changed to account for the outcome of those collisions that occurred. These new velocities are used as the initial velocities for the next time step. Because the collision probability along the path of a hot particle and the outcome of each collision are typically chosen using a Monte Carlo procedure, these are referred to as Monte Carlo simulations.

Whereas only hot particles are tracked in the test particle method, in the second type of simulation the background atmosphere is allowed to evolve in response to the energy deposition by hot particle production (e.g., Michael and Johnson 2005). Therefore, both representative hot particles and representative atmospheric molecules are tracked. In such simulations collisions are allowed to occur between hot particles, between hot particles and

atmospheric particles, and between atmospheric particles, each having weights that allow the representative particles to describe both the source distribution and the atmospheric structure and temperature. Because such simulations are computationally intensive, the computational zone has a lower boundary at which temperatures and densities are assigned. These are made to be consistent with the properties found by continuum models of the atmosphere at that depth. The lower boundary typically occurs at a depth at which the energy deposition can be neglected or treated by a continuous slowing down (CSDA) model. The upper boundary is typically where collisions are improbable and the hot particles are in ballistic orbits. Particles reaching the upper boundary are tested and either escape and are removed or are allowed to re-enter the atmosphere as appropriate to their ballistic trajectory.

Since the atmosphere is allowed to respond to the energy deposition in such simulations, care must be taken to account for energy loss processes other than conduction to the lower boundary which is automatically included. Following Bird (1994) these are often referred to as Direct Simulation Monte Carlo (DSMC) models.

In both types of simulations, the weights for different species in a multi-component atmosphere can be different, so that trace species can be accurately accounted for. In addition, the atmosphere is divided into cells in which its properties do not change significantly, so that random particles in each cell can be used to describe the outcome of the collisions. Most simulations use the method in Bird (1994) (e.g., Leblanc and Johnson 2001; Michael and Johnson 2005) to describe the collision probabilities based on the weights and densities of each type of particle. The accuracy and computational time are optimized by the choice of collision model, weights, time step, cell sizes and the simulation type used in each region of the atmosphere. For instance, in describing the transition from the thermosphere to the exosphere, weights that are different in different regions are often used as well as different simulation models which are coupled at the boundary between the regions. Such models have been used to directly produce the corona and to test the simpler analytic models (cf., Johnson et al. 2008; Lammer et al. 2008).

4.4 Energetic Particle Deposition

Based on the discussions above, there are a number of effects produced by the incident radiation: auroral emissions, an ionosphere, thermospheric heating, sputter loss, etc. These effects typically peak at very different depths in the atmosphere; therefore the relevance of the various radiation types depends both on the slant depth into the atmosphere as well as the energy flux for each type of incident radiation. The quantity of interest is the energy deposition per unit volume per unit time. This is the radiation flux, $\phi(z)$ at each altitude, z, times the energy deposited per unit path length by the incident particles. The latter quantity is called the stopping power of the medium and is typically written as (dE/dx) where x is along the path of the incident particles. The dependence of ϕ on depth and the redistribution of the deposited energy is determined by transport processes. Here the focus is on the energy deposition by different charged particle types via (dE/dx) and the penetration depths. Comparisons with the effect of the photon flux (e.g., Michael and Johnson 2005; Johnson 2008) are hampered by the fact that dE/dx for energetic ions and electrons are not very sensitive to the atmospheric composition, but the energy deposition by the solar flux UV and EUV flux, as well as the low energy electrons (≤ 100 eV) are very specific to the composition.

The energy lost per unit path length depends on the density of the atmosphere, and thus one often writes $dE/dx = \sum_i (n_i S_i)$, where n_i is the local number density for atmospheric molecules i and S_i is called the stopping cross section for the incident particle by molecules of type i. For incident ions S is divided into qualitatively different types of energy

Table 4 W-values (in eV) and ratios W/I

Gas	w	W/I
He	44	1.8
Ar	27	1.7
H_2	36	2.3
N_2	37	2.4
O_2	31	2.6
CO	34	2.4
CO_2	34	2.5
H_2O	30	2.4
NH_3	26	2.5
CH_4	31	2.5
C_2H_6	25	2.1
C_2H_4	26	2.5
C_2H_2	26	2.3
SO_2	32	2.6

transfer, as mentioned earlier: momentum transfer to the atmospheric atoms and molecules, often referred to as the elastic nuclear component, S_n, which also scatters the incident ions, and energy transfer to excitations and ionizations of the atmospheric atoms and molecules, S_e. Incident electrons are also scattered, especially at low energies, but the direct energy/momentum transfer to atomic motion is typically negligible.

Because the amount of energy transferred depends on the nuclear charge of the molecules, which is nearly proportional to its mass and equals the number of electrons available for excitation, the stopping power is often divided by the mass density, ρ. This gives a quantity that for fast ions and electrons is nearly material independent: $(dE/dx)/\rho$. Therefore, in Fig. 16 we compare the stopping powers of an electron, proton and O^+ ion in H_2O as a function of the incident velocity, v, given as the kinetic energy per unit mass. Such results can be obtained for a variety of incident ion/target combinations using freeware programs such as SRIM (http://www.srim.org/). It is seen that at velocities above the Bohr velocity (2.18×10^8 cm s^{-1}), the variation with velocity for each incident particle is similar, until one reaches very high velocities (e.g., $\sim$ a fraction of c or a few MeV/u) where radiation losses come into play. That is, the amount of energy deposited in the target electrons and ions is determined primarily by the speed of the charged particles over a broad range of relevant energies (e.g., Johnson 1990). Also shown in Fig. 17 is the projected range, or penetration depth, of these particles versus velocity, again given as their initial energy per unit mass. Because the atmospheric density versus altitude depends on the local gravity and temperature, the range is also multiplied by the mass density, giving the atmospheric mass per unit area penetrated by the particles. This is a quantity that is again nearly independent of atmospheric type.

There have been numerous studies of the fraction of energy deposited by fast ions and electrons in electronic excitations and ionizations (e.g., Paretzke 1989). The latter process, like photoionization, produces secondary electrons (Long and Paretzke 1991). As a rule, fast incident charged particles expend $\sim 50-60$ eV per ionization, so that the secondary electrons carry off a considerable fraction of the deposited energy. Since these electrons can also ionize and excite atmospheric molecules, the average energy deposited per ionization produced by either the incident particle or a secondary electron is called the W-value. Quite

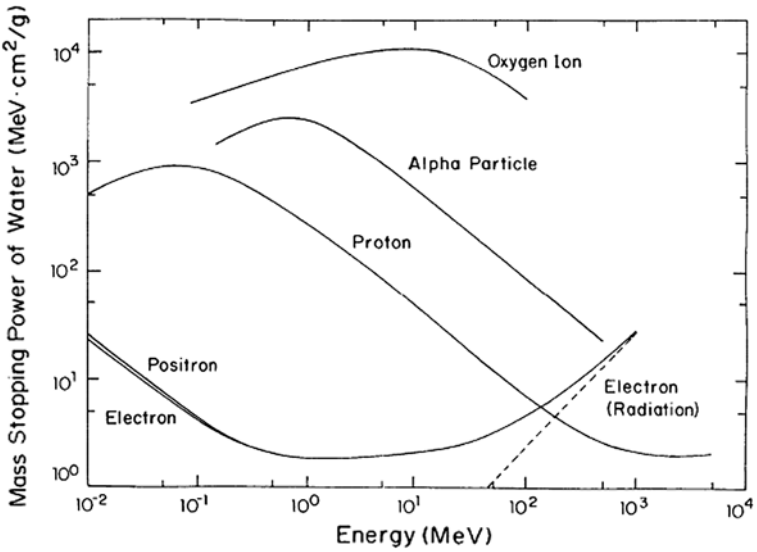

Fig. 16 Stopping power (dE/dx) of a material versus ion energy. Here water vapor is used and the stopping power is given as an energy loss per mass column density penetrated. For the energy range shown this quantity is nearly independent of material, i.e., multiply by the mass density of the material to obtain energy loss per unit path length (from Johnson 1990)

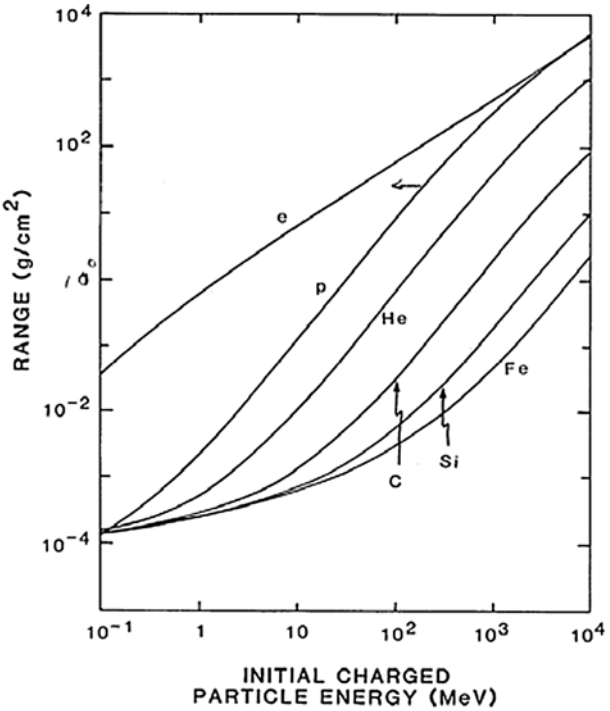

Fig. 17 Range (distance an incident ion travels in a material) versus ion energy. Range is given as a mass column density penetrated; the material is again water vapor, but is similar for most atmospheric compositions, i.e., divide by mass density to get distance traveled

remarkably this is nearly constant for fast ions and electrons, as is the fraction of the deposited energy going into excitations. Values for relevant gases are given in Table 4. It is seen that the W for a molecular atmosphere is $\sim 2.5\,I$, so the fast ions and electrons expend, on the average, more energy per ionization produced than is typical for EUV-UV photons described earlier. In a molecular atmosphere, the fraction of the deposited energy going into electronic excited states is $\sim 10\%$ and the energy dissipated by the secondary electrons in elastic collisions and vibrational excitations is $\sim 50\%$ of the total energy deposited. In addition, the ionizations produced by the incident plasma ions and electrons are distributed spatially very differently than are those produced by incident UV and EUV photons.

5 Summary and Conclusions

We have discussed here the energy deposition of solar photons and charged particles of various origins, with emphasis on problems of current interest. For photons, these include determining EUV and FUV heating efficiencies, for which the principal unknown is the fraction of energy that appears as vibrational excitation of molecules in various processes. These heating processes occur in competition with other external perturbations such as meteoroid bombardment. We have discussed the validity of Chapman layer theory. By comparison of a Chapman layer to a detailed, realistic model, we have shown that more elaborately modeled electron density profiles bear little resemblance to Chapman layers.

We have shown that modeling the photodissociation rates of many thermospheric molecules is difficult for several reasons. For photodissociations that proceed by excitation to discrete states followed by predissociation, the cross sections must be known to very high resolution, of the order of 10^{-3} Å. For most atmospheric molecules, there are wavelength regions in which the cross sections are highly oscillatory on such wavelength scales. Branching ratios for the production of various electronically excited states of the products of dissociation are also required, and are not generally known. Immediately shortward of the ionization thresholds of molecules, the photoabsorption cross sections are usually highly structured, and autoionization competes with predissociation. In this region, the photodissociation cross sections need to be determined as the difference between the photoabsorption cross sections and the photoionization cross sections, a process that is difficult and usually produces only approximations.

We have also discussed the interaction of X-rays with atmospheric species, in particular the Auger effect, and the production of characteristic X-rays from atoms and molecules. We have described the Auger effect in detail for atoms for O and that for molecules for N_2. Auger electrons have been observed or predicted in photoelectron flux spectra from several planetary bodies, as have X-rays of various origins. The Auger process and double ionization of valence shell electrons produce doubly ionized species of uncertain lifetime. Recent measurements have provided a basis for the construction of approximate models of such species. Much more data is needed, however, in order to accurately model their density profiles, especially for doubly ionized molecules.

Analyses of emissions are valuable for remote-sensing of auroral particles, which precipitate into the upper atmosphere of a solar system body, where they deposit their energy. Spectroscopic analyses of auroral emissions based on color ratios and spectral profiles have been used to identify the type of precipitating particles and to determine their characteristics in terms of total energy flux and mean energy or spectral shape. This information is crucial for identifying the origin of the auroral particles and the associated forcing, for assessing the global response of a planetary upper atmosphere to auroral particles, and to infer

the ionospheric contribution to magnetosphere–ionosphere coupling. Based on a cross body comparison, we have highlighted the differences in applying similar spectroscopic techniques at different solar system bodies. The auroral particle energy range covered by the analysis, the type of aurora which can be probed, and the physical quantities derived from the analysis vary from one solar system body to another. Multi-spectral analyses of auroral emissions have been employed for increasing the auroral particle energy range covered by only one technique, for determining the characteristics of more than one auroral particle type, and for constraining the atmospheric model used for the analysis.

The upper atmospheres of planets and planetary satellites are often affected by energetic ions and electrons, either locally created or from an ambient plasma. Since these ions and electrons are in turn affected by the local fields, there are complex feedback processes that affect the atmospheric heating and loss rates. Whereas the effect of solar photons on the upper atmosphere has been studied for years, only recently has accurate modeling of the plasma interactions been carried out, as discussed in the other articles of this volume. In addition, it is only very recently that we have had good spacecraft measurements of thermospheres other than that of the Earth to test such models.

Assuming one knows the local plasma flux, in this article we described briefly how one calculates the energy deposition rate. As is the case for photon-energy deposition, our ability to describe the effect of the incident and locally produced plasma particles is limited by the available atomic and molecular data. However, as pointed out in the text, for fast ions and electrons the energy deposition rates are much less sensitive to the atmospheric composition than is the case for incident photon or low energy incident or secondary electrons. When the energy deposition by the energetic plasma particles can be calculated, then the subsequent modeling of the atmospheric processes is roughly independent of the exciting radiation. That is, the subsequent processes are very similar to those initiated by photo-absorption. We also pointed out the similarity in the effect of hot recoils on atmospheric heating, whether the recoils are produced by incident ions or exothermic chemistry. Therefore, the principal limiting factor in our ability to describe the heating of the upper atmosphere by the incident plasma is our knowledge, from spacecraft measurements or modeling efforts, of the morphology of the plasma flow into the atmosphere and our knowledge of the fields that penetrate the atmosphere, issues discussed in later articles in this volume.

Acknowledgements JLF acknowledges partial support from the NASA Planetary Atmospheres Program under grant NNG06GF12G and from the NASA Mars Fundamental Research Program under grant NNG05GL82G to Wright State University. REJ acknowledges support from NASA's Planetary Atmospheres Program under grant NNG06GC09G to the University of Virginia.

References

H. Abgrall, E. Roueff, X. Liu, D.E. Shemansky, Astrophys. J. **481**, 557–566 (1997)

K. Ågren, J.-E. Wahlund, R. Modolo, D. Lummerzheim, M. Galand, I. Müller-Wodarg et al., Ann. Geophys. **25**, 2359–2369 (2007)

J.M. Ajello, D.E. Shemansky, W.R. Pryor, A.I. Stewart, K.E. Simmons, T. Majeed, J.H. Waite, G.R. Gladstone, D. Grodent, Icarus **152**, 151–171 (2001). doi:10.1006/icar.2001.6619

J.M. Ajello, W. Pryor, L. Esposito, A.I. Stewart, W. McClintock, J. Gustin, D. Grodent, J.-C. Gerard, T. Clarke, Icarus **178**, 327 (2005).

A. Aksnes, J. Stadsnes, G. Lu, N. Østgaard, R.R. Vondrak, D.L. Detrick, T.J. Rosenberg, G.A. Germany, M. Schulz, Ann. Geophys. **22**, 475–496 (2004)

A. Aksnes, J. Stadsnes, N. Østgaard, G.A. Germany, K. Oksavik, R.R. Vondrak, A. Brekke, U.P. Løvhaug, J. Geophys. Res. **111**, A02301 (2006). doi:10.1029/2005JA011331

A.C. Allison, S.L. Guberman, A. Dalgarno, J. Geophys. Res. **87**, 923–925 (1982)

A.C. Allison, S.L. Guberman, A. Dalgarno, J. Geophys. Res. **91**, 10,193–10,198 (1986)
A.D. Anbar, M. Allen, H.A. Nair, J. Geophys. Res. **98**, 10,925–10,931 (1993)
S.K. Atreya, M.H. Wong, T.C. Owen, P.R. Mahaffy, H.B. Niemann, I. de Pater, P. Drossart, Th. Encrenaz, Planet. Space Sci. **47**, 1243–1262 (1999)
S.V. Avakyan, Kosm. Issl. **16**, 144–148 (1978)
S.V. Avakyan, Cosmic Res. **17**, 786–789 (1980)
S.M. Bailey, T.N. Woods, C.A. Barth, S.C. Solomon, L.R. Canfield, R. Korde, J. Geophys. Res. **105**, 27,179–27,193 (2000)
K.H. Baines, H.B. Hammel, K.A. Rages, P.N. Romani, R.S. Samuelson, in *Neptune and Triton*, ed. by D.P. Cruikshank (University of Arizona Press, Tucson, 1995)
N. Balakrishnan, M.J. Jamieson, A. Dalgarno, Y. Li, R.J. Buenker, J. Chem. Phys. **112**, 1255–1259 (2000)
P.M. Banks, G. Kockarts, *Aeronomy* (Academic Press, New York, 1973)
B. Basu, D.T. Decker, J.R. Jasperse, J. Geophys. Res. **106**, 93–105 (2001)
S.J. Bauer, *Physics of Planetary Ionospheres* (Springer, New York, 1973)
S.J. Bauer, H. Lammer, *Planetary Aeronomy* (Springer, Berlin, 2004)
M. Benndorf, W.B. Westerveld, J.V. Eck, J.V.D. Weg, H.G.M. Heideman, Chem. Phys. Lett. **286**, 321–328 (1998)
J. Berkowitz, *Atomic and Molecular Photoabsorption* (Academic Press, San Diego, 2002)
A. Bhardwaj, G.R. Gladstone, Rev. Geophys. **38**, 295–353 (2000)
A. Bhardwaj, G. Branduardi-Raymont, R.F. Elsner, G.R. Gladstone, G. Ramsay, P. Rodriguez, R. Soria, J.H. Waite Jr., T.E. Cravens, Geophys. Res. Lett. **32**, L03S08 (2005a). doi:10.1029/2004GL021497
A. Bhardwaj, R.F. Elsner, J.H. Waite Jr., G.R. Gladstone, T.E. Cravens, P.F. Ford, Astrophys. J. **627**, L73–L76 (2005b)
A. Bhardwaj, R. Gladstone, R. Elsner, N. Østgaard, H. Waite, T. Cravens, S.-W. Chang, T. Majeed, A. Metzger, J. Atmos. Sol.-Terr. Phys. **69**, 179–187 (2007b). doi:10.1016/j.jastp.2006.07.011
A. Bhardwaj et al., Planet. Space Sci. **55**, 1135–1189 (2007a). doi:10.1016/j.Planet.SpaceSci.2006.11.009
G.A. Bird, *Molecular Gas Dynamics and the Direct Simulation of Gas Flows* (Clarendon, Oxford, England, 1994)
J.H. Black, E.F. van Dishoeck, Astrophys. J. **322**, 412–449 (1987)
S.W. Bougher, R.G. Roble, E.C. Ridley, R.E. Dickinson, J. Geophys. Res. **95**, 14,811–14,827 (1990)
S.W. Bougher, P.-L. Blelly, M. Combi, J.L. Fox, I. Mueller-Wodarg, A. Ridley, R.G. Roble, Space Sci. Rev. (2008, this issue)
G. Branduardi-Raymont, A. Bhardwaj, R.F. Elsner, G.R. Gladstone, G. Ramsay, P. Rodriguez, R. Soria, J.H. Waite Jr., T.E. Cravens, Astron. Astrophys. **463**, 761–774 (2007). doi:10.1051/00046361:20066406
G. Branduardi-Raymont, R.F. Elsner, M. Galand, D. Grodent, T.E. Cravens, P. Ford, G.R. Gladstone, J.H. Waite Jr., J. Geophys. Res. **113**, A02202 (2008). doi:10.1029/2007JA012600
D.H. Brautigam, M.S. Gussenhoven, D.A. Hardy, J. Geophys. Res. **96**(A4), 5525–5538 (1991)
B. Brehm, G. de Frênes, Int. J. Mass Spectrom. Ion Proc., 251–266 (1978)
E.L. Breig, M.R. Torr, D.G. Torr, W.B. Hanson, J.H. Hoffman, J.C.G. Walker, A.O. Nier, J. Geophys. Res. **82**, 1008–1012 (1977)
E.L. Breig, M.R. Torr, D.C. Kayser, J. Geophys. Res. **87**, 7653–7665 (1982)
C.D. Caldwell, M.O. Krause, Phys. Rev. A **47**, R759–R762 (1993)
R.W. Carlson, J. Chem. Phys. **60**, 2350–2352 (1974)
S.L. Carter, H.P. Kelly, J. Phys. B **9**, 1887–1897 (1976)
J.W. Chamberlain, D.M. Hunten, *Theory of Planetary Atmospheres* (Academic Press, Orlando, 1987)
S. Chapman, Proc. Phys. Soc. Lond. **43**, 26–45 (1931a)
S. Chapman, Proc. Phys. Soc. Lond. **43**, 483–501 (1931b)
B.K. Chatterjee, R. Johnsen, J. Chem. Phys. **91**, 1378–1379 (1989)
J.Y. Chaufray, R. Modolo, F. Leblanc, G. Chanteur, R.E. Johnson, J.G. Luhmann, J. Geophys. Res. **112**, E09009 (2007). doi:10.1029/2007JE002915
M.W. Chen, M. Schulz, P.C. Anderson, G. Lu, G. Germany, M. Wüest, J. Geophys. Res. **110**, A03210 (2005). doi:10.1029/2004JA010725
A.S.-C. Cheung, K. Yoshino, J.R. Esmond, W.H. Parkinson, J. Mol. Spectrosc. **178**, 66–77 (1996)
F. Cipriani, F. Leblanc, J.J. Berthelier, J. Geophys. Res. **E07001**, (2007). doi:10.1029/2006JE00281
E.U. Condon, G.H. Shortley, *Theory of Atomic Spectra* (Cambridge University Press, Cambridge, 1964)
B. Coquert, M.F. Merienne, A. Jenouvrier, Planet. Space. Sci. **38**, 287–300 (1990)
P.C. Cosby, R. Möller, H. Helm, Phys. Rev. A **28**, 766–722 (1983)
B. Craseman, in *Atomic, Molecular and Optical Physics Handbook*, 2nd edn. ed. by G.W.F. Drake (American Institute of Physics Press, Woodbury, 2006), pp. 915–928
T.E. Cravens, Science **296**, 1042–1045 (2002)
T.E. Cravens, E. Howell, J.H. Waite Jr., G.R. Gladstone, J. Geophys. Res. **100**, 17,153–17,161 (1995)

T.E. Cravens, J. Vann, J. Clark, J. Yu, C.N. Keller, C. Brull, Adv. Space Res. **33**, 212–215 (2004)
T.E. Cravens, T.E. Cravens, I.P. Robertson, J. Clark, J.-E. Wahlund, J.H. Waite Jr., S.A. Ledvina, H.B. Niemann, R.V. Yelle, W.T. Kasprzak, J.G. Luhmann, R.L. McNutt, W.H. Ip, V. De La Haye, I. Mueller-Wodarg, D.T. Young, A.J. Coates, Geophys. Res. Lett. **32**, L12108 (2005). doi:10.1029/2005GL023249
J.M. Curtis, R.K. Boyd, J. Chem. Phys. **80**, 1150–1161 (1984)
A. Dalgarno, G.H. Herzberg, T.L. Stevens, Astrophys J. **162**, L47 (1970)
I. de Pater, J.J. Lissauer, *Planetary Sciences* (Cambridge University Press, Cambridge, 2001)
I. de Pater, S.T. Massie, Icarus **62**, 143–171 (1985)
A. Dalgarno, H.R. Sadeghpour, Phys. Rev. A **46**, R3591–R3593 (1992)
D.R. Denne, J. Phys. D **3**, 1392–1398 (1970)
K. Dennerl, V. Astron. Astrophys. **386**, 319–330 (2002)
K. Dennerl, V. Burwitz, J. Englhauser, C. Lisse, S. Wolke, Astron. Astrophys. **386**, 319–330 (2002)
R.A. Doe, J.D. Kelly, D. Lummerzheim, G.K. Parks, M.J. Brittnacher, G.A. Germany, J. Spann, Geophys. Res. Lett. **24**(8), 999–1002 (1997)
D.P. Drob, R.R. Meier, J.M. Picone, D.J. Strickland, R.J. Cox, A.C. Nicholas, J. Geophys. Res. **104**, 4267 (1999)
G. Dujardin, M.J. Besnard, L. Heller, Y. Malinovich, Phys. Rev. A **35**, 5012–5019 (1987)
R.H. Eather, Rev. Geophys. **5**, 207–285 (1967)
A.K. Edwards, R.M. Wood, J. Chem. Phys. **76**, 2938–2942 (1982)
A. Ehresmann, S. Machida, M. Kitayama, M. Ukai, K. Kameta, N. Kouichi, Y. Hatano, E. Shigemasa, T. Hayashi, J. Phys. B **33**, 473–490 (2000)
R.F. Elsner et al., J. Geophys. Res. **110**, A10207 (2005). doi:10.1029/2004JA010717
L.W. Esposito, R.G. Knollenberg, M. Ya Marov, O.B. Toon, R.P. Turco, in *Venus* (University of Arizona Press, Tucson, 1983)
L.W. Esposito, J.-L. Bertaux, V. Krasnopolsky, V.I. Moroz, L.V. Zasova, in *Venus II*, ed. by S.W. Bougher, D.M. Hunten, R.J. Phillips (University of Arizona Press, Tucson, 1997)
E. Fainelli, R. Maracci, L. Avaldi, J. Electron. Spectrosc. Rad. Transf. **123**, 277–286 (2002)
X. Fang, M.W. Liemohn, J.U. Kozyra, S.C. Solomon, J. Geophys. Res. **110**, A07302 (2005). doi:10.1029/2004JA010915
M.O. Fillingim, G.K. Parks, H.U. Frey, T.J. Immel, S.B. Mende, Geophys. Res. Lett. **32**, L03113 (2005). doi:10.1029/2004GL021635
J.L. Fox, Planet. Space Sci. **36**, 37–46 (1988)
J.L. Fox, Geophys. Res. Lett. **24**, 2901–2904 (1997)
J.L. Fox, J. Geophys. Res. **109**, A11310 (2004). doi:10.1029/2004JA010380
J.L. Fox, Icarus 192 (2007). doi:10.1016/j.icarus2007.05.02
J.L. Fox, J.H. Black, Geophys. Res. Lett. **16**, 291–294 (1989)
J.L. Fox, A. Dalgarno, J. Geophys. Res. **84**, 7315–7333 (1979)
J.L. Fox, A. Dalgarno, J. Geophys. Res. **86**, 629–639 (1981)
J.L. Fox, A.I.F. Stewart, Geophys. Res. **96**(A6), 9821–9828 (1991)
J.L. Fox, G.A. Victor, J. Geophys. Res. **86**, 2438–2442 (1981)
J.L. Fox, P. Zhou, S.W. Bougher, Adv. Space Res. **17**, (11)203–(11)218 (1995)
R. Franceschi, R. Thissen, J. Žabka, J. Roithová, Z. Herman, O. Dutuit, Int. J. Mass Spectrom. Ion Proc. **228**, 507–516 (2003)
H.U. Frey, Rev. Geophys. **45**, RG1003 (2007). doi:10.1029/2005RG000174
H.U. Frey, S.B. Mende, T.J. Immel, S.A. Fuselier, E.S. Claflin, J.-C. Gérard, B. Hubert, J. Geophys. Res. **107**(A7), 1091 (2002). doi:10.1029/2001JA900161
T.J. Fuller-Rowell, D.S. Evans, J. Geophys. Res. **92**, 7606 (1987)
M. Galand, S. Chakrabarti, J. Atmos. Terr. Phys. **68**, 1488–1501 (2006). doi:10.1016/jastp.2005.04.013
M. Galand, S. Chakrabarti, in *Atmospheres in the Solar System: Comparative Aeronomy*, ed. by M. Mendillo, A. Nagy, H. Waite, AGU Monograph, vol. 130 (AGU Press, 2002), pp. 55–76
M. Galand, D. Lummerzheim, J. Geophys. Res. **109**(A3), A03307 (2004). doi:10.1029/2003JA010321
M. Galand, J. Lilensten, W. Kofman, R.B. Sidje, J. Geophys. Res. **102**, 22,261–22,272 (1997)
M. Galand, R. Roble, D. Lummerzheim, J. Geophys. Res. **104**, 27,973–27,990 (1999)
M. Galand, T.J. Fuller-Rowell, M.V. Codrescu, J. Geophys. Res. **106**, 127–139 (2001)
M. Galand, D. Lummerzheim, A.W. Stephan, B.C. Bush, S. Chakrabarti, J. Geophys. Res. **107**(A7) (2002). doi:10.1029/2001JA000235
M. Galand, A. Bhardwaj, S. Chakrabarti, in *Advances in Geosciences*, vol. 2: Solar Terrestrial (ST) Science. Editor-in-Chief Wing-Huen Ip, Volume Editor-in-Chief Marc Duldig (2006), pp. 239–248
L. Gan, C.N. Keller, T.E. Cravens, Geophys. Res. **97**, 12,137–12,151 (1992)
J.-C. Gérard, D. Grodent, J. Gustin, A. Saglam, J.T. Clarke, J.T. Trauger, J. Geophys. Res. **109**, A09207 (2004). doi:10.1029/2004JA010513

G.A. Germany, G.K. Parks, M. Brittnacher, J. Cumnock, D. Lummerzheim, J.F. Spann, L. Chen, P.G. Richards, F.J. Rich, Geophys. Res. Lett. **24**, 995 (1997)
T. Gilbert, T.L. Grebner, I. Fischer, P. Chen, J. Chem. Phys. **110**, 5485–5488 (1999)
G.R. Gladstone, J. Geophys. Res. **97**, 1377–1387 (1992)
G.R. Gladstone, M. Allen, Y.L. Yung, Icarus **119**, 1–52 (1996)
G.R. Gladstone, S.A. Stern, D.C. Slater, M. Versteeg, M.W. Davis, K.D. Retherford, L.A. Young, A.J. Steffl, H. Throop, J.W. Parker, H.A. Weaver, A.F. Cheng, G.S. Orton, J.T. Clarke, J.D. Nichols, Science **318**, 229 (2007). doi:10.1126/science.1147613
M. Glass-Maujean, Phys. Rev. A **33**, 342–345 (1986)
M. Glass-Maujean, S. Klumpp, L. Werner, A. Ehresmann, H. Schmoranzer, J. Chem. Phys. **126**, 144303 (2007)
D. Grodent, J.H. Waite, J.-C. Gérard, J. Geophys. Res. **106**, 12,933 (2001)
G. Gronoff, J. Lilensten, C. Simon, O. Witasse, R. Thissen, O. Dutuit, C. Alcaraz, Astron. Astrophys. **465**, 641–645 (2007)
E.M. Gurrola, E.A. Marouf, V.R. Eshleman, G.L. Tyler, P.A. Rosen, in *Abstract Book* (AZ, Tucson, 1992), p. 28
J. Gustin, J.-C. Gerard, D. Grodent, S.W.H. Cowley, J.T. Clarke, A. Grard, J. Geophys. Res. **109**, A10205 (2004). doi:10.1029/2003JA010365
D.A. Hardy, M.S. Gussenhoven, D. Brautigam, J. Geophys. Res. **94**, 370–392 (1989)
J.H. Hecht, D.J. Strickland, M.G. Conde, J. Atmos. Sol.-Terr. Phys. **68**, 1502–1519 (2006). doi:10.1016/j.jastp.2005.06.022
H. Helm, P.C. Cosby, J. Chem. Phys. **90**, 4208–4215 (1989)
B.L. Henke, P. Lee, J. Tanaka, R.L. Shimabukuro, B.K. Fujikawa, Atomic Data Nucl. Data Tables **27**, 1–144 (1982)
B.L. Henke, E.M. Gullikson, J.C. Davis, Atomic Data Nucl. Data Tables **54**, 181–342 (1993)
L. Heroux, H.E. Hinteregger, J. Geophys. Res. **83**, 5305–5308 (1978)
G. Herzberg, *Spectra of Diatomic Molecules* (van Nostrand Reinhold, New York, 1950)
D.P. Hinson, J.D. Twicken, E.T. Karayel, J. Geophys. Res. **103**, 9505–9520 (1998)
H.E. Hinteregger, K. Fukui, B.R. Gibson, Geophys. Res. Lett. **8**, 1147–1150 (1981)
P. Honvault, M. Gargaud, M.C. Bacchus-Montabonel, R. McCarroll, Astron. Astrophys. **302**, 931–934 (1995)
F. Howorka, A.A. Viggiano, D.L. Albritton, E.E. Ferguson, F.C. Fehsenfeld, J. Geophys. Res. **84**, 5941–5942 (1979)
S. Hsieh, J.H.D. Eland, J. Phys. B **29**, 5795–5809 (1996)
J.H. Hubbell, W.J. Veigele, E.A. Briggs, R.T. Brown, D.T. Cromer, R.J. Howerton, J. Phys. Chem. Ref. Data **4**, 471–538 (1975)
D.L. Huestis, J. Quant. Spectrosc. Rad. Trans. **69**, 709–721 (2001)
D.L. Huestis et al., Space Sci. Rev. (2008, this issue)
T.J. Immel, S.B. Mende, H.U. Frey, L.M. Peticolas, C.W. Carlson, J.-C. Gérard, B. Hubert, S.A. Fuselier, J.L. Burch, Geophys. Res. Lett. **29**(11), 1519 (2002). doi:10.1029/2001GL013847
G. Israel et al., Nature **438** (2005), doi:10.1038/nature04349
B.M. Jakosky, R.M. Haberle, in *Mars*, ed. by H.H. Kieffer, B.M. Jakosky, C.W. Snyder, M.S. Matthews (University of Arizona Press, Tucson, 1992), pp. 969–1016
E. Jannitti, P. Nicoloso, G. Tondello, Physica Scripta **41**, 458–463 (1990)
R.E. Johnson, *Energetic Charged Particle Interactions with Atmospheres and Surfaces* (Springer, Berlin, 1990)
R.E. Johnson, Space Sci. Revs. **69**, 215–253 (1994)
R.E. Johnson, Proc. Royal Soc. (Lond.) (2008, in press)
R.E. Johnson, M. Liu, J. Geophys. Res. **103**, 3639–3647 (1998)
R.E. Johnson, J.G. Luhmann, J. Geophys. Res. **103**, 3649–3653 (1998)
P.V. Johnson, D. Schnellenberger, M.C. Wong, J. Geophys. Res. **105**, 1659–1670 (2000)
P.V. Johnson, C.P. Malone, I. Kanik, K. Tran, M.A. Khakoo, J. Geophys. Res. **110**, A11311 (2005). doi:10.1029/2005JA011295
R.E. Johnson, M.R. Combi, J.L. Fox, W.-H. Ip, F. Leblanc, M.A. McGrath, V.I. Shematovich, D.F. Strobel, J.H. Waite, Space Sci. Rev. (2008, this issue)
A.L. Jones, A.J. Blake, L. Torop, D.G. McCoy, Chem. Phys. **211**, 291–297 (1996)
R.T. Jongma, G. Berden, G. Meijer, J. Chem. Phys. **107**, 7034–7040 (1997)
P.S. Julienne, D. Neumann, M. Krauss, J. Chem. Phys. **64**, 2990–2996 (1976)
R.A. Kahn, T.Z. Martin, R.W. Zurek, S.W. Lee, in *Mars*, ed. by H.H. Kieffer, B.M. Jakosky, C.W. Snyder, M.S. Matthews (University of Arizona Press, Tucson, 1992), pp. 1017–1053
E. Kallio, S. Barabash, J. Geophys. Res. **106**, 165–177 (2001)

E. Kallio, J.G. Luhmann, S. Barabash, Charge exchange near Mars. J. Geophys. Res. **102**, 22,183–22,198 (1997)
C.N. Keller, T.E. Cravens, L. Gan, J. Geophys. Res. **97**, 12,117–12,135 (1992)
V. Kharchenko, A. Dalgarno, D.R. Schultz, P.C. Stancil, Geophys. Res. Lett. **33**, L11105 (2006). doi:10.1029/2006GL026039
Y.H. Kim, J.L. Fox, Geophys. Res. Lett. **18**, 123 (1991)
Y.H. Kim, J.L. Fox, Icarus **112**, 310–325 (1994)
J.H. Kim, S.J. Kim, T.R. Geballe, S.S. Kim, L.R. Brown, Icarus **185**, 476–486 (2006)
M. Kimura, Chem. Phys. Lett. **200**, 524–527 (1992)
H.R. Koslowski, H. Lebuis, V. Staemmler, R. Fink, J. Phys. B **24**, 5023–5034 (1991)
V.A. Krasnopolsky, D.P. Cruikshank, J. Geophys. Res. **100**, 21,271–21,286 (1995)
V.A. Krasnopolsky, B.R. Sandel, R. Herbert, R.J. Vervack, J. Geophys. Res. **98**, 3065–3078 (1993)
M.O. Krause, J. Phys. Chem. Ref. Data **8**, 307–327 (1979)
G.S. Kudryashev, S.V. Avakyan, Phys. Chem. Earth (C) **25**, 511–514 (2000)
J. La Coursiere, S.A. Meyer, G.W. Faris, T.G. Slanger, B.R. Lewis, S.T. Gibson, J. Chem. Phys. **110**, 1949–1958 (1999)
H. Lammer, J.F. Kasting, E. Chassefiére, R.E. Johnson, Y.N. Kulikov, F. Tian, Space Sci. Rev. (2008, this issue)
M. Larsson, P. Baltzer, S. Svensson, B. Wannberg, N. Martensson, A. Naves de Brito, N. Correia, M.P. Keane, M. Carlsson-Göthe, L. Karlsson, J. Phys. B **23**, 1175–1195 (1990)
M. Larsson, G. Sundström, L. Broström, S. Mannervik, J. Chem. Phys. **97**, 1750–1756 (1992)
P.P. Lavvas, A. Keystones, I.M. Vardavas, Planet. Space Sci. **56**, 67–99 (2008)
F. Leblanc, R.E. Johnson, Planet. Space Sci. **49**, 645–656 (2001)
F. Leblanc, O. Witasse, J. Winningham, D. Brain, J. Lilensten, P.-L. Blelly, R.A. Frahm, J.S. Halekas, J.L. Bertaux, J. Geophys. Res. **111**, A09313 (2006). doi:10.1029/2006JA011763
Ledvina et al., Space Sci. Rev. (2008, this issue)
L.C. Lee, C.C. Chiang, J. Chem. Phys. **78**, 688–691 (1983)
P.C. Lee, J.B. Nee, J. Chem. Phys. **112**, 1763–1768 (2000)
P.C. Lee, J.B. Nee, J. Chem. Phys. **114**, 792 (2001)
B.R. Lewis, S.T. Gibson, J.P. Sprengers, W. Ubachs, A. Johansson, C.G. Wahlströom, J. Chem. Phys. **123**, 23,601 (2005)
S.G. Lias, J.E. Bartmess, J.F. Liebman, J.L. Holmes, R.D. Levin, W.G. Mallard, Gas phase ion and neutral thermochemistry. J. Phys. Chem. Ref. Data **17**, 1–861 (1988)
D.R. Lide, *Editor in Chief, Handbook of Chemistry and Physics*, 88th edn. (Chemical Rubber Company Press, Boca Raton, 2008)
J. Lilensten, O. Witasse, C. Simon, H. Soldi-Lose, O. Dutuit, R. Thissen, C. Alcaraz, Geophys. Res. Lett. L03203 (2005). doi:10.1029/2004GL021432
J.J. Lin, D.W. Hwang, Y.T. Lee, X. Yang, J. Chem. Phys. **109**, 1758–1762 (1996)
K. Liou, P.T. Newell, C.-I. Meng, A.T.Y. Lui, M. Brittnacher, G. Parks, J. Geophys. Res. **102**, 27,197 (1997)
K. Liou, P.T. Newell, C.-I. Meng, M. Brittnacher, G. Parks, J. Geophys. Res. **103**(A8), 17,543–17,557 (1998)
K. Liou, P.T. Newell, C.-I. Meng, J. Geophys. Res. **106**(A4), 5531–5542 (2001)
B. Lohmann, S. Fritzsche, J. Phys. B **29**, 5711–5723 (1996)
K.A. Long, H.G. Paretzke, J. Chem. Phys. **95**, 1049 (1991)
M.A. López-Valverde, D.P. Edwards, M. López-Puertas, C. Roldan, J. Geophys. Res. **103**, 16,799–16,811 (1998)
D.A. Lorentzen, Ann. Geophys. **18**, 81–89 (2000)
G. Lu, M. Brittnacher, G. Parks, D. Lummerzheim, J. Geophys. Res. **105**, 18,483 (2000)
G. Lu, D.N. Baker, R.L. McPherron, C.J. Farrugia, D. Lummerzheim, J.M. Ruohoniemi et al., J. Geophys. Res. **103**, 11,685 (1998)
J.G. Luhmann, R.E. Johnson, M.H.G. Zhang, Geophys. Res. Lett. **19**, 2151–2154 (1992)
D. Lummerzheim, M.H. Rees, H.R. Anderson, Planet. Space Sci. **37**, 109–129 (1989)
D. Lummerzheim, M. Brittnacher, D. Evans, G.A. Germany, G.K. Parks, M.H. Rees, J.F. Spann, Geophys. Res. Lett. **24**, 987 (1997)
D. Lummerzheim, M. Galand, J. Semeter, M.J. Mendillo, M.H. Rees, F.J. Rich, J. Geophys. Res. **106**, 141–148 (2001)
M. Lundqvist, P. Baltzer, D. Edvardsson, L. Karlsson, B. Wannberg, Phys. Rev. Lett. **75**, 1058–1061 (1995)
M. Lundqvist, D. Edvardsson, P. Baltzer, B. Wannberg, J. Phys. B **29**, 1489–1499 (1996)
Y.-J. Ma, A.F. Nagy, Geophys. Res. Lett. **34** (2007). doi:10.1029/2006GL029208
Y.-J. Ma, K. Altwegg, T. Breus, M.R. Combi, T.E. Cravens, E. Kallio, S.A. Ledvina, J.G. Luhmann, S. Miller, A.F. Nagy, A.J. Ridley, D.F. Strobel, Space Sci. Rev. (2008, this issue)
T.D. Märk, J. Chem. Phys. **63**, 3731–3736 (1975)

A. Marten, T. Hidayat, Y. Biraud, R. Moreno, Icarus **158**, 532–544 (2002)
P.A. Martin, F.R. Bennett, J.P. Maier, J. Chem. Phys. **100**, 4766–4774 (1994)
D. Mathur, Phys. Rep. **225**, 193–272 (1993)
D. Mathur, Phys. Rep. **391**, 1–118 (2004)
D. Mathur, L.H. Andersen, P. Hvelplund, D. Kella, C.P. Safvan, J. Phys. B **28**, 3415–3426 (1995)
T. Matsui, A.S.-C. Cheung, W.W.-S. Leung, K. Yoshino, W.H. Parkinson, A.P. Thorne, J.E. Murray, K. Ito, T. Imajo, J. Mol. Spectrosc. **219**, 45–57 (2003)
A. Maurellis, T.E. Cravens, G. Randall Gladstone, J.H. Waite, L.W. Acton, Geophys. Res. Lett. **27**, 1339–1342 (2000)
K.E. McCulloh, J. Chem. Phys. **48**, 2090–2093 (1968)
M.A. McGrath et al., in *Jupiter: Planet, Atmosphere, Magnetosphere*, ed. by F. Bagenal et al. (2004), Chap. 19
M.A. McGrath, R.E. Johnson, Icarus **69**, 519 (1987)
R. Meier, G. Crowley, D.J. Strickland, A.B. Christensen, L.J. Paxton, D. Morrison, C.L. Hackert, J. Geophys. Res. **110**, A09S41 (2005). doi:10.1029/2004JA010990
M. Mendillo, P. Withers, in *Radio Sounding and Plasma Physics*, ed. by P. Song, J. Foster, M. Mendillo, D. Bilitza (Am. Inst. Physics, 2008), #978–0–7354–0493–9
M. Mendillo, P. Withers, D. Hinson, H. Rishbeth, B. Reinisch, Science **311**, 1135–1138 (2006)
M. Mendillo, S. Laurent, J. Wilson, J. Baumgardner, J. Konrad, W.C. Karl, Nature **448**, 330–332 (2007)
C.-I. Meng, K. Liou, P.T. Newell, Phys. Chem. Earth (C) **26**, 43–47 (2001)
J.E. Mentall, E.P. Gentieu, J. Chem. Phys. **52**, 5641–5645 (1970)
M. Michael, R.E. Johnson, Planet. Space Sci. **53**, 1510–1514 (2005)
M. Michael, R.E. Johnson, F. Leblanc, M. Liu, J.G. Luhmann, V.I. Shematovich, Icarus **175**, 263–267 (2005)
H.H. Michels, in *The Excited State in Chemical Physics* (Wiley, New York, 1981) pp. 241–265
D.L. Mitchell, R.P. Lin, H. Rème, D.H. Crider, P.A. Cloutier, J.E.P. Connerney, M.H. Acuña, N.F. Ness, Geophys. Res. Lett. **27**, 1871–1874 (2000)
W.E. Moddeman, T.A. Carlson, M.O. Krause, B.P. Pullen, W.E. Bull, G.K. Schweitzer, J. Chem. Phys. **55**, 2317–2336 (1971)
P.F. Morrissey, P.D. Feldman, J.T. Clarke, B.C. Wolven, D.F. Strobel, S.T. Durrance, J.T. Trauger, Astrophys. J. **476**, 918 (1997)
J.I. Moses, Icarus **143**, 244–298 (2000)
J.I. Moses, M. Allen, Y.L. Yung, Icarus **99**, 318–346 (1992)
L. Mrázek, J. Žabka, Z. Dolejšek, J. Hrušák, Z. Herman, J. Phys. Chem. A **104**, 7294–7303 (2000)
A. Mühleisen, M. Budnar, J.-Cl. Dousse, Phys. Rev. A **54**, 3852–3858 (1996)
Müller-Wodarg et al., Space Sci. Rev. (2008, this issue)
A.S. Mullin, D.M. Szaflarski, K. Yokoyama, G. Gerber, W.C. Lineberger, J. Chem. Phys. **96**, 3636–3648 (1992)
A.F. Nagy, P.M. Banks, J. Geophys. Res. **75**(31), 6260–6270 (1970)
F.L. Nesbitt, G. Marston, L.J. Stief, J. Phys. Chem. **95**, 7613–7617 (1991)
A. Noelle, G.K. Hartman, D. Lary, S. Le Calve, S. Trick, A.D. Vandaele, R.P. Wayne, C.Y.R. Wu, *UV/Vis Spectra Data Base, Science-softCon*, 5th edn (2007)
B. Noller, I. Fischer, J. Chem. Phys. **126**, 144302 (2007)
K. Onda, M. Ejiri, Y. Itikawa, J. Geophys. Res. **104**, 27,991–28,001 (1999)
N. Østgaard, J. Stadsnes, J. Bjordal, R.R. Vondrak, S.A. Cummer, D.L. Chenette, M. Schulz, J. Pronko, J. Geophys. Res. **105**, 20,869 (2000)
N. Østgaard, J. Stadsnes, J. Bjordal, G.A. Germany, R.R. Vondrak, G.K. Parks, S.A. Cummer, D.L. Chenette, J.G. Pronko, J. Geophys. Res. **106**(A11), 26,081–26,089 (2001)
D. Pallamraju, S. Chakrabarti, J. Atmos. Sol.-Terr. Phys. **68**, 1459–1471 (2006). doi:10.1016/j.jastp.2005.05.013
L. Pallier, R. Prangé, Geophys. Res. Lett. **31**(6), L06701 (2004). doi:10.1029/2003GL018041
H.G. Paretzke, Adv. Space Res. **9**, 15–20 (1989)
F. Penent, P. Lablanquie, R.I. Hall, J. Palaudoux, K. Ito, Y. Hikosaka, T. Aoto, J.H.D. Eland, J. Electron. Spectrosc. Rel. Phenom. **7–11**, 144–147 (2005)
J.J. Perry, Y.H. Kim, J.L. Fox, H.S. Porter, J. Geophys. Res. **104**, 16,541–16,565 (1999)
D. Petrini, F.X. de Araújo, Astron. Astrophys. **282**, 315–317 (1994)
M. Pospieszalska, R.E. Johnson, J. Geophys. Res. **101**, 7565–7573 (1996)
R. Prangé, D. Régo, L. Pallier, L. Ben Jaffel, C. Emerich, J. Ajello, J.T. Clarke, G.E. Ballester, Astrophys. J. **484**, L169–L173 (1997)
R. Prangé, L. Pallier, K.C. Hansen, R. Howard, A. Vourlidas, R. Courtin, C. Parkinson, Nature **432**, 78–81 (2004). doi:10.1038/nature02986

R.G. Prinn, in *The Photochemistry of Atmospheres: Earth, the Other Planets, and Comets*, ed. by J.S. Levine (Academic Press, Orlando, 1985)
M.H. Rees, Planet. Space Sci. **11**, 1209–1218 (1963). doi:10.1016/0032-0633(63)90252-6
M.H. Rees, *Physics and Chemistry of the Upper Atmosphere* (Cambridge University Press, New York, 1989)
M.H. Rees, B.A. Emery, R.G. Roble, K. Stamnes, J. Geophys. Res. **88**, 6289–6300 (1983)
M.H. Rees, D. Lummerzheim, R.G. Roble, Space Sci. Rev. **71**, 691 (1995)
D. Régo, R. Prangé, L. Ben Jaffel, J. Geophys. Res. **104**, 5939–5954 (1999)
D. Régo, J.T. Clarke, L. Ben Jaffel, G.E. Ballester, R. Prangé, J. McConnell, Icarus **150**, 234–243 (2001). doi:10.1006/icar.2000.6583
H. Rishbeth, O.K. Garriott, *Introduction to Atmospheric Physics* (Academic Press, New York, 1969)
R.G. Roble, E.C. Ridley, R.E. Dickinson, J. Geophys. Res. **92**, 8745–8758 (1987)
C. Roldán, M.A. Lopez-Valverde, M. Lopez-Puertas, D.P. Edwards, Icarus **147**, 11–25 (2000)
H.R. Sadeghpour, A. Dalgarno, Phys. Rev. A. **47**, R2458–R2459 (1993)
C. Sætre, C.A. Barth, J. Stadsnes, N. Østgaard, S.M. Bailey, D.N. Baker, G.A. Germany, J.W. Gjerloev, J. Geophys. Res. **112**, A08306 (2007). doi:10.1029/2006JA012203
C.P. Safvan, M.J. Jensen, H.B. Pedersen, L.H. Andersen, Phys. Rev. A **60**, R3361–R3364 (1999). Erratum in Phys. Rev. A, **60**, R3361 (1999)
J.A.R. Samson, G.N. Haddad, J. Opt. Soc. Am. B **11**, 277–279 (1994)
R.P. Saxon, T.G. Slanger, J. Geophys. Res. **91**, 9877 (1986)
R.W. Schunk, A.F. Nagy, *Ionospheres: Physics, Plasma Physics, and Chemistry* (Cambridge University Press, New York, 2000)
K. Seiersen, A. Al-Khalili, O. Heber, M.J. Jensen, I.B. Pedersen, C.P. Safvan, L.H. Andersen, Phys. Rev. A **68**, 022708 (2003a)
K. Seiersen, O. Heber, M.J. Jensen, C.P. Safvan, L.H. Andersen, J. Chem. Phys. **119**, 839–843 (2003b)
V.I. Shematovich, D.V. Bisikalo, J.-C. Gérard, J. Geophys. Res. **99**, 23,217 (1994)
V.I. Shematovich, R.E. Johnson, M. Michael, J.G. Luhmann, J. Geophys. Res. **108**, 5087 (2003). doi:10.1029/2003JE002094
E. Shigemasa, T. Gejo, M. Nagasono, T. Hatsui, N. Kosugi, Phys. Rev. A **66**, 022508 (2002)
C. Simon, J. Lilensten, O. Dutuit, R. Thissen, O. Witasse, C. Alcaraz, H. Soldi-Lose, Ann. Geophys. **23**, 781–797 (2005)
D.E. Siskind, D.J. Strickland, R.R. Meier, T. Majeed, F.G. Eparvier, J. Geophys. Res. **100**, 19,687–19,694 (1989)
T.G. Slanger et al., Space Sci. Rev. (2008, this issue)
F.L. Smith, C. Smith, J. Geophys. Res. **77**, 3592–3597 (1972)
P.F. Smith, K. Yoshino, W.H. Parkinson, K. Ito, G. Stark, J. Geophys. Res. **96**, 17,529–17,533 (1991)
S.C. Solomon, Geophys. Res. Lett. **20**, 185–188 (1993)
J.P. Sprengers, W. Ubachs, K.G.H. Baldwin, J. Chem. Phys. **122**, 144301 (2005)
S.C. Solomon, S.M. Bailey, T.N. Woods, Geophys. Res. Lett. **28**, 2149–2152 (2001)
V. Srivastava, V. Singh, J. Geophys. Res. **93**, 5845–5854 (1988)
G. Stark, K. Yoshino, P.L. Smith, J.R. Esmond, K. Ito, M.H. Stevens, Astrophys. J. **410**, 837–842 (1993)
G. Stark, K.P. Huber, K. Yoshino, P.L. Smith, K. Ito, J. Chem. Phys. **123**, 214303 (2005)
G. Stark, K. Yoshino, P.L. Smith, K. Ito, J. Quant. Spectrosc. Rad. Transf. **103**, 67–73 (2007)
M.H. Stevens, D.F. Strobel, M.E. Summers, R.V. Yelle, Geophys. Res. Lett. **19**, 669–672 (1992)
J.A.D. Stockdale, J. Chem. Phys. **66**, 1792–1794 (1977)
D.J. Strickland, D.L. Book, T.P. Coffey, J.A. Fedder, J. Geophys. Res. **81**, 2755–2764 (1976)
D.J. Strickland, R.R. Meier, J.H. Hecht, A.B. Christensen, J. Geophys. Res. **94**(A10), 13,527–13,539 (1989)
D.J. Strickland, R.J. Cox, R.R. Meier, D.P. Drob, J. Geophys. Res. **104**, 4251 (1999)
D.J. Strickland, J. Bishop, J.S. Evans, T. Majeed, R.J. Cox, D. Morrison, G.J. Romick, J.F. Carbary, L.J. Paxton, C.-I. Meng, J. Geophys. Res. **106**, 65 (2001)
D.F. Strobel, in *Atmospheres in the Solar System: Comparative Aeronomy*, ed. by M. Mendillo, A. Nagy, H. Waite, AGU Monograph, vol. 130 (AGU Press, 2002), pp. 7–22
G. Sundström, M. Carlson, M. Larsson, Broström, Chem. Phys. Lett. **218**, 17–20 (1994)
S. Svensson, J. Phys. B **38**, S821–S835 (2005)
S. Svensson, A. Naves de Brito, M.P. Keane, N. Correia, L. Karllson, C.-M. Liegenner, A. Ågren, J. Phys. B **25**, 135–144 (1992)
P.R. Taylor, H. Partridge, J. Phys. Chem. **91**, 6148–6151 (1987)
H.A. Taylor, H.C. Brinton, S.J. Bauer, R.E. Hartle, P.A. Cloutier, R.E. Daniell, J. Geophys. Res. **85**, 7765–7777 (1980)
H.A. Taylor, Th. Encrenaz, D.M. Hunten, P.G.J. Irwin, T. Cowan, in *Jupiter: The Planet, Satellites, and Magnetospheres*, ed. by F. Bagenal, T.E. Dowling, W.B. McKinnon (2004)
W.K. Tobiska, J. Atmos. Terr. Phys. **53**, 1005–1018 (1991)

W.K. Tobiska, Adv. Space. Res. **34**(8), 1736–1746 (2004)
W.K. Tobiska, S.D. Bouwer, Adv. Space Res. **37**(2), 347–358 (2006). doi:10.1016/j.asr.2005.08.015
M.G. Tomasko et al., Nature **438**, 765–778 (2005)
M.R. Torr, D.G. Torr, R.A. Ong, H.E. Hinteregger, Geophys. Res. Lett. **6**, 771–774 (1979)
M. Uda, H. Endo, K. Maeda, Y. Awaya, M. Kobayashi, Y. Sasa, H. Kumagi, T. Tomma, Phys. Rev. Lett. **42**, 1257–1269 (1979)
E.F. van Dishoeck, J.H. Black, Astrophys. J. **334**, 771–802 (1988)
D.A. Verner, D.G. Yakovlev, Astron. Astrophys. Suppl. Ser. **109**, 125–133 (1995)
D.A. Verner, G.J. Ferland, K.T. Korista, D.G. Yakovlev, Astrophys. J. **465**, 487–498 (1996)
G.A. Victor, E.R. Constantinides, Geophys. Res. Lett. **6**, 519–522 (1979)
J.H. Waite, T.E. Cravens, Adv. Space Res. **7**(12), 119–134 (1987)
J.H. Waite, D. Lummerzheim, in *Atmospheres in the Solar System: Comparative Aeronomy*, ed. by M. Mendillo, A. Nagy, H. Waite, AGU Monograph, vol. 130 (AGU Press, 2002), pp. 115–139
J.H. Waite, G.R. Gladstone, W.S. Lewis, P. Drossart, T.E. Cravens, A.N. Maurellis, B.H. Mauk, S. Miller, Science **276**, 104–108 (1997)
C.W. Walter, P.C. Cosby, H. Helm, J. Chem. Phys. **99**, 3553–3561 (1993)
R.A. West, K.H. Baines, A.J. Friedson, D. Banfield, B. Ragent, F.W. Taylor, in *Jupiter: The Planet, Satellites, and Magnetosphere*, ed. by F. Bagenal, T.E. Dowling, W. McKinnon (Cambridge University Press, Cambridge, 2004)
R.W. Wetmore, R.K. Boyd, J. Phys. Chem. **90**, 5540–5551 (1986)
J.K. Wilson, M. Mendillo, J. Baumgardner, N.M. Schneider, J.T. Trauger, B. Flynn, Icarus **157**, 476–489 (2002)
J.D. Winningham, D.T. Decker, J.U. Kozyra, J. Geophys. Res. **94**, 15,335–15,348 (1989)
O. Witasse et al., Space Sci. Rev. (2008, this issue)
O. Witasse, O. Dutuit, J. Lilensten, R. Thissen, J. Zabka, C. Alcaraz, P.-L. Blelly, S.W. Bougher, S. Engel, L.H. Andersen, K. Seiersen, Geophys. Res. Lett. **29**, 1263 (2002). doi:10.1029/2002GL014781
T.N. Woods, F.G. Eparvier, S.M. Bailey, P.C. Charberlin, J. Lean, G.J. Rottman, S.C. Solomon, W.K. Tobiska, D.L. Woodraska, J. Geophys. Res. **110**, A01312 (2005). doi:10.1029/2004JA010765
J.S. Wright, D.J. Carpenter, A.B. Alekseyev, H.-P. Lieberman, R. Lingott, R.J. Buenker, Chem. Phys. Lett. **266**, 391–396 (1997)
C.Y.R. Wu, F.Z. Chen, D.L. Judge, J. Geophys. Res. **109**, E07S15 (2004). doi:10.1029/2003JE002180
M. Yan, H.R. Sadeghpour, A. Dalgarno, Astrophys. J. **496**, 1044–1050 (1998)
Yelle, Miller, in *Jupiter, the Planet, Satellites, and Magnetosphere*, ed. by F. Bagenal et al. (Cambridge University Press, Cambridge, 2002)
R.V. Yelle, J.I. Lunine, J.B. Pollack, R.W. Brown, in *Neptune and Triton*, ed. by D.P. Cruikshank (University of Arizona Press, Tucson, 1995), pp. 1031–1106
R.V. Yelle, N. Borggren, V. de la Haye, W.T. Kasprzak, H.B. Niemann, I. Müller-Wodard, J.H. Waite, Icarus **182**, 567–576 (2006)
K. Yoshino, D.E. Freedman, W.H. Parkinson, J. Phys. Chem. Ref. Data **13**, 207–227 (1984)
K. Yoshino, A.S.-C. Cheung, J.R. Esmond, W.H. Parkinson, D.E. Freedman, S.L. Guberman, A. Jenvrier, B. Coquart, M.F. Merienne, Planet. Space Sci. **36**, 1469–1475 (1988)
K. Yoshino, J.R. Esmond, A.S.-C. Cheung, D.E. Freedman, W.H. Parkinson, Planet. Space Sci. **40**, 185–192 (1992)
K. Yoshino, G. Stark, J.R. Esmond, P.L. Smith, K. Ito, T. Matsui, Astrophys. J. **438**, 1013–1016 (1995)
K. Yoshino, J.R. Esmond, Y. Sun, W.H. Parkinson, K. Ito, T. Matsui, J. Quant. Spectrosc. Rad. Trans. **55**, 53–60 (1996)
K. Yoshino, W.H. Parkinson, K. Ito, T. Matsui, J. Mol. Spectrosc. **229**, 238–243 (2005)
R.W. Zurek, J.R. Barnes, R.M. Haberle, J.B. Pollack, J.E. Tillman, C.B. Leovy, in *Mars*, ed. by H.H. Kieffer, B.M. Jakosky, C.W. Snyder, M.S. Matthews (University of Arizona Press, Tucson, 1992), pp. 835–933